UNIVERSITY OF SOUTHAMPTON

An Adaptive Mid-Infrared Ultrashort Pulse Source for Applications in Coherent Control

by

Hazel Hung

A thesis submitted in partial fulfillment for the degree of Doctor of Philosophy

in the

Faculty of Engineering, Science and Mathematics

Optoelectronics Research Centre

October 2008

UNIVERSITY OF SOUTHAMPTON

Abstract

Faculty of Engineering, Science and Mathematics
Optoelectronics Research Centre

Doctor of Philosophy

An Adaptive Mid-infrared Ultrashort Pulse Source for Applications in Coherent Control

by Hazel Hung

An adaptive mid-infrared (MIR) ultrashort pulse source is investigated for application to the coherent control of molecules. The MIR regime will allow access to vibrational modes of common organic bonds, and ultrashort pulse durations should enable the required interaction to occur before the energy is redistributed throughout the molecule. By using the molecular system as part of an adaptive learning loop, one can deliver the desired MIR pulse without the need for prior lengthy calculations to solve the Hamiltonian.

The adaptive MIR pulse shaper is presented as a feasibility study in this thesis. It involves shaping a near-infrared (NIR) pulse using a spatial light modulator in a phase-only pulse shaper. The shaped NIR pulse is then transferred to the MIR via a synchronously pumped optical parametric oscillator (SPOPO), which is consequently measured using a nonlinear detector whose signal is used as the feedback parameter to be optimised. Using a global optimisation algorithm, initial experiments demonstrated adaptive MIR pulse shaping, achieving pulse compression and double pulse generation.

The transfer of the pulse shape from the NIR to the MIR in the SPOPO however, is non-trivial and is discussed in detail, both numerically and experimentally, in this thesis. The results show that parameters such as the signal pulse bandwidth, temporal walk-off of the interacting pulses, signal gain, pump depletion, and group velocity dispersion should be considered when high fidelity transfer is required. It is also shown that, for an SPOPO based on periodically poled $LiNbO_3$ high-fidelity transfer is possible for wavelengths centred around $3.5\,\mu$m with a tunability of $\pm 0.5\,\mu$m.

The investigation then progresses to the femtosecond regime where the demonstration of coherent control experiments becomes more accessible. Using a fibre-based chirped pulse amplification system, which is an attractive pump source for the SPOPO, adaptive pulse shaping is demonstrated, showing significant improvement in the quality of the 500 fs source at high pulse energies of $65\,\mu$J, as a result of the learning loop.

Thus the individual components to make the adaptive MIR ultrashort pulse shaping system have all been demonstrated; namely the adaptive shaping of MIR pulses via an SPOPO, the high-fidelity transfer of NIR pump pulses to the MIR in an SPOPO, and the femtosecond NIR pump source.

Contents

Declaration of Authorship

I, Hazel Hung, declare that this thesis titled, "An Adaptive Mid-infrared Light Source for Applications in Coherent Control," and the work presented in it are my own. I confirm that:

- This work was done wholly or mainly while in candidature for a research degree at this University
- Where any part of this thesis has previously been submitted for a degree or any other qualification at this University or any other institution, this has been clearly stated
- Where I have consulted the published work of others, this is always clearly attributed
- Where I have quoted from the work of others, the source is always given. With the exception of such quotations, this thesis is entirely my own work
- I have acknowledged all main sources of help
- Where the thesis is based on work done by myself jointly with others, I have made clear exactly what was done by others and what I have contributed myself
- Parts of this work have been published as:
  - N. A. Naz et al. , Opt. Express 13, pp. 8400-8405, 2005.
  - J. Prawiharjo et al. , J. Opt. Soc. Am. B 24, pp. 895-905, 2007.
  - J. Prawiharjo et al. , J. Opt. Soc. Am. B 24, pp. 2484-2493, 2007.
  - H. S. S. Hung et al. , J. Opt. Soc. Am. B 24, pp. 2998-3006, 2007.
  - F. He et al. , Opt. Express 16, pp. 5813-5821, 2008.

Signed:

Date: 5th October 2008

Acknowledgements

I would like to thank my supervisor, Prof. Dave Shepherd, for his constant patience, encouragement and guidance throughout my studies. Dave never failed to pick up my spirits during my PhD blues, a time when months of tinkering away in the lab felt like they came to nothing, by somehow showing me the brighter side of things.

Thanks also go to Dr Martin O'Connor and Naveed Naz for showing me the ropes in the lab and introducing me to the dazzling beauty that is the OPO. I am grateful for their patience and all the times they put up with my constant nagging of questions. For his inhuman wealth of knowledge of optics and Matlab, I would like to thank Dr Jerry Prawiharjo, without whom I would still be stuck in the lab today, working on the sonogram. He has helped me to understand so much about optics.

For helping me out in the lab, I would also like to thank Nikita Daga, who also listened so intently at my attempts to explain how the lab works. I gained a lot from that experience and I hope that it benefited her at least half as much as it did me. I am also grateful to Prof. Dave Hanna whose words of wisdom have helped, on numerous occasions, with progress in the lab as well as discussions on the intricacies of the OPO. I would also like to thank my colleagues, Fei He and Jonathan Price, for their hard work and patience during our collaborative work on the fibre CPA system. I must also thank the technicians, Simon Butler and Tim McIntyre, for making and tweaking many mounts in the workshop for me and for always being so incredibly efficient. Thanks also go to Corin Gawith from Stratophase for fabricating the PPLN crystal used in the XFROG setup.

Away from the lab and office, I would like to thank my friends for keeping me sane and helping me maintain a good balance of work and play. I must also extend my deepest gratitude to my parents and sister for their incredible support in everything that I do.

Finally, I am ever indebted to James for looking out for me, believing in me and for always being there.

Abbreviations

AC	Autocorrelation
AOCC	Adaptive optimal coherent control
AOM	Acousto-optic modulator
AOPDF	Acousto-optic programmable dispersive filter
ASA	Adaptive simulated annealing
CARS	Coherent anti-Stokes raman scattering
CCS	Cross-correlation sonogram
CDMA	Code-division multiple access
CPA	Chirped pulse amplification
CSA	Classical simulated annealing
DE	Differential evolution
DFG	Difference-frequency generation
DRO	Doubly resonant oscillator
EA	Evolutionary algorithm
ES	Evolutionary strategy
FFT	Fast Fourier transform
FOD	Fourth order dispersion
FP	Fourier plane
FRAC	Fringe-resolved autocorrelation
FROG	Frequency resolved optical gating
FSA	Fast simulated annealing
FT	Fourier transform
FWHM	Full-width half-maximum
GA	Genetic algorithm
GDD	Group delay dispersion

GP	Generalized-projections
GSA	Generalized simulated annealing
GVD	Group velocity dispersion
GVM	Group velocity mismatch
HR	Highly reflecting
IVBC	Initial value boundary conditions
IVR	Intramolecular vibrational-enery redistribution
LCM	Liquid crystal modulator
LED	Light-emitting diode
MIR	Mid-infrared
NIR	Near-infrared
OBPF	Optical band-pass filter
OC	Output coupler
OPA	Optical parametric amplifier
OPO	Optical parametric oscillator
OSA	Optical spectrum analyser
PCF	Photonic crystal fibre
PCGP	Principle component generalized projections
PG FROG	Polarisation-gate frequency resolved optical gating
PM	Polarisation maintaining
PPLN	Periodically poled lithium niobate
QPM	Quasi-phase-matching
RMS	Root mean square
SA	Simulated annealing
SD FROG	Self-diffracting frequency resolved optical gating
SFG	Sum-frequency generation
SHG	Second-harmonic generation
SLM	Spatial light modulator
SPIDER	Spectral phase interferometry for direct electric-field reconstruction
SPM	Self-phase modulation
SPOPO	Synchronously pumped optical parametric oscillator
SQ	Simulated quenching
SRO	Singly resonant oscillator

SVD	Singular value decomposition
TOD	Third order dispersion
TPA	Two-photon absorption
UV	Ultra-violet
VSFS	Vibrational sum frequency spectroscopy
XFROG	Cross-correlation frequency resolved optical gating

Symbols

θ_d	Grating diffracted angle (rad)
θ_{in}	Grating incident angle (rad)
m	Grating order
d	Grating period (m)
λ	Centre wavelength (m)
D	Angular dispersion (rad/m)
$\Delta\lambda$	Pulse bandwidth (m)
$\Delta\theta_d$	Dispersion angle (rad)
a	Spatial extend of beam at FP (m)
f_L	Focal length (m)
α	Spatial dispersion (m/(rad/s))
$\Delta\omega$	Bandwidth (rad/s)
c	Speed of light (m/s)
t	Time (s)
f	Frequency (Hz)
ω	Radial frequency (rad/s)
$E_{in}(t)$	Input pulse electric field
$E_{out}(t)$	Output pulse electric field
$H(t)$	Impulse response function
$\widetilde{E}_{in}(\omega)$	FT of $E_{in}(t)$
$\widetilde{E}_{out}(\omega)$	FT of $E_{out}(t)$
$\widetilde{H}(\omega)$	FT of $H(t)$
$\widetilde{M}(x), \widetilde{M}(\alpha\omega)$	Masking function
$\widetilde{E}_m(x,\omega)$	Electric field immediately after mask
w_0	Spot size of each individual frequency (m)

w_i	Spot size of collimated input beam (m)
$\Delta x/\Delta t$	Time-dependent spatial shift on shaper output pulse (m/s)
$\delta\omega$	Pulse shaper resolution (rad/s)
η	Pulse shaper complexity
$M(t)$	Inverse FT of $\widetilde{M}(\alpha\omega)$
$G(t)$	Gaussian envelope of time window
T	Pulse shaper time window (s)
B	Bandwidth (Hz)
δt	Temporal resolution (s)
δf	Spectral resolution (Hz)
N_{pix}	Number of pixels
phi	Phase (rad)
$\Delta\omega_{pix}$	Frequency span of one pixel (rad/s)
Ω	Frequency detuning (rad/s)
β_n	nth order dispersion parameter ($\mathrm{rad}^n/\mathrm{s}^{n-1}$)
$\beta_{n_{max}}$	maximum nth order dispersion parameter ($\mathrm{rad}^n/\mathrm{s}^{n-1}$)
$\mathbf{P}$	Polarisation vector
$\mathbf{E}$	Electric field vector
ϵ_0	Electric permittivity of free space
$\chi^{(n)}$	nth order susceptibility
$\mathbf{r}$	Resultant vector of vectors $\mathbf{x}$, $\mathbf{y}$, and $\mathbf{z}$
ω_p, ω_3	Pump photon frequency (rad/s)
ω_s, ω_2	Signal photon frequency (rad/s)
ω_i, ω_1	Idler photon frequency (rad/s)
$\hbar$	Planck's constant (Js)
k_p, k_3	Pump wavevector (m^{-1})
k_s, k_2	Signal wavevector (m^{-1})
k_i, k_1	Idler wavevector (m^{-1})
Δk	Wavevector mismatch (m^{-1})
L_c	Coherence length (m)
n_j	Refractive index
Λ	Poling Period (m)
k_G	Grating wavevector (m^{-1})

A_j	Slowly varying electric field envelope
z	Axis along which the pulse propagates (m)
α_j	Nonlinear parameter
d_{eff}	Effective nonlinear index
$n(\omega_j)$	Effective refractive index
g	Gain parameter
Γ	Parametric gain coefficient
I_3	Pump intensity (W)
$G_2(L)$	Single-pass incremental signal gain
$\Delta\Omega_2$	Signal gain bandwidth
ν_j	Group velocity (m/s)
$\delta\nu_{jk}$	Group velocity mismatch (s/m)
$P_{p,th}$	Theshold peak pump power (W)
ϵ_s	Fractional power loss per round trip
g_t	Parameter for pump-signal temporal overlap
l_{eff}	Effective interaction length (m)
h_2	Guha's integral
ξ_s	Confocal parameter
b_s	Confocal length (m)
$G_{mult}(L)$	Single-pass multiplicative signal gain
R_M	Output coupler reflectivity
R_L	Effective reflectivity for intracavity losses
Γ_{th}	Gain theshold
P_{th}	Theshold average power (W)
K	Proportionality Constant in Findlay-Clay analysis (W^{-1})
$\widetilde{P}_j^{NL}(z,\omega_j)$	Nonlinear polarisation
Δk_{DFG}	Wavevector mismatch for DFG (m^{-1})
b_j	Group velocity dispersion (s^2/m^2)
δb_{jk}	Group velocity dispersion mismatch (s^2/m^2)
$P(x_t \rightarrow x_{j+1})$	Acceptance probability
$E(x_j)$	Energy of the system at position x_j
$T(j)$	Temperature of the system
T_0	Initial temperature

T_a	Acceptance temperature
T_v	Visiting temperature
q_a	acceptance parameter
q_v	visiting parameter
$I_{AC}(\tau)$	Intensity autocorrelation
τ	Variable autocorrelator delay
$I_{FRAC}(\tau)$	Fringe resolved autocorrelation intensity
τ_j	FWHM pulse width at frequency ω_j
R_{NL}	Nonlinear response (nA/(mW)^2)
I_{TPA}	Two-photon absorption photocurrent (nA)
P_pk	Peak power (mW)
P_av	Average power (mW)
S	Sensitivity (mW^2)
$\Sigma_g^E(\omega,\tau)$	Spectrogram intensity
$E_{sig}(t,\tau)$	Measured signal field
$g(t-\tau)$	Gate pulse electric field
$I_{FROG}(\omega,\tau)$	Frequency resolved optical gating intensity
$G^{(k)}$	RMS error
$I_{sono}(t,\Omega)$	Sonogram intensity
$I_{xsono}(t,\Omega)$	Cross-correlation sonogram intensity
τ_{ps}	Delay between the pump and signal entering the nonlinear crystal
$\psi(z,\Omega_j)$	Spectral amplitude profile
$\phi(z,\Omega_j)$	Spectral phase profile
$f(t)$	Normalised Gaussian temporal profile of numerical input pulse
δt_p	Temporal FWHM of numerical input pulse
Z	Transfer fidelity based on the spectrogram
$S_j(\Omega,\tau;z)$	Polarisation gate spectrogram
Δk_0	Wavevector mismatch between the centre wavelengths
$D(L,\Omega_i)$	Filter function
$\widetilde{A}_e(\Omega_s)$	Effective signal field
τ_c	Critical pump-signal delay for symmetric walk-through
$\mathcal{M}\left[A_s(L,t)\right]$	Modified signal field
R	Total signal reflectivity of cavity mirrors

$G_F(\Omega_s)$	Optical band-pass filter function
δf_F	FHWM of optical band-pass filter (Hz)
Z_S	Spectral transfer fidelity
τ'	Round-trip mismatch for experimental SPOPO (s)
τ'_m	Round-trip mismatch for minimum (s)
$\phi_{SLM}(\Omega)$	Phase applied by SLM (rad)

“ It was octarine, the colour of magic. It was alive and glowing and vibrant and it was the undisputed pigment of the imagination, because wherever it appeared it was a sign that mere matter was a servant of the powers of the magical mind. It was enchantment itself. But Rincewind always thought it looked a sort of greenish-purple.”

“The Colour of Magic”, Terry Pratchett

Chapter 1

Introduction

1.1 Thesis motivation

Tailoring ultrashort pulses in the mid-infrared wavelength regime is a powerful technique for applications in spectroscopy [1–5] and particularly coherent control [6–12], where having adaptive control over the pulse shape can significantly enhance the outcome of chemical reactions. Control of chemical reactions with lasers has been well practised since the 1960s. Initial experiments [13] investigated control through mode-selective chemistry which involved tuning the laser frequency to a specific vibrational mode of the required bond. However, control could only be achieved with specific molecules that met certain conditions. This was due to a process known as intramolecular vibrational-energy redistribution (IVR) where anharmonic coupling between modes causes the laser excitation energy to be very rapidly transferred to other vibrational modes of the molecule. Experiments were successful in which the IVR time of the rapid transfer exceeded the reaction time [14]. Due to the very short timescale of IVR, Zewail [13] proposed that ultrashort (sub picosecond) laser pulses were required. Further investigation [15] into the dynamics of IVR highlighted the importance of coherence in mode selectivity.

One of the first methods of active manipulation of molecules using coherent light was developed by Brumer and Shapiro [16]. It involves the excitation of a mode through two or more pathways at the same instant resulting in a quantum mechanical interference

between the reaction pathways. By controlling the relative phases and amplitudes of the light sources, the reaction can be steered to the desired outcome.

Another approach, called the pump-dump scheme, by Tannor and Rice [17, 18] works by controlling the separation of ultrashort pulses. An initial sequence of pump pulses transfer energy from the ground state to an excited molecular state. A sequence of dump pulses, which transfer energy back down to the ground state, is applied after a delay whose length determines the yield of the desired product. The result of the pump pulse sequence is a wave packet of molecular eigenstates of which the amplitude distribution over the possible reaction pathways depends on the pulse shapes as well as the pump-dump delay. However, the complexity of this amplitude distribution means that it is almost impossible to pre-determine the dump pulse shape and delay to result in an efficient product yield.

Rabitz et al. [19, 20] developed a more efficient method which involved the use of optimal control theory to create the ideal pulse sequences for control. Control of the relative phase and amplitude of the pulse frequency components makes it possible to manipulate the shaped wave packet into an evolution that favours a particular reaction pathway. Initial work in designing pulses engaged in solving the molecular Hamiltonian but this became highly complex for systems with more than a few atoms.

Judson and Rabitz then proposed the adaptive optimal coherent control (AOCC) scheme in 1992 [21] in which the experimental arrangement involved a feedback loop to allow the pulse shapes applied to iterate to the ideal, with the use of an evolutionary algorithm. The presence of the sample in the feedback loop edges the laser pulse shape closer and closer to the solution of the Hamiltonian. The adaptive property of this method essentially eliminates the need for a prior detailed knowledge of the molecular system which can be actively manipulated in real-time.

Following advances in ultrafast optics, the first experimental demonstration of AOCC in a molecular system was performed by Bardeen et al. in 1997 [22]. Using femtosecond pulses shaped by an acousto-optic pulse shaper and monitoring fluorescence through a feedback loop configuration, they were able to optimise population transfer to the excited state of dye molecules in solution.

Further advances in AOCC include the control of independent chemical reaction pathways [23], molecular dissociation [24, 25] and molecular manipulation for the enhancement of particular properties [24, 26, 27]. Optimal pulses have also been deciphered to extract information about the dynamics of the system [28, 29]. An experiment for biochemical applications [30] has demonstrated that even highly complex molecular systems can be manipulated through this adaptive technique and that molecular complexity need not be an issue with coherent control. Finally, AOCC has also been applied to biomedical imaging applications, through phase-only shaping for compensation of light scattering in biological tissue [31].

The adaptive pulse shaping technique behind AOCC has extended to other applications besides photochemistry. These include adaptive pulse compression [32], arbitrary waveform generation [33] ultrashort pulse propagation in fibres [34], chirped pulse amplification schemes [35, 36], control of multiphoton processes in a quantum dot saturable Bragg reflector [37], and multimode fibre dispersion compensation [38].

All of the above mentioned demonstrations of AOCC and adaptive pulse shaping were carried out using visible and near-infrared (NIR) radiation, which rely on indirect (e.g. multiphoton excitation) methods of manipulation. More direct control of molecules occurs in the ultraviolet (UV) region, for bond breaking, or in the MIR regime for vibrational modal excitation. Unfortunately, many of the commercially available pulse shaping devices such as liquid crystal modulators (LCMs) [39] and acousto-optic modulators (AOMs) are normally only suitable for the visible and near-infrared (NIR) wavelengths, requiring that alternative methods be used for other regimes such as the UV or mid-infrared (MIR). Such methods include the use of a micromirror array or deformable mirror for phase-only pulse shaping [40, 41] as well as spectral amplitude and phase shaping with a fused silica AOM for the UV [42]. Direct shaping of MIR pulses has been demonstrated with dispersive fibres and/or grating compressors [43–45] but these techniques are not programmable and therefore not suited to adaptive pulse shaping. More recently however, high resolution pulse shaping was achieved using a Ge-doped AOM [46] which was used for adaptive coherent control of a CO-stretching mode [10].

Direct pulse shaping in the MIR has also been demonstrated with a free-electron laser, but by using reflective optics in the pulse shaper that generates only simple, linearly chirped, pulses [44]. Such a MIR source has been used in successful demonstrations of coherent control using a method known as vibrational ladder climbing [6, 7, 43, 47]. This technique was first introduced by Chelkowski et al. in 1990 [48, 49], and involves exciting molecules with appropriately chirped pulses to high vibrational levels causing molecular dissociation. This technique has been extended to optimal control methods, theoretically finding the best chirp for excitation of the CO stretch by solving the Hamiltonian of a polyatomic molecule [8] and recently, the same bond in a biolgical molecule, carboxyhemoglobin [9].

An alternative approach to MIR shaping is to indirectly shape the pulse by initial shaping in the NIR using a LCM or AOM before transferring the pulse to the MIR using an optical parametric process. Such a method was initially demonstrated with difference frequency generation (DFG) from the leading and trailing spectral edges of a chirped femtosecond pulse [50, 51] generating wavelengths beyond 10μm. However other schemes have demonstrated greater wavelength tunability and higher pulse energies from a spectrally narrow pulse and a highly complex pulse generating shaped MIR pulses through DFG [52] and optical parametric amplification (OPA) [1, 53]. However, to the best of my knowledge, other than the work presented in this thesis no adaptive control has been demonstrated in this indirect shaping scheme.

1.2 Adaptive MIR pulse shaper

The work in this thesis aims to demonstrate the feasibility of an adaptive mid-infrared (MIR) pulse shaping system for active manipulation of molecules by AOCC. Many experiments have achieved coherent control in the visible and near-infrared wavelengths for electronic excitation. However, the use of MIR wavelengths will allow for direct excitation of vibrational modes thus improving mode selectivity. The intelligent system will be designed such that it is able to produce shaped pulses in a tunable MIR range. We have chosen an indirect shaping method where generation of the MIR pulses

is achieved with periodically poled lithium niobate (PPLN), a nonlinear material which allows wavelengths up to 7μm [54] when used within a synchronously pumped optical parametric oscillator (SPOPO). The indirect shaping in a SPOPO was demonstrated for the first time in Ref. [55] (see Chapter 4) in contrast to the previous work in DFG processes. The use of a SPOPO provides a more efficient MIR source with low oscillation threshold and one has the practical advantage of requiring only one pump source.

Figure 1.1 shows a schematic diagram of the MIR adaptive pulse shaping system. A NIR pulse is shaped with a one-dimensional, phase only, spatial light modulator (SLM) before being transferred to the MIR region using a SPOPO. Pulse transfer from the pump to the idler ideally requires a monochromatic signal within the optical parametric oscillator (see Section 2.3.4). Although this cannot be achieved experimentally, a flat-phase bandwidth-limited signal will allow high fidelity transfer if the pump bandwidth is much greater than the signal bandwidth. Other factors affecting the fidelity of transfer are also investigated, both numerically and experimentally, in this thesis.

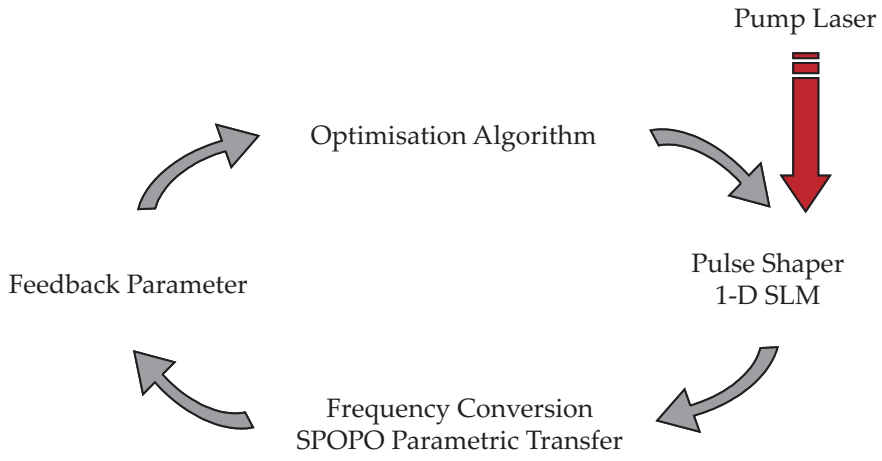

FIGURE 1.1: Flow diagram of the adaptive MIR pulse shaping system.

The shaped idler pulse is then optimised by analysis of a certain parameter, such as a two-photon absorption signal, which can be maximised to cause, for example, idler pulse compression. The fitness of the parameter is then fed back to an optimisation algorithm that has control over the SLM. This process is repeated in an iterative manner until the optimum pulse shape is found. The output pulse is then recorded using an ultrashort pulse measurement, such as, an autocorrelator.

Measurement of MIR pulses, however, is non-trivial compared with visible or NIR wavelengths where devices for spectral phase and amplitude characterisation, such as frequency resolved optical gating (FROG), are readily available. The build and development of MIR pulse characterisation arrangements such as the autocorrelator, sonogram and cross-correlation FROG was carried out as part of the work in this thesis. These diagnostic techniques were then used to provide many of the key results presented herein.

The outline of this thesis is as follows. In Chapter 2, an overview of the MIR pulse shaping system is presented followed by a discussion of the theory behind pulse shaping, optical parametric oscillators and optimisation algorithms. A comprehensive review of pulse characterisation techniques is then given in Chapter 3. Here, an experimental comparison of the cross-correlation sonogram and cross-correlation frequency resolved optical gating technique is also presented for characterisation of MIR SPOPO pulses. In Chapter 4 an experimental demonstration of the feasibility of adaptive MIR pulse shaping, achieving pulse compression and double pulse generation, is presented. The results of this chapter also highlight the consequences of the fidelity of the parametric transfer of the pump pulse characteristics to the MIR. This opens an investigation into parametric transfer in a SPOPO. A numerical study of this process in difference frequency generation is carried out in Chapter 5 before extending the analysis to a SPOPO. Having identified, in the numerical work, the factors affecting parametric transfer, the numerical results are verified by experiment in Chapter 6. The experimental work then progresses from a picosecond pump laser system to a femtosecond fibre chirped pulse amplification (CPA) scheme. In Chapter 7, adaptive shaping in a high-power fibre CPA system is demonstrated. Finally, discussions about future directions, such as, how this work will progress to coherent control experiments, will be presented in the Chapter 8.

References

[1] H. S. Tan and W. S. Warren, "Mid infrared pulse shaping by optical parametric amplification and its application to optical free induction decay measurement," *Opt. Express* **11**, pp. 1021–1028, 2003.

[2] K. A. Tillman, R. R. J. Maier, D. T. Reid, and E. D. McNaghten, "Mid-infrared absorption spectroscopy of methane using a broadband femtosecond optical parametric oscillator based on aperiodically poled lithium niobate," *J. Opt. A. Pure. Appl. Opt.* **7**, pp. S408–S414, 2005.

[3] H. K. Nienhuys, S. Woutersen, R. A. van Santen, and H. J. Bakker, "Mechanism for vibrational relaxation in water investigated by femtosecond infrared spectroscopy," *J. Chem. Phys.* **111**, pp. 1494–1500, 1999.

[4] W. Wohlleben, T. Buckup, J. L. Herek, and M. Motzkus, "Coherent control for spectroscopy and manipulation of biological dynamics," *Chemphyschem* **6**, pp. 850–857, 2005.

[5] E. Tyrode, C. M. Johnson, M. W. Rutland, and P. M. Claesson, "Structure and hydration of poly(ethylene oxide) surfactants at the air/liquid interface. a vibrational sum frequency spectroscopy study," *Journal of Physical Chemistry C* **111**, pp. 11642–11652, 2007.

[6] L. Windhorn, J. S. Yeston, T. Witte, W. Fuss, M. Motzkus, D. Proch, K. L. Kompa, and C. B. Moore, "Getting ahead of IVR: A demonstration of mid-infrared induced molecular dissociation on a sub-statistical time scale," *J. Chem. Phys.* **119**, pp. 641–645, 2003.

[7] D. J. Maas, D. I. Duncan, R. B. Vrijen, W. J. van der Zande, and L. D. Noordam, "Vibrational ladder climbing in NO by (sub)picosecond frequency-chirped infrared laser pulses," *Chem. Phys. Lett.* **290**, pp. 75–80, 1998.

[8] T. Witte, T. Hornung, L. Windhorn, D. Proch, R. de Vivie-Riedle, M. Motzkus, and K. L. Kompa, "Controlling molecular ground-state dissociation by optimizing vibrational ladder climbing," *J. Chem. Phys.* **118**, pp. 2021–2024, 2003.

[9] C. Meier and M. C. Heitz, "Laser control of vibrational excitation in carboxyhemoglobin: A quantum wave packet study," *J. Chem. Phys.* **123**, pp. 161–172, 2005.

[10] D. B. Strasfeld, S.-H. Shim, and M. T. Zanni, "Controlling vibrational excitation with shaped Mid-IR pulses," *Phys. Rev. Lett.* **99**, pp. 038102–4, 2007.

[11] D. Voronine, D. Abramavicius, and S. Mukamel, "Coherent control of pump-probe signals of helical structures by adaptive pulse polarizations," *J. Chem. Phys.* **124**, 2006.

[12] P. Nuernberger, G. Vogt, T. Brixner, and G. Gerber, "Femtosecond quantum control of molecular dynamics in the condensed phase," *Phys. Chem. Chem. Phys.* **9**, pp. 2470–2497, 2007.

[13] A. H. Zewail, "Laser selective chemistry - is it possible," *Phys. Today* **33**, pp. 27–33, 1980.

[14] R. N. Zare, "Laser control of chemical reactions," *Science* **279**, pp. 1875–1879, 1998.

[15] N. Bloembergen and A. H. Zewail, "Energy redistribution in isolated molecules and the question of mode-selective laser chemistry revisited," *J. Phys. Chem.* **88**, pp. 5459–5465, 1984.

[16] P. Brumer and M. Shapiro, "Control of unimolecular reactions using coherent light," *Chem. Phys. Lett.* **126**, pp. 541–545, 1986.

[17] D. J. Tannor, R. Kosloff, and S. A. Rice, "Coherent pulse sequence induced control of selectivity of reactions - exact quantum-mechanical calculations," *J. Chem. Phys.* **85**, pp. 5805–5820, 1986.

[18] D. J. Tannor and S. A. Rice, "Control of selectivity of chemical reaction via control of wave packet evolution," *J. Chem. Phys.* **83**, pp. 5013–5018, 1985.

[19] M. Dahleh, A. P. Peirce, and H. Rabitz, "Optimal-control of uncertain quantum-systems," *Phys. Rev. A* **42**, pp. 1065–1079, 1990.

[20] A. P. Peirce, M. A. Dahleh, and H. Rabitz, "Optimal-control of quantum-mechanical systems - existence, numerical approximation, and applications," *Phys. Rev. A* **37**, pp. 4950–4964, 1988.

[21] R. S. Judson and H. Rabitz, "Teaching lasers to control molecules," *Phys. Rev. Lett.* **68**, pp. 1500–1503, 1992.

[22] C. J. Bardeen, V. V. Yakovlev, K. R. Wilson, S. D. Carpenter, P. M. Weber, and W. S. Warren, "Feedback quantum control of molecular electronic population transfer," *Chem. Phys. Lett.* **280**, pp. 151–158, 1997.

[23] A. Assion, T. Baumert, M. Bergt, T. Brixner, B. Kiefer, V. Seyfried, M. Strehle, and G. Gerber, "Control of chemical reactions by feedback-optimized phase- shaped femtosecond laser pulses," *Science* **282**, pp. 919–922, 1998.

[24] R. J. Levis, G. M. Menkir, and H. Rabitz, "Selective bond dissociation and rearrangement with optimally tailored, strong-field laser pulses," *Science* **292**, pp. 709–713, 2001.

[25] M. Bergt, T. Brixner, B. Kiefer, M. Strehle, and G. Gerber, "Controlling the femtochemistry of $Fe(CO)_5$," *J. Phys. Chem. A.* **103**, pp. 10381–10387, 1999.

[26] B. J. Pearson, J. L. White, T. C. Weinacht, and P. H. Bucksbaum, "Coherent control using adaptive learning algorithms," *Phys. Rev. A* **6306**, pp. 063412(1–12), 2001.

[27] T. Brixner, N. H. Damrauer, P. Niklaus, and G. Gerber, "Photoselective adaptive femtosecond quantum control in the liquid phase," *Nature* **414**, pp. 57–60, 2001.

[28] C. Daniel, J. Full, L. Gonzalez, C. Lupulescu, J. Manz, A. Merli, S. Vajda, and L. Woste, "Deciphering the reaction dynamics underlying optimal control laser fields," *Science* **299**, pp. 536–539, 2003.

[29] J. M. Geremia and H. Rabitz, "Optimal identification of hamiltonian information by closed- loop laser control of quantum systems," *Phys. Rev. Lett.* **89**, pp. 263902(1–4), 2002.

[30] J. L. Herek, W. Wohlleben, R. J. Cogdell, D. Zeidler, and M. Motzkus, "Quantum control of energy flow in light harvesting," *Nature* **417**, pp. 533–535, 2002.

[31] J. M. Dela Cruz, I. Pastirk, M. Comstock, V. V. Lozovoy, and M. Dantus, "Use of coherent control methods through scattering biological tissue to achieve functional imaging," *PNAS* **101**, pp. 16996–17001, 2004.

[32] D. Yelin, D. Meshulach, and Y. Silberberg, "Adaptive femtosecond pulse compression," *Opt. Lett.* **22**, pp. 1793–1795, 1997.

[33] D. Meshulach, D. Yelin, and Y. Silberberg, "Adaptive real-time femtosecond pulse shaping," *J. Opt. Soc. Am. B* **15**, pp. 1615–1619, 1998.

[34] F. G. Omenetto, B. P. Luce, and A. J. Taylor, "Genetic algorithm pulse shaping for optimum femtosecond propagation in optical fibers," *J. Opt. Soc. Am. B* **16**, pp. 2005–2009, 1999.

[35] A. Efimov and D. H. Reitze, "Programmable dispersion compensation and pulse shaping in a 26-fs chirped-pulse amplifier," *Opt. Lett.* **23**, pp. 1612–1614, 1998.

[36] A. Efimov, M. D. Moores, B. Mei, J. L. Krause, C. W. Siders, and D. H. Reitze, "Minimization of dispersion in an ultrafast chirped pulse amplifier using adaptive learning," *Appl. Phys. B* **70**, pp. S133–S141, 2000.

[37] M. C. Chen, J. Y. Huang, and L. J. Chen, "Coherent control multiphoton processes in semiconductor saturable bragg reflector with freezing phase algorithm," *Appl. Phys. B* **80**, pp. 333–340, 2005.

[38] S. Xiling, J. M. Kahn, and M. A. Horowitz, "Compensation for multimode fiber dispersion by adaptive optics," **30**, pp. 2985–2987, 2005.

[39] A. M. Weiner, "Femtosecond pulse shaping using spatial light modulators," *Rev. Sci. Instrum.* **71**, pp. 1929–1960, 2000.

[40] E. Zeek, K. Maginnis, S. Backus, U. Russek, M. Murnane, G. Mourou, H. Kapteyn, and G. Vdovin, "Pulse compression by use of deformable mirrors," *Opt. Lett.* **24**, pp. 493–495, 1999.

[41] M. Hacker, G. Stobrawa, R. Sauerbrey, T. Buckup, M. Motzkus, M. Wildenhain, and A. Gehner, "Micromirror SLM for femtosecond pulse shaping in the ultraviolet," *Appl. Phys. B* **76**, pp. 711–714, 2003.

[42] M. Roth, M. Mehendale, A. Bartelt, and H. Rabitz, "Acousto-optical shaping of ultraviolet femtosecond pulses," *Appl. Phys. B* **80**, pp. 441–444, 2005.

[43] V. D. Kleiman, S. M. Arrivo, J. S. Melinger, and E. J. Heilweil, "Controlling condensed-phase vibrational excitation with tailored infrared pulses," *Chem. Phys.* **233**, pp. 207–216, 1998.

[44] G. M. H. Knippels, A. F. G. Vandermeer, R. Mols, P. W. Vanamersfoort, R. B. Vrijen, D. J. Maas, and L. D. Noordam, "Generation of frequency-chirped pulses in the far-infrared by means of a subpicosecond free-electron laser and an external pulse shaper," *Opt. Commun.* **118**, pp. 546–550, 1995.

[45] R. A. Kaindl, M. Wurm, K. Reimann, P. Hamm, A. M. Weiner, and M. Woerner, "Generation, shaping, and characterization of intense femtosecond pulses tunable from 3 to 20 μm," *J. Opt. Soc. Am. B* **17**, pp. 2086–2094, 2000.

[46] S. H. Shim, D. B. Strasfeld, E. C. Fulmer, and M. T. Zanni, "Femtosecond pulse shaping directly in the mid-IR using acousto-optic modulation," *Opt. Lett.* **31**, pp. 838–840, 2006.

[47] L. Windhorn, T. Witte, J. S. Yeston, D. Proch, M. Motzkus, K. L. Kompa, and W. Fuss, "Molecular dissociation by mid-ir femtosecond pulses," *Chem. Phys. Lett.* **357**, pp. 85–90, 2002.

[48] S. Chelkowski, A. D. Bandrauk, and P. B. Corkum, "Efficient molecular dissociation by a chirped ultrashort infrared-laser pulse," *Phys. Rev. Lett.* **65**, pp. 2355–2358, 1990.

[49] S. Chelkowski and G. N. Gibson, "Adiabatic climbing of vibrational ladders using raman transitions with a chirped pump laser," *Phys. Rev. A* **52**, pp. R3417–R3420, 1995.

[50] F. Eickemeyer, R. A. Kaindl, M. Woerner, T. Elsaesser, and A. M. Weiner, "Controlled shaping of ultrafast electric field transients in the mid-infrared spectral range," *Opt. Lett.* **25**, pp. 1472–1474, 2000.

[51] N. Belabas, J. P. Likforman, L. Canioni, B. Bousquet, and M. Joffre, "Coherent broadband pulse shaping in the mid infrared," *Opt. Lett.* **26**, pp. 743–745, 2001.

[52] T. Witte, K. L. Kompa, and M. Motzkus, "Femtosecond pulse shaping in the mid infrared by difference-frequency mixing," *Applied Physics B: Lasers and Optics* **76**, pp. 467–471, 2003.

[53] H. S. Tan, E. Schreiber, and W. S. Warren, "High-resolution indirect pulse shaping by parametric transfer," *Opt. Lett.* **27**, pp. 439–441, 2002.

[54] M. A. Watson, M. V. O'Connor, P. S. Lloyd, D. P. Shepherd, D. C. Hanna, C. B. E. Gawith, L. Ming, P. G. R. Smith, and O. Balachninaite, "Extended operation of synchronously pumped optical parametric oscillators to longer idler wavelengths," *Opt. Lett.* **27**, pp. 2106–2108, 2002.

[55] N. A. Naz, H. S. S. Hung, M. V. O'Connor, D. C. Hanna, and D. P. Shepherd, "Adaptively shaped mid-infrared pulses from a synchronously pumped optical parametric oscillator," *Opt. Express* **13**, pp. 8400–8405, 2005.

Chapter 2

The Adaptive Mid-infrared Pulse Shaping System

2.1 Introduction

A schematic of the intelligent MIR pulse shaper used in this work is shown in Fig. 2.1. Starting with a NIR mode-locked pump source delivering bandwidth-limited pulses, the pulse is spectrally broadened in a standard polarisation maintaining (PM) fibre using self-phase modulation (SPM). The chirped pulses are shaped using a spatial light modulator in a 4-f configuration [1] such that the spectral phase and/or amplitude of the pulse can be manipulated. The shaped NIR pulses are then transferred to the MIR regime using an optical parametric oscillator (OPO) to perform the frequency conversion. The MIR output pulse is consequently assessed, for example for peak intensity, and the information is sent to an optimisation algorithm run from a computer which then applies the next guess for the spectral phase and/or amplitude applied by the pulse shaper. This completes the learning loop of the adaptive shaper. Spectral phase and intensity measurements of the MIR pulses are measured using spectrographic techniques such as the FROG or sonogram which are reviewed in Chapter 3.

In this chapter the background and theory for the adaptive MIR pulse shaper components will be introduced. In Section 2.2 pulse shaping theory and shaping methods will

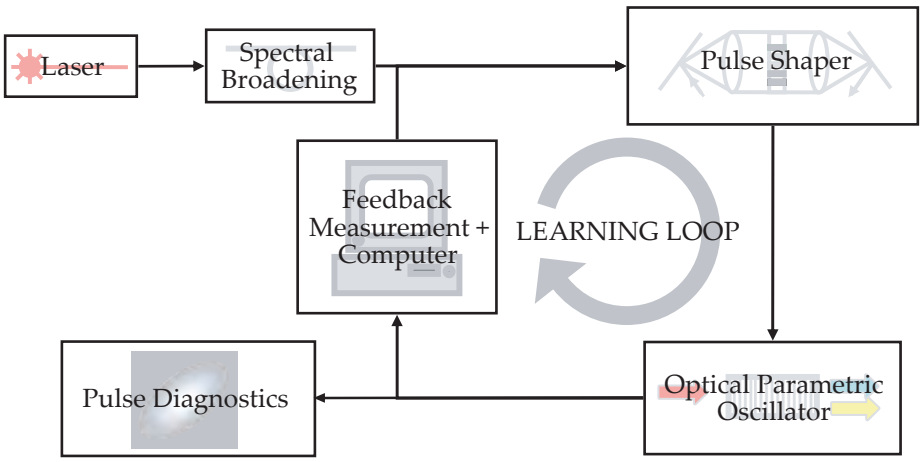

FIGURE 2.1: Schematic of adaptive MIR pulse shaping system.

be discussed followed by the theory of OPOs in Section 2.3, which begins with basic nonlinear optics extending to parametric gain and other parametric processes. Finally, a review of optimisation algorithms in Section 2.4 will conclude this chapter.

2.2 Pulse Shaping

With the development of ultrashort pulse laser systems, pulse shaping has become an important experimental tool with widespread applications in addition to the previously discussed application of coherent control of molecules. Adaptive coherent control has also been used in biomedical imaging applications, for multiphoton microscopy techniques [2–4] and coherent anti-Stokes Raman scattering (CARS) microscopy [5, 6].

Programmable pulse shaping has been applied to areas such as telecommunications where, dispersion compensation of femtosecond pulses through long fibre links has been shown using phase only shaping [7–9]. The application of dispersion compensation of femtosecond pulses is a useful approach for optical code division multiple access (CDMA) systems [10] where phase shaping has been used to encode and decode pulses and with dispersion compensation.

Dispersion compensation also has applications in CPA systems where a SLM is placed at the Fourier plane of a grating stretcher [11, 12], and has recently been used in high power

fibre CPA systems for amplitude-only [13, 14] and phase-only [15] adaptive shaping. Results of this last experiment will be shown later in Chapter 7.

2.2.1 Pulse Shaping Theory

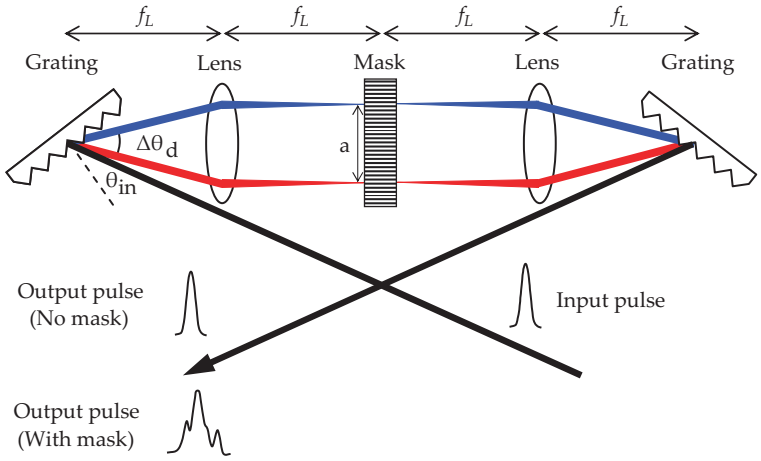

FIGURE 2.2: A pulse shaper arranged in a 4-f configuration where there is zero dispersion with no mask present.

Pulse shaping for arbitrary shapes requires control over spectral phase and amplitude, which can be achieved in a variety of ways. The most widely used set up is shown in Fig. 2.2 and is one that was originally introduced by Froehly [16] but later updated by Weiner [17] for ultrashort pulse applications. The pulse shaper consists of two diffraction gratings, two lenses and a mask. Each component is separated by the focal length, f_L, of the lenses in a set up known as the 4-f configuration or a zero-dispersion pulse shaper such that, when no mask is present, the output pulse is unchanged. The first diffraction grating spatially disperses the input pulse such that different frequencies are diffracted at different angles. The lens then focuses each frequency component at the focal plane or the Fourier plane (FP) one focal length after the lens. Here the pulse can be temporally shaped with a mask to apply changes in phase, amplitude or both to each individual frequency component. The second lens and diffraction grating then spatially recombine all the frequencies into a single collimated beam of shaped pulses.

When designing a pulse shaping system the design parameters should be chosen such that sufficient resolution and spatial dispersion can be achieved within the physical constraints of the optics. We begin with the grating equation for the dispersion of the

system,

$$\sin\theta_d = \frac{m\lambda}{d} - \sin\theta_{in}\ , \tag{2.1}$$

where m is the grating order, λ is the central wavelength, d is the grating period, and θ_{in} and θ_d are the input and diffracted angles of the grating, respectively. The angular dispersion, D, of a grating is given by differentiating Eqn. 2.1,

$$D = \frac{d\theta_d}{d\lambda} = \frac{m}{d\cos\theta_d}\ . \tag{2.2}$$

With this relationship, we can determine the size of the beam at the FP for a pulse with bandwidth $\Delta\lambda$. The dispersion angle, $\Delta\theta_d$ can be written as,

$$\Delta\theta_d = D\,\Delta\lambda\ . \tag{2.3}$$

For small angles of $\Delta\theta_d$, the spatial extent of the beam at the FP, a, can be approximated to,

$$\begin{aligned} a &= f_L\Delta\theta_d \\ &= \frac{f_L\Delta\lambda}{d\cos\theta_d}\ , \end{aligned} \tag{2.4}$$

where f_L is the focal length and the diffraction order, m, has been set to 1. More generally, we can derive from Eqn. 2.4 the spatial dispersion, α,

$$\alpha = \frac{a}{\Delta\omega} = \frac{f_L\lambda^2}{2\pi cd\cos\theta_d}\ , \tag{2.5}$$

where $\Delta\omega$ is the pulse bandwidth in units of rad/s and c is the speed of light. Therefore, for a fixed grating period, variation of the spatial dispersion depends on the focal length and grating angle. Design considerations must ensure sufficient grating efficiency and the angle between the incident and diffracted beam must be large enough to accommodate the physical dimensions of the lens and shaping mask.

In order to understand such limitations as the resolution or space-time coupling of the shaping system, we consider the effect of the shaper on the electric field of the

beam. The mathematical description of the pulse shaping process is often referred to as linear filtering [1], an engineering concept that originates from arbitrary waveform generation of electrical signals. Shaping of the input pulse, $E_{in}(t)$, is characterised by an impulse response function $H(t)$ and the output pulse, $E_{out}(t)$ is described by the following convolution,

$$E_{out}(t) = E_{in}(t) \otimes H(t) \, . \tag{2.6}$$

In the frequency domain, Eqn. 2.6 can be written as,

$$\widetilde{E}_{out}(\omega) = \widetilde{E}_{in}(\omega)\widetilde{H}(\omega) \, , \tag{2.7}$$

where $\widetilde{E}_{out}(\omega)$, $\widetilde{E}_{in}(\omega)$, and $\widetilde{H}(\omega)$ are Fourier transforms of $E_{out}(t)$, $E_{in}(t)$, and $H(t)$, respectively. In order to relate the filter function, $\widetilde{H}(\omega)$, to the actual masking function, $\widetilde{M}(x)$, which describes the spatial distribution of the amplitude and phase transmission of the mask, we consider the electric field, with a Gaussian spatial distribution, immediately after the mask, $\widetilde{E}_m(x, \omega)$.

$$\widetilde{E}_m(x, \omega) \sim \widetilde{E}_{in}(\omega) exp \left[-\frac{(x - \alpha\omega)^2}{\mathrm{w}_0^2} \right] \widetilde{M}(x) \, , \tag{2.8}$$

where w_0 is the $1/\mathrm{e}^2$ (of intensity) spot size of each individual frequency component at the FP given by,

$$\mathrm{w}_0 = \frac{cos\,\theta_{in}}{cos\,\theta_d} \left(\frac{f_L \lambda}{\pi \mathrm{w}_i} \right) \, , \tag{2.9}$$

where w_i is the $1/\mathrm{e}^2$ radius of the collimated input beam. Equation 2.8 describes the field as a function of space and frequency where the masking function acts on the spatial beam profile as well as the field in frequency. Due to the finite size of each individual frequency at the mask, it is possible for different spatial parts of the single frequency component to see different optical retardation and/or transmittance. Such an event would occur, for example, over interpixel gaps or pixel edges, leading to spatial diffraction. Full analysis of the space-time coupling has been studied by Wefers and Nelson [18] who find that the effect of the mask is to introduce a time-dependent spatial shift. This shift is given by,

$$\frac{\Delta x}{\Delta t} = -\frac{cd \cos\theta_{in}}{\lambda} \, . \tag{2.10}$$

For the experimental setup described in Chapter 4, the time-dependent spatial shift, $\Delta x/\Delta t$, is calculated to be 0.095 mm/ps for a shaper arrangement with a grating density of 1714 g/mm, grating incident angle of 53.4 degrees and a centre wavelength of 1047 nm.

For negligible pulse front tilts, Eqn. 2.8 can be simplified to neglect the space-time coupling by rewriting the equation as a superposition of Hermite-Gaussian modes for which the fundamental Gaussian mode is not space-time coupled [19]. Higher order modes describe the spatial diffraction due to the mask and can be neglected if the spatial diffraction is expected to be small or if spatial filtering, such as focusing into a fibre, will be performed to eliminate these modes. The shaped field is therefore described by the lowest order Hermite-Gaussian mode whose coefficient is defined to be the filter function, $\widetilde{H}(\omega)$, and takes the following form [1, 19],

$$\widetilde{H}(\omega) = \left(\frac{2}{\pi \mathrm{w}_0^2}\right)^{1/2} \int_{-\infty}^{\infty} \widetilde{M}(x) \exp\left[-\frac{2(x-\alpha\omega)^2}{\mathrm{w}_0^2}\right] dx \,. \tag{2.11}$$

This equation shows that the filter function is simply the masking function, $\widetilde{M}(x)$ convolved with a Gaussian beam profile which has an effective 1/e spot size of $\mathrm{w}_0/\sqrt{2}$. This Gaussian profile determines the resolution limit of the shaper which can be equated to a full-width at half-maximum (FWHM) spectral resolution, $\delta\omega$,

$$\delta\omega = (\ln 2)^{1/2} \frac{\mathrm{w}_0}{\alpha} \,. \tag{2.12}$$

We can express the effect of the resolution in terms of the overall complexity that can be achieved with the shaper. This is important in the design considerations as ideally, one would want the maximum achievable complexity, η, to be at least as complex as the mask in terms of the number of pixels. Using Eqns. 2.5, 2.9 and 2.12,

$$\eta = \frac{\Delta\omega}{\delta\omega} = \frac{\Delta\lambda}{\lambda} \frac{\pi}{\sqrt{\ln 2}} \frac{\mathrm{w}_i}{d\cos\theta_{in}} \,. \tag{2.13}$$

The complexity can be improved by increasing the input spot size on the grating as this ultimately determines the resolution of the shaper. Note that for pixellated masks, the sharp stepwise features are smeared out by the shaper resolution. This effect will be discussed in more detail later.

From Fourier theory, a limit in the frequency domain infers a limit in the time domain. Writing the convolution relation in Eqn. 2.11 in terms of the inverse Fourier Transform, gives a simple relation for the impulse response, $H(t)$,

$$H(t) = M(t)G(t)\,, \tag{2.14}$$

where $M(t)$ is the inverse Fourier transform of $\widetilde{M}(\alpha\omega)$ and $G(t)$ is given by,

$$G(t) = \exp\left(-\frac{\mathrm{w}_0^2 t^2}{8\alpha^2}\right)\,, \tag{2.15}$$

Equation 2.15 describes a Gaussian envelope that restricts the time window of the shaper. The FWHM of this envelope is given by [1],

$$T = \frac{4\alpha\sqrt{\ln 2}}{\mathrm{w}_0} = \frac{2\sqrt{\ln 2}\mathrm{w}_i\lambda}{cd\cos\alpha}\,, \tag{2.16}$$

This is related to Eqn. 2.12 for the resolution by the Fourier limit i.e. $T\delta f \cong 0.44$, where $\delta\omega = 2\pi\delta f$. Similarly, the total bandwidth, B, of the shaper is related to the temporal resolution, δt by $B\delta t \cong 0.44$ and the complexity of the shaper can be expressed as,

$$\eta = \frac{\Delta\omega}{\delta\omega} = \frac{B}{\delta f} = \frac{T}{\delta t}\,. \tag{2.17}$$

The time window sets a temporal limit on the pulse shaper such that, for example, a bandwidth limited pulse cannot be stretched more than the time window by the phase imparted by the mask. However, it is still possible to shape a pulse that is longer than the time window, as one might wish to do in the case of a fibre CPA system, for example. Numerical modelling of a pulse shaping using Eqns. 2.7 and 2.14, and their equivalent convolution relations, has been carried out to demonstrate this. Consider a bandwidth-limited 1 ps pulse shaped in a phase-only pulse shaper with a sinusoidal phase, and a time window of ∼20 ps. Figure 2.3(a) shows this theoretical pulse where the time window (blue solid) is larger than the pulse width (black solid). The shaped output, as a result of the sinusoidal phase from the phase-shaper, is shown in red in Fig. 2.3(a) and the spectral intensity profile is unchanged. The spectral intensity of the shaped and unshaped pulses are shown in Fig. 2.3(b) with the group delay of the output pulse

also shown. Now consider the case where a large linear chirp is applied to the pulse, stretching it to 55 ps, such that the pulse is now longer than the time window as shown by the solid curve in Fig. 2.3(b). However, after shaping this pulse and then having a matched re-compression stage after the shaper, the output pulse (red) is identical to the case of the bandwidth limited input pulse. Therefore shaping a stretched pulse that is larger than the time window can be achieved and should yield identical results to an unstretched pulse. This is useful to note for chirped pulse amplification (CPA) schemes where the stretched pulse has a low peak power so as not to damage the shaping optics and therefore could be used, for example, to compensate for nonlinear effects before re-compression. An experiment involving adaptive phase shaping in a high power fibre CPA system will be discussed later in Chapter 7.

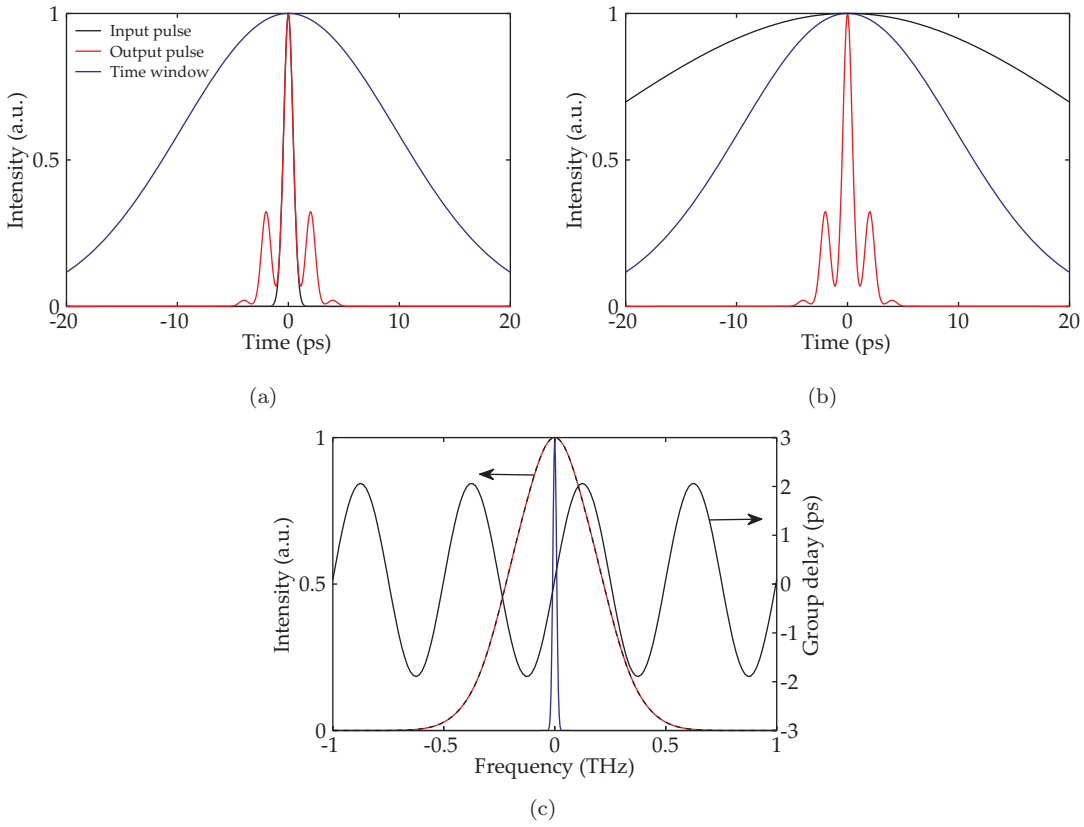

FIGURE 2.3: A bandwidth limited and linearly chirped pulse are shaped with a sinusoidal phase. The numerical results for bandwidth limited (a) and linearly chirped pulse (b) are shown with the input pulse (solid), the shaped output pulse (red) and the time window (blue). (c) The spectral intensity for both input pulses are identical. The results in this subfigure are therefore relevant to both types of pulse. The input (dashed) and output spectrum (red) are shown with the spectral resolution (blue). The group delay for the output pulse is also shown here (solid).

As mentioned previously, for pixellated masks, the sharp features between pixels are smoothed out by the resolution. The complexity of the shaper as defined by the resolution must be at equal to or better than the complexity imposed by the mask. Using a similar pulse shaping model to the one described above, this effect is demonstrated here. Figure 2.4 shows the effect of increasing the resolution of a shaper with a binary amplitude mask. The mask is comprised of 22 pixels and covers a total bandwidth of 1.4 THz. Using Eqn. 2.17 where $\eta = 22$, the maximum resolution is 0.06 THz. Figure 2.4(a) shows the shaped output pulse for a high resolution shaper where the spectral resolution can be considered as a delta function as shown in blue. As the resolution changes from a FWHM of 0.02 THz in Fig. 2.4(b), 0.03 THz in Fig. 2.4(c), and finally to the resolution limit of 0.06 THz in Fig. 2.4(d), it is clear that the sharp features of the mask are smeared out. At the resolution limit, where the complexity is equal to the mask complexity, the shaped pulse is not well resolved at the zeros of the amplitude mask. It is therefore advisable for the shaper complexity to be at least twice the complexity of the mask, as is the case in Fig. 2.4(c).

Having discussed the resolution and time window limitations of the pulse shaper optics, we now discuss further limitations imposed by pixellated masks.

Most pixellated devices can apply a maximum phase of a few π. In theory, a phase of 2π is sufficient since the phase profile can be wrapped within the shaper limits. However, phase wrapping results in abrupt changes in phase between pixels leading to parts of the beam being diffracted out of the main beam. These are known as phase-to-amplitude distortions [1] that result from the finite size of each individual frequency.

Another consequence of the pixellated mask is the limit imposed on the complexity of the phase profile. The sampling theorem [20], derived from information theory, states that for a signal whose highest frequency component is B, the sampling must be acquired at a minimum rate, termed the Nyquist frequency, of 2B. Therefore, for a mask of N_{pix} pixels, the maximum number of modulations that can be sampled is $N_{pix}/2$. For example, a binary (0-π) phase mask, where alternate pixels are programmed to apply a phase shift of π, is the most complex profile that can be achieved. One pixel corresponds to half of a cycle of the highest frequency component that can be sampled. In other words, the

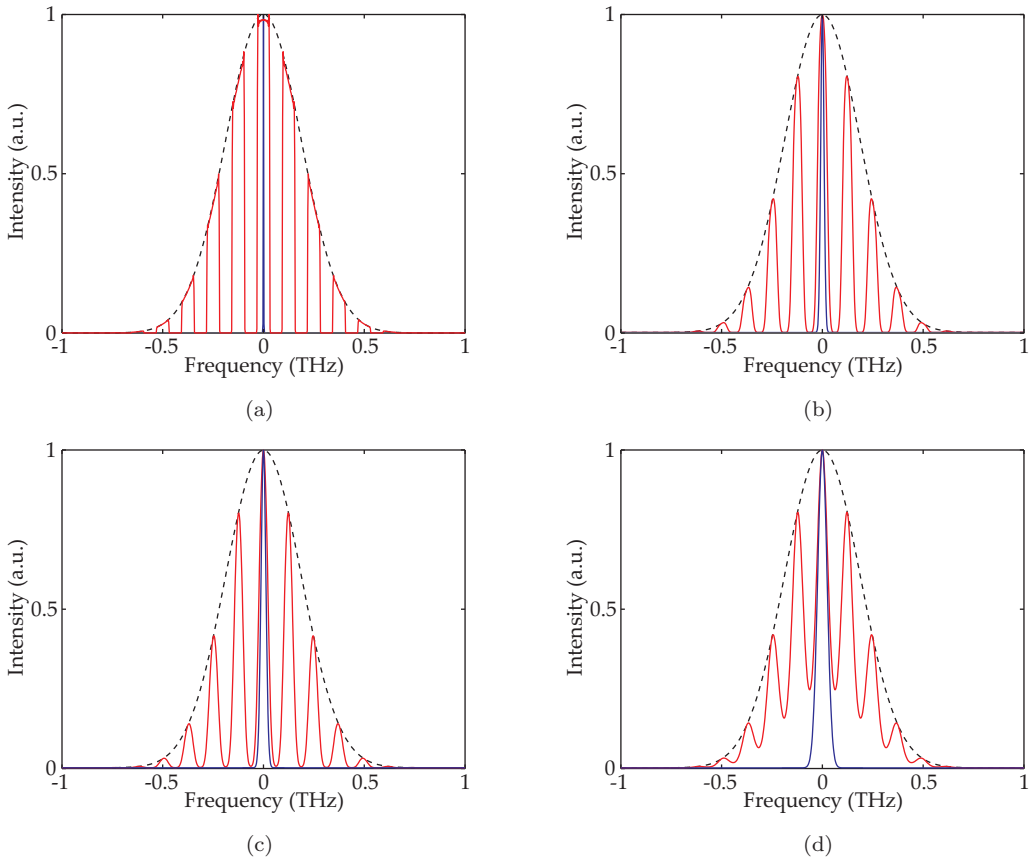

FIGURE 2.4: Numerical spectral intensity data for a 22-pixel binary amplitude mask for spectral resolutions of (a) near delta function, (b) FWHM 0.02 THz, (c) FWHM 0.03 THz, and (d) FWHM 0.06 THz. The unshaped frequency spectrum (dashed), shaped spectrum (red) and spectral resolution (blue), are shown.

maximum phase change between pixels is π. Thus the maximum rate of change of phase with frequency $d\phi/d\omega$ is,

$$\left.\frac{d\phi}{d\omega}\right|_{max} = \pm\frac{\pi}{\Delta\omega_{\text{pix}}}\,, \tag{2.18}$$

where $\Delta\omega_{\text{pix}}$ is the frequency span of one pixel. In the case of phase-only pulse shaping, an efficient way of representing the phase applied to each pixel of the mask is to approximate the phase distribution with a Taylor Series expansion [11, 21].

$$\begin{aligned}\phi(\Omega) &= \phi_0 + \left.\frac{d\phi}{d\Omega}\right|_0\Omega + \frac{1}{2!}\left.\frac{d^2\phi}{d\Omega^2}\right|_0\Omega^2 + \frac{1}{3!}\left.\frac{d^3\phi}{d\Omega^3}\right|_0\Omega^3 + \frac{1}{4!}\left.\frac{d^4\phi}{d\Omega^4}\right|_0\Omega^4 + \ldots \\ &= \beta_0 + \beta_1\Omega + \beta_2\frac{\Omega^2}{2!} + \beta_3\frac{\Omega^3}{3!} + \beta_4\frac{\Omega^4}{4!} + \ldots\,,\end{aligned} \tag{2.19}$$

where β_n corresponds to the nth order dispersion parameters of the phase, and $\Omega = \omega - \omega_0$

is the frequency detuning from the centre frequency ω_0 which, in general, coincides with the centre pixel. β_0 is is a constant offset and merely sets the level of reference and β_1, describes overall group delay (or linear phase) of the pulse. β_2, β_3, and β_4 are the dispersion terms corresponding to group delay dispersion (GDD), third order dispersion (TOD), and fourth order dispersion (FOD), respectively. By considering each of these dispersion parameters individually, we can derive the maximum values that can be applied before reaching the Nyquist limit [21].

For a purely linear phase,

$$\phi(\Omega) \;=\; \beta_{1_{max}}\Omega\,, \tag{2.20}$$

$$\Rightarrow \qquad \left.\frac{d\phi}{d\omega}\right|_{max} = \beta_{1_{max}}\,. \tag{2.21}$$

Equating this to Eqn. 2.18 gives,

$$\beta_{1_{max}} = \pm\frac{\lambda_0^2}{2\pi c\Delta\lambda_{pix}}\,, \tag{2.22}$$

where $\Delta\lambda_{pix}$ is the wavelength span of one pixel. Similarly, by making the assumption that $\Delta\omega_{pix}$ is constant across all N_{pix} pixels, the maximum GDD to FOD terms can be derived,

$$\beta_{2_{max}} \;=\; \pm\frac{\lambda_0^4}{2N_{pix}\pi c^2\Delta\lambda_{pix}^2}\,, \tag{2.23}$$

$$\beta_{3_{max}} \;=\; \pm\frac{\lambda_0^6}{N_{pix}^2\pi^2 c^3\Delta\lambda_{pix}^3}\,, \tag{2.24}$$

$$\beta_{4_{max}} \;=\; \pm\frac{3\lambda_0^8}{N_{pix}^3\pi^3 c^4\Delta\lambda_{pix}^4}\,. \tag{2.25}$$

In general,

$$\beta_{n_{max}} = \pm\frac{(n-1)!}{2}\frac{\lambda_0^{2n}}{(N_{pix}\pi)^{n-1}(c\Delta\lambda_{pix})^n}\,. \tag{2.26}$$

Note that these equations only give values for purely nth order dispersion and hence only

provide an indication of the shaper limits. For a combination of dispersion parameters, the Nyquist limit may be reached before the absolute limits derived from Eqn. 2.26.

2.2.2 Spatial Light Modulators

For the purposes of programmable pulse shaping, the shaping mask must be a variable mask. Spatial light modulators (SLMs) are programmable phase masks that can variably control the amplitude and phase of the pulse. There are several types of SLMs using liquid crystals, acousto-optic modulators, and deformable mirrors. Comprehensive reviews of pulse shapers can be found in Refs. [1, 22] but a few examples of SLMs are discussed in this section.

2.2.2.1 Acousto-Optic Devices

Acousto-optic modulators (AOM) are used to shape pulses in the same 4-f configuration but the pulses are incident on the AOM at the Bragg angle [22] (see Fig. 2.5). Acoustic waves are generated in the AOM crystal, e.g. TiO_2 and InP, through an electrically driven transducer from which the resulting sound wave induces refractive index changes due to the stresses caused by the wave. Since the acoustic wave travels at a much slower rate than the passing light wave, the pulse sees the crystal as a fixed diffraction grating. Ultrashort pulse shaping requires that the pulse repetition rate of the laser is synchronised with the driving electric field of the AOM. The speed of the acoustic wave therefore limits the repetition rate to $\sim$1MHz.

The phase and amplitude of the sound wave translate directly to the phase shift and diffraction efficiency of the frequencies at each point on the Fourier plane allowing for simultaneous modulation of phase and amplitude.

Another type of acousto-optic pulse shaping device is the acousto-optic programmable dispersive filter (AOPDF) [23], commercially known as the Dazzler. In contrast to the previously described setup, the AOPDF does not require complex alignment of optics as the entire shaping process occurs within the AOM crystal. It involves the optical pulse co-propagating with the sound wave in a birefringent crystal, in which the chirped

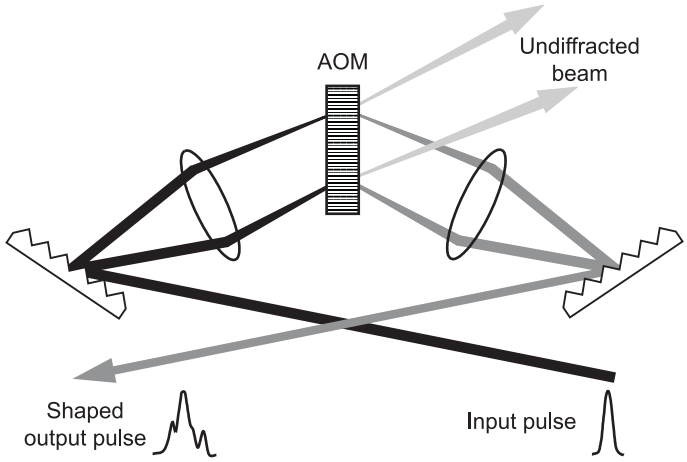

FIGURE 2.5: Schematic of a 4-f pulse shaper with an AOM set at the Bragg angle. The diffraction efficiency induced by the acoustic wave determines the amplitude of the frequencies.

acoustic wave rotates the polarisation of specific optical frequencies at different points along the crystal. The beam enters the crystal parallel to the fast axis and the phase shift imposed on an optical frequency depends on the position in the crystal at which the polarisation is rotated to the slow axis. The efficiency (or amplitude) of this rotation is controlled by the acoustic power and the position at which the optical frequency is rotated depends on the frequency pattern of the sound wave.

2.2.2.2 Liquid Crystal Modulators

A liquid crystal modulator (LCM) consists of an array of individually addressable pixels containing long, rod-like molecules whose orientation depends on the voltage applied. When no field is applied, the molecules are aligned along the crystal's extraordinary axis, and applying an electric field, causes them to tilt towards this external field axis. Light that is polarised along the crystal axis experiences a refractive index that is related to the degree of tilt. No tilt, corresponds to extraordinary refractive index (maximum retardation), whilst maximum tilt corresponds to ordinary refractive index (minimum retardation). Therefore, by applying different voltages to each of the individual pixels, one can change the relative phase of discrete frequency components of a pulse.

Rotating the light polarisation by 45° to the crystal axis and then passing the beam through a polariser after the LCM, results in an amplitude modulator as the LCM

acts like an electrically driven variable wave plate. When dealing with both phase and amplitude, two liquid crystal (LC) arrays are used whose molecular orientation are angled at $\pm 45^\circ$ to the linearly polarised light and sandwiched between two polarisers.

Although the LCM has a refresh rate of ms (compared to μs in an AOM) and the pixels discretise the frequency distribution, it has a much higher transmission and no limitations on the laser repetition rate.

2.3 Optical Parametric Oscillators

The conversion of IR to MIR radiation required for the MIR pulse shaping system is achieved through a nonlinear parametric process known as difference-frequency generation. This process forms the basis of the SPOPO which hosts the frequency conversion.

2.3.1 Difference-Frequency Generation

The effect of an electric field, $\mathbf{E}$, on a material can be described as forced oscillations of the constituent atoms or molecules, now acting as dipoles. Driving these molecules gently, causes an induced polarisation, $\mathbf{P}$, resulting in the emission of radiation at the same frequency as the original $\mathbf{E}$ field. The equation for $\mathbf{P}$ is given by,

$$\mathbf{P} = \epsilon_0 \chi^{(1)} \mathbf{E} \,, \tag{2.27}$$

where ϵ_0 is the electric permittivity of free space and $\chi^{(1)}$ is the linear susceptibility. At high intensity, the polarisation equation is no longer linear and higher order terms have to be considered. The general equation can be written as a power series,

$$\mathbf{P} = \epsilon_0 \left[\chi^{(1)} \mathbf{E} + \chi^{(2)} \mathbf{E}^2 + \chi^{(3)} \mathbf{E}^3 + \ldots \right] \,, \tag{2.28}$$

where $\chi^{(2)}$ and $\chi^{(3)}$ are the second and third order nonlinear susceptibilities, respectively. The second order nonlinear polarisation, $\mathbf{P}^{(2)} = \epsilon_0 \chi^{(2)} \mathbf{E}^2$, is responsible for processes such as second-harmonic generation (SHG), sum-frequency generation (SFG)

and difference-frequency generation (DFG). This can be shown by considering the combined electric field, E, of two linearly polarised beams, ω_3 and ω_2, incident on a nonlinear crystal.

$$E = E_3 \exp\left[i\left(\omega_3 t - \mathbf{k_3}.\mathbf{r}\right)\right] + E_2 \exp\left[i\left(\omega_2 t - \mathbf{k_2}.\mathbf{r}\right)\right] + c.c.\,, \tag{2.29}$$

where $\mathbf{k_j}$ is the momentum wavevector, $\mathbf{r}$ is the resultant vector from spatial coordinates $\mathbf{x}$, $\mathbf{y}$, $\mathbf{z}$ and "*c.c.*" denotes the complex conjugate. Substitution of Eqn. 2.29 into the second order nonlinear polarisation results in,

$$\begin{aligned} P^{(2)} &= \epsilon_0\chi^{(2)}\Big\{2\left|E_3\right|^2 + 2\left|E_2\right|^2\Big\} \\ &\quad + \epsilon_0\chi^{(2)}\Big\{E_3^2\exp\left[2i(\omega_3 t - \mathbf{k_3}.\mathbf{r})\right] + E_2^2\exp\left[2i(\omega_2 t - \mathbf{k_2}.\mathbf{r})\right] \\ &\quad + 2E_3E_2^*\exp\left[i\left((\omega_3+\omega_2)t - (\mathbf{k_3}+\mathbf{k_2}).\mathbf{r}\right)\right] \\ &\quad + 2E_3E_2^*\exp\left[i\left((\omega_3-\omega_2)t - (\mathbf{k_3}-\mathbf{k_2}).\mathbf{r}\right)\right] \\ &\quad + c.c\Big\}\,. \end{aligned} \tag{2.30}$$

The first line of Eqn. 2.30 is recognised as the optical rectification term and the second line is the SHG for the individual fields. SFG is given by the third line, and finally, DFG in the fourth.

Difference frequency generation is a process in which a pump photon at frequency ω_3 is stimulated to split, by a signal photon at ω_2, into a signal and idler photon at ω_2 and ω_1, respectively as shown in Fig. 2.6(a). In this process, energy conservation requires that the idler frequency is given by,

$$\hbar\omega_1 = \hbar\omega_3 - \hbar\omega_2\,, \tag{2.31}$$

where $\hbar$ is the reduced Planck constant. This equation shows that for every idler photon that is generated, a pump photon is lost and a signal photon is gained. Therefore, the

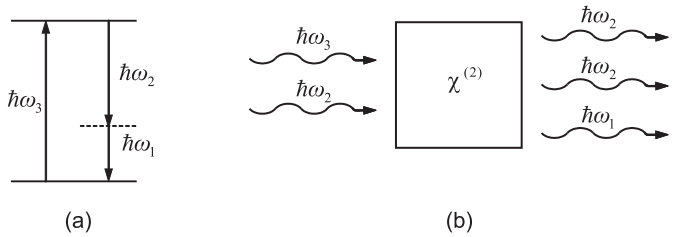

FIGURE 2.6: (a) Energy level diagram illustrating DFG; (b) Difference frequency generation in a nonlinear medium.

pump field depletes as it passes through the crystal, generating more signal (and idler) and hence amplifying the initial signal field. This is known as parametric amplification and is illustrated in Fig. 2.6(b).

It follows that the momentum must also be conserved in this process, such that,

$$\Delta k = k_3 - k_2 - k_1 = 0\,, \tag{2.32}$$

where k_3, k_2 and k_1 are the wavevectors corresponding to the pump, signal and idler, respectively. Note that here, we have assumed a collinear arrangement so that the wavevector is now a scalar. This equation is often referred to as the phase-matching condition. Satisfying Eqn. 2.32 is essential to achieving parametric gain in a nonlinear crystal. A detailed proof of this can be found in Ref. [24, chap. 2], meanwhile, the details of how phase matching might be achieved are shown later in Section 2.3.2.

The parametric gain achieved in a single pass DFG process, also known as an optical parametric amplifier (OPA), can be significantly enhanced with feedback operation by placing a $\chi^{(2)}$ material in a cavity to resonate the signal or idler (or both) wavelengths. If the cavity mirrors are set to be reflective at both the signal and idler wavelengths, then the OPO is known as a doubly resonant oscillator (DRO). In a singly resonant oscillator (SRO), only the signal (or idler) are reflected and the OPO oscillates on the cavity mode that most closely satisfies the phase-matching condition, i.e. the peak of the gain curve. However, for DROs, the cavity can only oscillate where the two wavelengths result in energy conservation, momentum conservation, and where the cavity modes coincide. The DRO will oscillate on the coincident cavity modes that are closest to the peak of the gain curve but this could still be far from the peak. Therefore, although DROs

theoretically have a much lower threshold than SROs, they are very unstable since small changes in the cavity length or pump wavelength could cause the cavity modes to jump.

Figure 2.7 shows a diagram of a singly resonant OPO in a bow-tie configuration. The curved mirrors act to focus the generated signal beam to a tight spot in the nonlinear crystal. The ideal case assumes near confocal focusing for maximum gain [25]. This configuration also allows the distance between the flat mirrors to be tuned such that the round-trip time is equal to the pump repetition period, without greatly affecting the signal spot size within the nonlinear crystal. The synchronously pumped optical parametric oscillator (SPOPO) leads to the resonating signal pulse experiencing further amplification within the crystal as it coincides with each successive pump pulse.

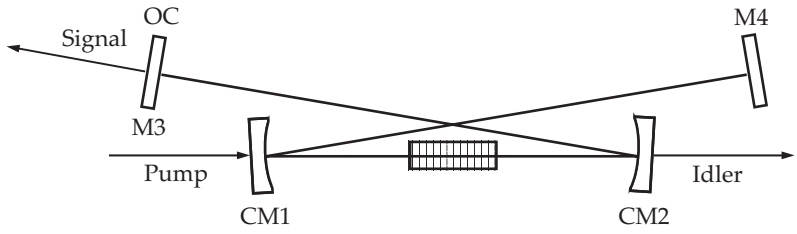

FIGURE 2.7: Schematic of a SPOPO arranged in bow-tie configuration with curved mirrors, CM1 and CM2, and flat mirrors, M3 and M4 where M3 is an output coupler (OC) for the signal beam.

2.3.2 Phase-Matching

In the case of normal dispersion in an isotropic crystal, phase-matching cannot be achieved. However, a crystal property whereby the refractive index depends on the polarisation of the fields, known as birefringence, allows for perfect phase-matching [26]. This requires careful selection of wavelengths in a limited phase-matching range. Tuning within this range can be achieved through very careful alignment of the crystal but gain efficiency is affected due to the spatial walk-off between the ordinary and extraordinary rays. Another technique that can be used is known as quasi-phase-matching (QPM) [27] and is described in the remainder of this section.

In a non-phase-matched bulk crystal, parametric generation of the signal field follows a sinusoidal relationship such that gain can be achieved up to a point where the pump,

signal and idler are π out of phase. The distance over which this occurs is known as the coherence length, L_c, and is given by,

$$L_c = \frac{\pi}{\Delta k} , \tag{2.33}$$

By careful fabrication of the bulk crystal, one can manipulate the gain that occurs over L_c to occur over a significantly longer length. This can be achieved by flipping the orientation of the crystal domains every L_c which has the effect of inverting the sign of the sinusoidal gain to result in a continuous growth of the signal and idler fields over the entire length of the crystal, as illustrated in Fig. 2.8. Note that the emission of a

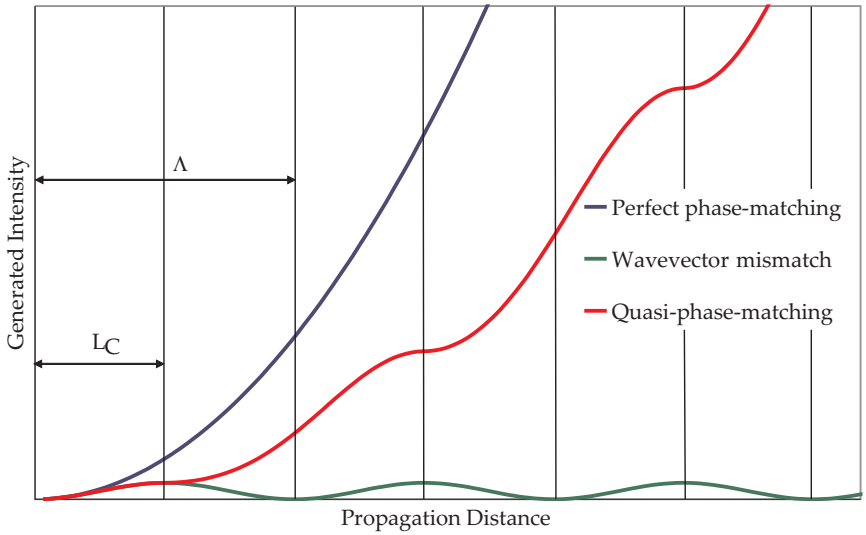

FIGURE 2.8: Illustration of the parametric generation for $\Delta\mathbf{k}$=0, $\Delta\mathbf{k}\neq$0 and a quasi-phase-matched crystal of poling period Λ.

signal and idler photon can occur without an initial signal field through spontaneous two-photon emission. In this process, the signal wavelength will be determined by the poling period, Λ, of the crystal allowing for a potentially wavelength-tunable device, and is given by,

$$\Lambda = 2L_c = \frac{2\pi}{k_G} , \tag{2.34}$$

where k_G is the grating wavevector, such that the phase mismatch must be rewritten as,

$$k_{QPM} = k_3 - k_2 - k_1 - k_G . \tag{2.35}$$

Due to the relative ease with which it is poled and its large effective nonlinear coefficient,

periodically poled lithium niobate (PPLN) is the preferred choice of material in this work. Lithium niobate ($LiNbO_3$ or LN) is a uniaxial ferroelectric crystal whose crystal domains can be easily inverted using *ferroelectric domain engineering* whereby a strong electric field is applied to patterned electrodes which map out the periodically poled structure. This nonlinear material allows idler wavelengths of up to 7μm [28] but further work at even longer wavelengths with other materials, e.g. CdSe [29] and GaAs [30], is anticipated in the future.

It should be noted that $LiNbO_3$ is prone to an effect, known as photorefraction, that causes local refractive index variations initiated by a propagating beam. This results in pulse distortions which can be avoided by heating the PPLN crystal to 100-200°C (N.B. the grating period is temperature dependent). However, by doping PPLN with MgO it is possible to reduce the photorefraction damage threshold such that the crystal will allow operation at room temperature [31].

The work in this thesis uses undoped PPLN operating at controlled temperatures in the range 100-200°C. Due to thermal expansion, the grating period varies with temperature and therefore allows for fine wavelength tuning. More coarse wavelength tuning is generally achieved by fabricating several grating periods on one crystal such that a simple translation of the crystal will allow access to another grating period.

2.3.3 Parametric Gain

From Maxwell's wave equation one can derive a set of equations that describe the interaction of the pump, signal and idler field known as the coupled-wave equations [32, Chap. 3].

$$\frac{\partial A_3}{\partial z} + \frac{1}{u_3}\frac{\partial A_3}{\partial t} + i\frac{b_3}{2}\frac{\partial^2 A_3}{\partial t^2} = 2i\alpha_3 A_1 A_2 \exp[-i\Delta k z]\,, \tag{2.36}$$

$$\frac{\partial A_2}{\partial z} + \frac{1}{u_2}\frac{\partial A_2}{\partial t} + i\frac{b_2}{2}\frac{\partial^2 A_2}{\partial t^2} = 2i\alpha_2 A_1^* A_3 \exp[+i\Delta k z]\,, \tag{2.37}$$

$$\frac{\partial A_1}{\partial z} + \frac{1}{u_1}\frac{\partial A_1}{\partial t} + i\frac{b_1}{2}\frac{\partial^2 A_1}{\partial t^2} = 2i\alpha_1 A_2^* A_3 \exp[+i\Delta k z]\,, \tag{2.38}$$

where u_j is the group velocity and b_j is the group velocity dispersion, and collinear pulse propagation, along direction z, in a bulk crystal is assumed. The slowly varying envelope, $A_j = A_j(z,t)$, is defined by,

$$E_j(z,t) = A_j(z,t)\exp[i(k_j z - \omega_j t)] + \ c.c. \tag{2.39}$$

and,

$$\alpha_j = \frac{d_{eff}\omega_j}{cn_j}\ , \tag{2.40}$$

where $d_{eff} = \frac{1}{2}\chi^{(2)}$ is the effective nonlinear coefficient, and n_j is the refractive index at frequency ω_j.

Under the conditions of no dispersion and no pump depletion, it can be shown from Eqns. 2.37 to 2.38 that [24],

$$A_2(z) \propto \sinh(gL)\ , \tag{2.41}$$

$$A_3(z) \propto \cosh(gL)\ , \tag{2.42}$$

where L is the crystal length and g is,

$$g = \left[\Gamma^2 - \left(\frac{\Delta k}{2}\right)^2\right]^{1/2}\ , \tag{2.43}$$

and, Γ, the parametric gain coefficient is defined as,

$$\Gamma^2 = \frac{2\omega_1\omega_2\left|d_{eff}\right|^2 I_3}{n_1 n_2 n_3 \epsilon_0 c^3}\ , \tag{2.44}$$

where I_3 is the pump intensity, and all other parameters are as previously defined. In other words, Eqns. 2.41 and 2.42 state that for perfect phase matching, the amplitude of the signal and idler fields increases asymptotically with distance under the condition that $gL \gg 1$.

When considering the design of an OPO, it is important to calculate the bandwidth limits of the nonlinear crystal. From Eqn. 2.41 one can derive the single-pass incremental signal

gain [33, 34],

$$G_2(L) = \frac{|A_2(L)|^2}{|A_2(0)|^2} - 1 \tag{2.45}$$

$$= \Gamma^2 L^2 \frac{\sinh^2(gL)}{(gL)^2} , \tag{2.46}$$

In the limit of low gain, where $\Gamma^2 < (\Delta k/2)^2$, the gain $G_2(l)$ can be rewritten as,

$$G_2(L) = \Gamma^2 L^2 \frac{\sin^2(g'L)}{(g'L)^2} = \Gamma^2 L^2 \mathrm{sinc}^2(g'L) , \tag{2.47}$$

where $g' = ig$,

$$g' = \left[\left(\frac{\Delta k}{2} \right)^2 - \Gamma^2 \right]^{1/2} , \tag{2.48}$$

From Eqn. 2.47, the gain bandwidth is defined by $g'L = \pi$ where $G_2(L) = 0$ at the first minimum of the sinc function. If $\Gamma^2 L^2 \ll \pi^2$, then the gain function can be approximated to a $\mathrm{sinc}^2(\Delta k L/2)$ relationship for which the FWHM signal gain bandwidth, is given by,

$$\Delta\Omega_2 \simeq \left| \frac{5.56}{\delta v_{21}\, L} \right| , \tag{2.49}$$

where $\Delta\Omega_2$ has units rad/s and $\delta v_{21} = 1/v_2 - 1/v_1$ is the group velocity mismatch (GVM) between the signal and idler. Equation 2.49 shows that the tolerance of parametric gain worsens as the walk-off ($\delta v_{21}\, L$) between the signal and idler pulses increases. $\Delta\Omega_2$ can therefore be maximised when the signal and idler group velocities are matched which can be most easily achieved when both have the same wavelength, i.e. under the condition that is known as *degeneracy*. Alternatively, increasing the gain bandwidth can be achieved by shortening the crystal length.

From Eqn. 2.49 one can derive a range of pump frequencies that can be used to operate the OPO under a fixed signal gain curve. This expression for the pump acceptance bandwidth is dependent on the pump-idler GVM and is given by,

$$\Delta\Omega_3 \simeq \left| \frac{5.56}{\delta v_{31}\, L} \right| . \tag{2.50}$$

The description for gain has so far assumed a plane wave analysis. Consideration of Gaussian beams in a near confocal focusing condition for pulsed operation, can lead to a useful estimation of oscillation threshold. A Gaussian beam analysis of focused beams in an OPO was first shown by Boyd and Kleinman [35]. They considered a continuous wave (CW), doubly resonant oscillator working at degeneracy and with the pump, signal and idler all with the same confocal parameter. Guha et al. [36] later investigated the parametric gain of a singly resonant oscillator with emphasis on having unequal confocal parameters of the interacting waves for optimum threshold. This work was then revisited and extended by Guha [25] to describe the conversion efficiency in the near-threshold regime as well as incorporating linear absorption of the interacting waves and considering arbitrary focusing conditions.

For synchronous pumping, one has to consider the temporal walk-off between interacting pulses due to GVM. McCarthy et al. [37] build on a simple plane wave analysis introducing factors to account for the spatial and temporal overlap of the beams, assuming collimated beams. The scenario of tight focusing conditions together with synchronous pumping, was approached by Hanna et al. [38] by heuristically combining the analyses of Guha [25] and McCarthy [37], resulting in the following expression for the threshold peak pump power,

$$P_{p,th} = \frac{n_p\, n_i\, \lambda_i^2\, \lambda_s\, c\, \epsilon_0}{128\, \pi^2 d_{eff}^2\, l_{eff}} \frac{\epsilon_s}{g_t\, \xi_s\, \mathrm{Re}\,(h_2)}\ , \tag{2.51}$$

where ϵ_s is the fractional power loss per round trip, and $g_t = [\tau_3^2/(\tau_3^2 + \tau_2^2)]^{1/2}$ for which τ_j is the pulse duration. The effective interaction length l_{eff}, as defined in Ref. [37], is a function of the crystal length and the GVM between the interacting pulses. The spatial component of l_{eff} is ignored in Hanna's approach [38] as the focusing conditions are considered in the term h_2, which is an integral originating from Guha's analysis [25]. Values for parameters defining this integral are provided in Ref. [25] for various focusing conditions. Finally, the confocal parameter ξ_s is defined as a ratio between the crystal length, L and the confocal length b_s.

Aside from careful choice of focusing conditions and crystal length, one must also consider the intracavity losses when designing an OPO. The oscillation threshold of an OPO is ultimately determined by the point at which these losses are overcome. Under the

conditions of small gain and low loss, a 'Findlay-Clay' analysis [39], a technique generally used for 4-level laser systems, can be applied to OPOs. Analysis of this begins with the plane wave expression for multiplicative gain (rather than incremental gain c.f. Eqn. 2.46) at $\Delta k = 0$,

$$G_{mult}(L) = \frac{|A_2(L)|^2}{|A_2(0)|^2} \tag{2.52}$$

$$= \cosh^2(\Gamma L) \, , \tag{2.53}$$

Taking into account the losses introduced by the output coupler reflectivity, R_M and the internal losses given by an effective reflectivity R_L, an expression at threshold can be written as,

$$R_L R_M \cosh^2(\Gamma L) = 1 \, , \tag{2.54}$$

which, in the limit of low loss, such that $\Gamma L \ll 1$, is reduced to,

$$\ln[\cosh^2(\Gamma L)] = -\ln R_L - \ln R_M \tag{2.55}$$

$$\Gamma^2 L^2 \simeq -\ln R_L - \ln R_M \, . \tag{2.56}$$

Since $\Gamma^2 \propto P_{th}$ (see Eqn. 2.44), where P_{th} is the average power at threshold, Eqn. 2.56 becomes,

$$K P_{th} = -\ln R_L - \ln R_M \, , \tag{2.57}$$

where K is a proportionality constant. By measuring the oscillation threshold for OPO arrangements with various output coupler reflectivities, it is possible to extrapolate the value of R_L from a plot of $-\ln R_M$ against P_{th} with a gradient K.

For the SPOPO arrangement used in Chapter 6 the Findlay-Clay analysis was applied to calculate the resonator loss. Using output couplers with reflectivities of 85% and 65%, oscillation thresholds of 200 and 300 mW were achieved, respectively. Using Eqn. 2.57 the OPO was calculated to have a resonator loss (1-R_L) of 13%. A significant part of this loss was due to 95% signal transmission through the PPLN crystal.

2.3.4 Parametric Transfer

A frequency domain analysis of DFG is carried out in this section, based on Refs. [40] and [41], to further understand the physical interpretation of the parametric process. Analysis of how the interacting pulses affects the transfer of the pulse shape from the pump to the idler is required for the development of the indirect MIR pulse shaper. We begin with the Fourier transform of Maxwell's wave equation, the second order nonlinear polarisation for DFG, and the definition of the electric field envelope given by,

$$\frac{\partial^2 \widetilde{E}(z,\omega)}{\partial z^2} + k(\omega)^2 \widetilde{E}(z,\omega) = -\mu_0 \omega^2 \widetilde{P}^{NL}(z,\omega)\,, \tag{2.58}$$

$$\widetilde{P}_1^{NL}(z,\Omega_1) = 2d\epsilon_0 \int_{-\infty}^{+\infty} \widetilde{E}_3(z,\Omega_2+\Omega_3)\widetilde{E}_2^*(z,\Omega_2)\, d\Omega_2\,, \tag{2.59}$$

$$\widetilde{E}_j(z,\Omega_j) = \widetilde{A}_j(z,\Omega_j) exp\left[ik(\omega_j+\Omega_j)\right] z\,, \tag{2.60}$$

where $\Omega_j = \omega - \omega_j$ is the frequency detuning from the central frequency, ω_j.

Using equations 2.58 to 2.60 and the slowly-varying envelope approximation, the following equation can be derived for the idler frequency-domain spatial envelope, $\widetilde{A}_1(L,\Omega_1)$. We assume plane wave interactions in the z direction of an isotropic medium of length L, through which there is no pump depletion and no signal amplification, such that,

$$\begin{aligned}
\widetilde{A}_1(L,\Omega_1) &= \int_{-\infty}^{+\infty}\int_0^L i\alpha_1 \widetilde{A}_3(\Omega_2+\Omega_1)\widetilde{A}_2^*(\Omega_2)\exp[i\Delta k_{DFG}(\Omega_2,\Omega_1)z]\, dz\, d\Omega_2 \\
&= \int_{-\infty}^{+\infty} i\alpha_1 \widetilde{A}_3(\Omega_2+\Omega_1)\widetilde{A}_2^*(\Omega_2) L\,\mathrm{sinc}\left[\Delta k_{DFG}(\Omega_2,\Omega_1)\frac{L}{2}\right] \\
&\qquad \times \exp\left[i\Delta k_{DFG}(\Omega_2,\Omega_1)\frac{L}{2}\right] d\Omega_2\,,
\end{aligned} \tag{2.61}$$

where, to a second order approximation, $\Delta k_{DFG}(\Omega_2,\Omega_1)$ is given by,

$$\Delta k_{DFG}(\Omega_2,\Omega_1) = \Delta k + \Omega_2\delta\nu_{32} + \Omega_1\delta\nu_{31} + \frac{1}{2}\left[\Omega_2^2\delta b_{32} + \Omega_1^2\delta b_{31} + b_3\Omega_2\Omega_1\right]\,, \tag{2.62}$$

where $\delta\nu_{jk}$ is the GVM parameter between the group velocities ν_j and ν_k,

$$\delta\nu_{jk} = \frac{1}{\nu_j} - \frac{1}{\nu_k} \quad , \quad \nu_j = \left[\frac{dk(\omega)}{d\omega}\right]^{-1}_{\omega=\omega_j} , \tag{2.63}$$

and δb_{jk} is the group velocity dispersion (GVD) mismatch between the group velocity dispersion parameters b_j and b_k,

$$\delta b_{jk} = b_j - b_k \quad , \quad b_j = \left.\frac{d^2k(\omega)}{d\omega^2}\right|_{\omega=\omega_j} . \tag{2.64}$$

If the interaction length of the crystal is small such that GVM (and GVD) can be neglected, Eqn. 2.61 reduces to a simple convolution,

$$\widetilde{A}_1(L,\Omega_1) \propto \widetilde{A}_3(\Omega_3) \otimes \widetilde{A}_2^*(\Omega_3 - \Omega_1) . \tag{2.65}$$

Moreover, complete transfer of the pump pulse envelope characteristics occur if $\widetilde{A}_2^*(\Omega_3 - \Omega_1)$ is a delta function. High fidelity transfer of the pump requires a very narrow signal spectrum and will be discussed in more detail in Chapter 5. Since pulse shapers are typically transparent in the visible and NIR wavelength regions, much of the work involved with indirect pulse shaping investigates the fidelity of spectral transfer from the NIR to the MIR [42–44] as well as to the UV region [45].

Equation 2.65 can be extended to OPOs, such that, in order to allow high fidelity spectral shape transfer of the pump to the idler, the signal spectrum must have a narrow spectral bandwidth compared to the pump. Previous work by Hanna et al. [38] has shown that replacing M4 in Fig. 2.7 with a diffraction grating can control the signal bandwidth. In addition, this configuration also benefits from agile tuning of the signal (and idler) using the grating tilt, which is less time consuming than adjusting the crystal temperature. Alternatively, a birefringent filter [46] or an etalon placed within the OPO has a similar effect but is much easier to implement.

High fidelity spectral transfer is not essential to demonstrating adaptive control, but it can significantly increase the resolution of control over MIR pulse shape and therefore the range of achievable pulse shapes. The importance of spectral transfer will be discussed both theoretically and experimentally later in Chapters 5 and 6.

2.4 Optimisation Algorithms

In this thesis, an algorithm is used to adaptively optimise the outcome of the system by controlling the individual pixels of the SLM of the pulse shaper. Information on the effect of the pulse shaping on the experiment being undertaken is used as feedback to the computer controlled algorithm completing the learning loop. With the wide breadth of optimisation algorithms available it is a challenging task to find the best algorithm required. The most important criteria for finding such an algorithm are fast convergence, efficient parameter searching to avoid being trapped in local optima, and ease of implementation. Many comparisons of optimisation algorithms have been made [47–49] claiming better performance of one type of algorithm over several others for specific functions. Overall, however, it seems that the best algorithm for the particular problem in hand can only ultimately be decided by comparison of a few short-listed algorithms. The two most widely used algorithms in this field are the evolutionary algorithms (EA) and simulated annealing (SA) algorithms although many hybrid algorithms have also been developed but will not be discussed here. In this section, details of some types of EAs and SAs will be discussed.

2.4.1 Evolutionary Algorithms

The optimisation process of evolutionary algorithms are so called because they mimic biological evolution. A typical EA process is outlined below:

1. A population of individuals which are uniquely encoded by a sequence of genes (i.e. optimisation parameters) is initialized.

2. A fitness function that can measure the fitness of each individual and return a single number is defined.

3. The individuals are then placed in rank order of fitness and some are selected to be parents of the next generation. This is achieved using recombination and mutation operators to create new offspring.

4. These new individuals are evaluated for fitness and the process, from steps 2 to 4, continues until a set number of iterations has occurred or the required level of fitness has been reached.

The implementation of a mutation promotes genetic diversity and prevents a particularly fit individual from dominating the population, resulting in premature convergence in a local minimum in parameter space. It is important that the algorithm has the ability to search as much of the parameter space as possible for the global optimum as well as being sensibly sized for efficiency. The ideal form of parameter space is one that is continually varying rather than one which is discontinuous or has very steep mountains and valleys where the algorithm could get trapped in a minimum that is not the global optimum. In the case of the EAs, it is very important to have a well defined fitness function to achieve a near optimum solution since reaching the global optimum is possible but not guaranteed.

Many different types of EA exist all with, most notably, varying approaches to achieving step (3) in the artificial evolutionary process described above. The two most commonly used EAs are genetic algorithms (GA) and evolutionary strategies (ES), both of which were initially independently formulated in the 1960s [50, 51]. For GAs, the new generation is typically achieved by first selecting half of the current population to reproduce. The recombination operator, i.e. production of new offspring, combines a section of the genes of one parent with the rest of genes of the other and vice-versa to generate two new individuals. This recombination operator, where the gene sequences of both parents are essentially spliced together is termed *crossover*. Most commonly, the individuals of GAs are represented as binary strings such that crossover operators can be easily achieved. In addition to this, a mutation operator, where e.g. a gene (or bit) is flipped, enhances the diversity of the generation and thus leads to faster convergence to an optimum solution.

ESs, on the other hand, usually encode individuals with real numbers so they can be represented as D-dimensional vectors, where D is the number of variables (or genes). The development of a new generation begins with a recombination step but each individual can parent several new individuals. In contrast to the GA, the ES search is driven by the mutation operator which adds a perturbation to each variable where the perturbation

is given by a normal distribution, $G(0, \sigma)$, with zero mean and a standard deviation of σ. For every generation of μ individuals, λ offspring are reproduced. The selection of individuals for the new generation has many schemes but commonly the ES follows a (μ, λ) selection, where the best μ individuals are taken from the offspring λ, or a $(\mu + \lambda)$ selection scheme is used, where the best μ individuals are chosen from the parents and offspring combined.

One particular type of ES that will be used in follow-on work from that presented in this thesis is *differential evolution* (DE) developed by Storn and Price [49]. In this method, the perturbation mechanism in the mutation stage is instead determined by the difference vector of two random individuals. Each individual from the parent population generates one offspring whose variables are either the same as the parent's or a mutated parent variable. The parent and offspring are then compared in the selection process and if the offspring yields a more desirable outcome, it becomes a member of the new generation, otherwise, the parent advances to the next generation. Variations on this method include careful choice of the individuals that make up a difference vector rather than random allocation and having perturbations based on two difference vectors rather than just one which has been observed to improve the population diversity. In Ref. [49] comparison with annealing methods and other EAs found that the DE algorithm outperformed all of these in almost all of the test functions. Recently, Fan and Lampinen [52] developed the *trigonometric mutation operation* in which the three random individuals are chosen but the individual to be perturbed is given by the centre of the vector triangle formed by the three individuals. The perturbation is then the sum of three weighted difference vectors where the weight depends on the outcome of each of the parents. Results from Ref. [52] found that the trigonometric DE outperformed the original DE in all of the test functions in terms of the speed of convergence.

2.4.2 Simulated Annealing

The SA, developed by Kirkpatrick et al. in 1983 [53], is based on a principle analogous to the heating and cooling (or the annealing) of a metal. If the metal is cooled slowly large crystals will form and after a long time of controlled cooling, it will form a single

pure crystal with no defects thereby reaching its minimum energy state. During this process, small amounts of heating may be required for the atoms to relocate to areas where they can crystallise more efficiently. The SA algorithm uses this technique of slowly lowering the temperature of the system in a controlled manner to find the global minimum. Each SA problem can be approached by imagining the parameter space as a range of mountains and valleys amongst which, one would like to find the lowest valley. The SA uses a bouncing ball in this landscape to find the minimum by initially giving the ball lots of energy such that it can easily bounce between the valleys. As the energy of the ball is slowly lowered, the ball can get trapped in a smaller range and survey the depths of the local valleys. It compares each one to the last saved lowest valley. If it is lower, it records the new lowest valley, and if it is higher, it either accepts it as the new "lowest" valley or moves on to assess the next one. In general, all SA techniques use the following procedure:

1. Define a *visiting distribution* or probability density of states for all D parameters. This determines the the next position of the ball in the D-dimensional parameter space.

2. Define the *acceptance probability* for solutions of higher energy than the previous ball position. This helps to prevent the ball from being stuck in local minima.

3. Define the *cooling schedule* to control how quickly the algorithm converges.

4. Define a starting position.

5. Sample the next position using the visiting distribution.

6. Assess whether this new position is to be accepted using the definition of the acceptance probability.

7. Reduce the temperature according to the cooling schedule.

8. Repeat steps 5-7 until convergence.

The acceptance criterion for most types of SA follow the well known Metropolis algorithm [54] and is given by,

$$P(x_t \rightarrow x_{j+1}) = \begin{cases} 1 & \text{if } E(x_{j+1}) < E(x_j) \\ \exp \frac{[E(x_j)-E(x_{j+1})]}{T(j)} & \text{if } E(x_{j+1}) \geq E(x_j)\,, \end{cases} \tag{2.66}$$

where $P(x_j \rightarrow x_{j+1})$ is the acceptance probability, and in keeping with the ball analogy, $x_{j,j+1}$ is the position of the ball at iteration number j and $j+1$, $E(x_{j,j+1})$ is the energy, and $T(j)$ is the "temperature" of the system. The form of the exponential in Eqn. 2.66 follows Boltzmann statistics, which is also the form of the visiting distribution defining the probability that a position will be visited. Annealing techniques that use this type of visiting distribution are known as *classical simulated annealing* (CSA). An optimum cooling schedule was developed by Geman and Geman [55] which showed that the CSA would always converge to the global optimum as $j \rightarrow \infty$ if the following cooling schedule was adopted,

$$T(j) = \frac{T_0}{\ln(1+j)}\,, \tag{2.67}$$

where T_0 is the initial temperature of the system. Although such a scheme guarantees convergence, the speed of convergence is usually very slow. Cooling schemes where the temperature drops very fast to speed up the convergence is known as *simulated quenching* (SQ), for which convergence to the global optimum is no longer guaranteed. The implementation of SQ should, in general, be used with caution such that there is a satisfactory trade-off between processing time and finding a good solution.

In 1987, Szu and Hartley [56] developed a faster SA technique named *fast simulated annealing* (FSA), which used a Cauchy-Lorentz visiting distribution in place of the Boltzmann distribution. The long tails of the Cauchy-Lorentz distribution give rise to the occasional long jump from a local search so that a global optimum might be found quicker. The FSA therefore has a faster cooling schedule and still guarantees optimal convergence as $j \rightarrow \infty$,

$$T(j) = \frac{T_0}{(1+j)}\,. \tag{2.68}$$

Another, yet faster algorithm called *adaptive simulated annealing* (ASA) was developed by Ingber [57, 58]. In this scheme the cooling schedules and visiting distributions exist for each individual parameter, which are adjusted as the algorithm progresses. The form of the visiting distribution is such that the cooling schedule follows an exponential decay and guarantees optimal convergence. The adaptive nature of the algorithm comes from *re-annealing*. This process increases the temperature every e.g. one hundred iterations such that long jumps can be made, further sampling the parameter space. The increase in temperature is dependent on the sensitivity of each parameter at the time of re-annealing, resulting in adaptive behaviour. An SA algorithm based on Ingber's ASA has been used for the work presented in Chapter 4.

The final type of SA considered in this section is the *generalized simulated annealing* (GSA) algorithm originally developed by Tsallis and Stariolo [59] in 1996. The GSA combines the CSA and the FSA for a more general visiting distribution and acceptance probability. The scheme introduces four convergence parameters; q_v controls the shape of the visiting distribution as well as the cooling rate, which defines the visiting temperature T_v at each iteration, and the parameter q_a controls shape of the the acceptance probability, which is also dependent on the acceptance temperature T_a. The acceptance probability is generalised to,

$$P(x_j \to x_{j+1}) = \begin{cases} 1 & \text{if } E(x_{j+1}) < E(x_j) \\ \frac{1}{[1+(q_a-1)(E(x_{j+1})-E(x_j))/T_a(j)]^{1/(q_a-1)}} & \text{if } E(x_{j+1}) \geq E(x_j)\,, \end{cases} \tag{2.69}$$

and the visiting distribution [59, Eqn. 21] requires the cooling schedule to be,

$$T_v(j) = T_v(1)\frac{2^{q_v-1}-1}{(1+j)^{q_v-1}-1}\,. \tag{2.70}$$

where $T_v(1)$ is the initial visiting temperature. Note that for $(q_v, q_a) = (1, 1)$ the GSA reduces to the CSA and for $(q_v, q_a) = (2, 1)$ it becomes the FSA. A comparison of the CSA, FSA and GSA by Xiang and Gong [48] shows that the performance of the GSA is significantly higher due to the visiting distribution allowing the wide search space to be sampled more quickly, leading to faster convergence.

For the cost function investigated in Ref. [59] it was found that optimum convergence occured for $T_v = T_a$, $q_a = 1$ and $q_v = 2.5$, where the variation of q_v most affected the rate of convergence for this particular cost function. These numbers are in agreement with the GSA algorithm implemented later in Chapter 7.

References

[1] A. M. Weiner, "Femtosecond pulse shaping using spatial light modulators," *Rev. Sci. Instrum.* **71**(5), pp. 1929–1960, 2000.

[2] J. M. Dela Cruz, I. Pastirk, M. Comstock, V. V. Lozovoy, and M. Dantus, "Use of coherent control methods through scattering biological tissue to achieve functional imaging," *PNAS* **101**(49), pp. 16996–17001, 2004.

[3] M. C. Chen, J. Y. Huang, and L. J. Chen, "Coherent control multiphoton processes in semiconductor saturable bragg reflector with freezing phase algorithm," *Appl. Phys. B* **80**(3), pp. 333–340, 2005.

[4] J. M. Dela Cruz, I. Pastirk, V. V. Lozovoy, K. A. Walowicz, and M. Dantus, "Multiphoton intrapulse interference 3: Probing microscopic chemical environments," *J. Phys. Chem. A.* **108**, pp. 53–58, 2004.

[5] N. Dudovich, D. Oron, and Y. Silberberg, "Single-pulse coherently controlled nonlinear Raman spectroscopy and microscopy," *Nature* **418**(6897), pp. 512–514, 2002.

[6] N. Dudovich, D. Oron, and Y. Silberberg, "Single-pulse coherent anti-Stokes Raman spectroscopy in the fingerprint spectral region," *J.Chem.Phys.* **118**(20), pp. 9208–9215, 2003.

[7] S. Shen and A. M. Weiner, "Complete dispersion compensation for 400-fs pulse transmission over 10-km fiber link using dispersion compensating fiber and spectral phase equalizer," *Photonics Technology Letters, IEEE* **11**(7), pp. 827–829, 1999.

[8] C. Cheng-Chun and A. M. Weiner, "Fiber transmission for sub-500-fs pulses using a dispersion-compensating fiber," *IEEE J. Quantum Electron.* **33**(9), pp. 1455–1464, 1997.

[9] S. H. Lee, A. L. Cavalieri, D. M. Fritz, M. Myaing, and D. A. Reis, "Adaptive dispersion compensation for remote fiber delivery of near-infrared femtosecond pulses," *Opt. Lett.* **29**(22), pp. 2602–2604, 2004.

[10] H. P. Sardesai, C. C. Chang, and A. M. Weiner, "A femtosecond code-division multiple-access communication system test bed," *Journal of Lightwave Technology* **16**(11), pp. 1953–1964, 1998.

[11] A. Efimov, M. D. Moores, B. Mei, J. L. Krause, C. W. Siders, and D. H. Reitze, "Minimization of dispersion in an ultrafast chirped pulse amplifier using adaptive learning," *Appl. Phys. B* **70**(7), pp. S133–S141, 2000.

[12] A. Efimov and D. H. Reitze, "Programmable dispersion compensation and pulse shaping in a 26-fs chirped-pulse amplifier," *Opt. Lett.* **23**(20), pp. 1612–1614, 1998.

[13] F. Röser, D. Schimpf, O. Schmidt, B. Ortaç, K. Rademaker, J. Limpert, and A. Tünnermann, "90 W average power 100μJ energy femtosecond fiber chirped-pulse amplification system," *Opt. Lett.* **32**(15), pp. 2230–2232, 2007.

[14] D. N. Schimpf, J. Limpert, and A. Tünnermann, "Controlling the influence of SPM in fiber-based chirped-pulse amplification systems by using an actively shaped parabolic spectrum," *Opt. Express* **15**(25), pp. 16945–16953, 2007.

[15] F. He, H. S. S. Hung, J. H. V. Price, N. K. Daga, N. Naz, J. Prawiharjo, D. C. Hanna, D. P. Shepherd, D. J. Richardson, J. W. Dawson, C. W. Siders, and C. P. Barty, "High energy femtosecond fiber chirped pulse amplification system with adaptive phase control," *Opt. Express* **16**(8), pp. 5813–5821, 2008.

[16] C. Froehly, B. Colombeau, and M. Vampouille, "Shaping and analysis of picosecond light-pulses," *Progress in Optics* **20**, pp. 65–153, 1983.

[17] A. M. Weiner, "Femtosecond optical pulse shaping and processing," *Prog. Quantum Electron.* **19**(3), pp. 161–237, 1995.

[18] M. M. Wefers and K. A. Nelson, "Space-time profiles of shaped ultrafast optical waveforms," *IEEE J. Quantum Electron.* **32**(1), pp. 161–172, 1996.

[19] R. N. Thurston, J. P. Heritage, A. M. Weiner, and W. J. Tomlinson, "Analysis of picosecond pulse shape synthesis by spectral masking in a grating pulse compressor," *IEEE J. Quantum Electron.* **22**(5), pp. 682–696, 1986.

[20] C. E. Shannon, "Communication in the presence of noise," *Proceedings of the IEEE* **86**(2), pp. 447–457, 1998.

[21] G. Stobrawa, M. Hacker, T. Feurer, D. Zeidler, M. Motzkus, and F. Reichel, "A new high-resolution femtosecond pulse shaper," *Appl. Phys. B* **72**(5), pp. 627–630, 2001.

[22] D. Goswami, "Optical pulse shaping approaches to coherent control," *Physics Reports* **374**(6), pp. 385–481, 2003.

[23] F. Verluise, V. Laude, Z. Cheng, C. Spielmann, and P. Tournois, "Amplitude and phase control of ultrashort pulses by use of an acousto-optic programmable dispersive filter: pulse compression and shaping," *Opt. Lett.* **25**(8), pp. 575–577, 2000.

[24] R. W. Boyd, *Nonlinear Optics*, Academic Press, 2nd ed., 2000.

[25] S. Guha, "Focusing dependence of the efficiency of a singly resonant optical parametric oscillator," *Appl. Phys. B* **66**(6), pp. 663–675, 1998.

[26] J. E. Midwinter and J. Warner, "The effects of phase matching method and of uniaxial crystal symmetry on the polar distribution of second-order non-linear optical polarization," *British Journal of Applied Physics* (8), p. 1135, 1965.

[27] L. E. Myers, R. C. Eckardt, M. M. Fejer, R. L. Byer, W. R. Bosenberg, and J. W. Pierce, "Quasi-phase-matched optical parametric oscillators in bulk periodically poled $LiNbO_3$," *J. Opt. Soc. Am. B* **12**(11), p. 2102, 1995.

[28] M. A. Watson, M. V. O'Connor, P. S. Lloyd, D. P. Shepherd, D. C. Hanna, C. B. E. Gawith, L. Ming, P. G. R. Smith, and O. Balachninaite, "Extended operation of synchronously pumped optical parametric oscillators to longer idler wavelengths," *Opt. Lett.* **27**(23), pp. 2106–2108, 2002.

[29] M. A. Watson, M. V. O'Connor, D. P. Shepherd, and D. C. Hanna, "Synchronously pumped CdSe optical parametric oscillator in the 9-10 μm region," *Opt. Lett.* **28**(20), pp. 1957–1959, 2003.

[30] K. L. Vodopyanov, O. Levi, P. S. Kuo, T. J. Pinguet, J. S. Harris, M. M. Fejer, B. Gerard, L. Becouarn, and E. Lallier, "Optical parametric oscillator based on microstructured GaAs," in *Solid State Laser Technologies and Femtosecond Phenomena, Oct 25-27 2004*, *Proceedings of SPIE - The International Society for Optical Engineering* **5620**, pp. 63–69, 2004.

[31] M. Nakamura, M. Kotoh, H. Taniguchi, and K. Tadatomo, "Bulk periodically poled MgO-doped $LiNbO_3$ by external electric field application," *Japanese Journal of Applied Physics Part 2-Letters* **38**(5A), pp. L512–L514, 1999.

[32] J. C. Diels and W. Rudolph, *Ultrashort laser pulse phenomena*, Academic Press, 2nd ed.

[33] R. L. Byer, "Parametric oscillators and nonlinear materials," in *Nonlinear Optics*, P. G. Harper and B. S. Wherrett, eds., Academic Press, New York, 1977.

[34] M. A. Watson, *Agile tuning and long-wavelength tuning of synchronously pumped optical parametric oscillators.* PhD thesis, University of Southampton, 2003.

[35] G. Boyd and D. Kleinman, "Parametric interaction of focused gaussian light beams," *IEEE J. Quantum Electron.* **4**(5), pp. 353–353, 1968.

[36] S. Guha, F. J. Wu, and J. Falk, "The effects of focusing on parametric oscillation," *IEEE J. Quantum Electron.* **18**(5), pp. 907–912, 1982.

[37] M. J. McCarthy and D. C. Hanna, "All-solid-state synchronously pumped optical parametric oscillator," *J. Opt. Soc. Am. B* **10**(11), p. 2180, 1993.

[38] D. C. Hanna, M. V. O'Connor, M. A. Watson, and D. P. Shepherd, "Synchronously pumped optical parametric oscillator with diffraction-grating tuning," *J. Phys. D* **34**(16), pp. 2440–2454, 2001.

[39] D. Findlay and R. A. Clay, "The measurement of internal losses in 4-level lasers," *Physics Letters* **20**(3), pp. 277–278, 1966.

[40] G. Imeshev, M. M. Fejer, A. Galvanauskas, and D. Harter, "Pulse shaping by difference-frequency mixing with quasi-phase-matching gratings," *J. Opt. Soc. Am. B* **18**(4), pp. 534–539, 2001.

[41] J. Prawiharjo, *Frequency-resolved optical gating in periodically-poled lithium niobate waveguide devices*. PhD thesis, University of Southampton, 2005.

[42] H. S. Tan and W. S. Warren, "Mid infrared pulse shaping by optical parametric amplification and its application to optical free induction decay measurement," *Opt. Express* **11**(9), pp. 1021–1028, 2003.

[43] T. Witte, K. L. Kompa, and M. Motzkus, "Femtosecond pulse shaping in the mid infrared by difference-frequency mixing," *Applied Physics B: Lasers and Optics* **76**(4), pp. 467–471, 2003.

[44] H. S. Tan, E. Schreiber, and W. S. Warren, "High-resolution indirect pulse shaping by parametric transfer," *Opt. Lett.* **27**(6), pp. 439–441, 2002.

[45] S. Shimizu, Y. Nabekawa, M. Obara, and K. Midorikawa, "Spectral phase transfer for indirect phase control of sub-20-fs deep UV pulses," *Opt. Express* **13**(17), pp. 6345–6353, 2005.

[46] M. V. O'Connor, M. A. Watson, D. P. Shepherd, and D. C. Hanna, "Use of a birefringent filter for tuning a synchronously pumped optical parametric oscillator," *Appl. Phys. B* **79**(1), pp. 15–23, 2004.

[47] L. Ingber and B. Rosen, "Genetic algorithms and very fast simulated reannealing: A comparison," *Mathematical and Computer Modelling* **16**(11), pp. 87–100, 1992.

[48] D. B. Strasfeld, S.-H. Shim, and M. T. Zanni, "Controlling vibrational excitation with shaped Mid-IR pulses," *Phys. Rev. Lett.* **99**(3), pp. 038102–4, 2007.

[49] R. Storn and K. Price, "Differential evolution a simple and efficient heuristic for global optimization over continuous spaces," *Journal of Global Optimization* **11**(4), pp. 341–359, 1997.

[50] K. A. De Jong, *Evolutionary Computation: A Unified Approach*, MIT Press, 2006.

[51] G. Jones, "Genetic and evolutionary algorithms," in *Encyclopedia of Computational Chemistry*, John Wiley and Sons Ltd, 1998.

[52] H.-Y. Fan and J. Lampinen, "A trigonometric mutation operation to differential evolution," *Journal of Global Optimization* **27**(1), pp. 105–129, 2003.

[53] S. Kirkpatrick, C. D. Gelatt, and M. P. Vecchi, "Optimization by simulated annealing," *Science* **220**(4598), pp. 671–680, 1983.

[54] N. Metropolis, A. W. Rosenbluth, M. N. Rosenbluth, A. H. Teller, and E. Teller, "Equation of state calculations by fast computing machines," *J.Chem.Phys.* **21**(6), pp. 1087–1092, 1953.

[55] S. Geman and D. Geman, "Stochastic relaxation, Gibbs distributions, and the Bayesian restoration of images," *IEEE Transactions on Pattern Analysis and Machine Intelligence* **6**(6), pp. 721–741, 1984.

[56] H. Szu and R. Hartley, "Fast simulated annealing," *Physics Letters A* **122**(3-4), pp. 157–162, 1987.

[57] L. Ingber, "Very fast simulated re-annealing," *Mathematical and Computer Modelling* **12**(8), pp. 967–973, 1989.

[58] L. Ingber, "Simulated annealing: Practice versus theory," *Mathematical and Computer Modelling* **18**(11), pp. 29–57, 1993.

[59] C. Tsallis and D. A. Stariolo, "Generalized simulated annealing," *Physica A* **233**(1-2), pp. 395–406, 1996.

Chapter 3

Pulse diagnostics

3.1 Introduction

Measurement of ultrafast pulses becomes a challenge when the duration of the pulse is of the same order or shorter than the speed of the detecting instrument. During initial demonstrations of ultrashort sources in the 1960s, detection systems were orders of magnitude too slow for the pulses to be accurately measured using conventional linear techniques. Due to the rapidly growing interest in mode-locked lasers, new methods for pulse characterisation were required to support it. In 1966, Weber [1] proposed the now well established intensity autocorrelation (AC) technique that was based on a Michelson interferometer arrangement with nonlinear detection. With the incident beam split into two, the pulse can be characterised with its own replica at different delays. In such an interferometric configuration, the short length of the pulse is no longer a hindrance and conventional slow detectors may be used. Relying on a stable continuous train of pulses, the intensity AC technique is a quick and easy method of measuring widths of simple pulses. However, the resolution of the AC is ultimately limited by the pulse itself so any detail in the pulse intensity will be washed out. Moreover, the AC technique is unable to detect the presence of chirp without independent measurement of the pulse spectrum to infer the time-bandwidth product.

A method known as fringe resolved autocorrelation (FRAC) or interferometric autocorrelation, was developed by Diels et al. [2], extending the intensity AC technique such that the presence of chirp could be directly inferred from the measurement. The experimental arrangement used is the Michelson arrangement described above with a fast detector to resolve the second order interfering fringes of the pulse electric field. For intensity ACs, these fringes are usually averaged out with a slow detector or completely avoided with a non-collinear arrangement. The interfering fringes, however, provide additional information about the phase of the pulse, so from the shape of the FRAC trace, it is possible to infer more about the pulse than from an intensity AC. Reconstruction of the phase has been demonstrated with an iterative method to fit data from a FRAC, an intensity AC and the spectrum [3] for simple pulses where a moderate amount of prior knowledge of the phase is required to start the iterative procedure. A more self-sufficient procedure, developed by Diels et al. [2, 4], involved placing a highly dispersive material in one of the Michelson arms to impose a known dispersion. The resulting fringe resolved cross-correlation could then be analysed along with the original FRAC to retrieve the original pulse.

Over the last decade, a technique making simultaneous measurements of the pulse in the time and frequency domain has dominated the research literature on ultrashort pulse diagnostics. Inspired by the analogue of a musical score, the time-frequency domain approach was initially proposed in the 70s by Treacy [5]. Kane and Trebino later developed a similar technique which they named frequency-resolved optical gating (FROG) [6, 7] in 1993, which was made commercially available by 2001, and has since proved to be a simple, robust and popular method of pulse measurement. The FROG has many different arrangements, which are discussed in detail in Ref. [8], but in general the technique involves measuring spectra at different delays of an autocorrelation (or cross-correlation), building up a 2D intensity image of the pulse in time and frequency. The original pulse electric field can then be retrieved using an iterative algorithm to reconstruct the measured FROG trace with extremely high accuracy.

Another time-frequency domain approach is the sonogram technique which involves measuring cross-correlations of the pulse with a frequency gated version of itself for different

frequencies within the spectrum. Initially demonstrated by Chilla and Martinez [9] and then later developed by Reid [10, 11], the cross-correlation sonogram (CCS) produces intuitive traces from which one can immediately see how the instantaneous frequency changes with time. The experimental setup had the particular appeal that a simple photodiode or LED could be used as a two-photon absorption detector in place of the more expensive and narrower bandwidth nonlinear crystals [11] and pulse retrieval could be achieved using algorithms similar to those used in FROG techniques.

The FROG and sonogram methods are both based on auto- or cross-correlation type arrangements. A completely different approach, based on spectral interferometry, is called spectral phase interferometry for direct electric-field reconstruction (SPIDER) [12]. This involves upconversion between two pulse replicas that are temporally delayed and where one is spectrally sheared. The spectral intensity of the nonlinearly produced pulse is the interferogram from which the original pulse can be extracted analytically without the need for an iterative algorithm.

For the work in this thesis, pulse characterisation of experimental pulses was carried out using the FRAC, sonogram and FROG techniques. Details of the theory behind these methods will be discussed further in Section 3.2. For the particular case of pulse characterisation at MIR wavelengths generated via a SPOPO, a comparison between the sonogram and cross-correlation FROG (XFROG) will be investigated in Section 3.3 with detailed experimental results and a discussion of the practical limitation of the two methods.

3.2 Ultrashort pulse measurement

The setups for measuring pulse characteristics in this thesis include the intensity autocorrelator (AC), fringe resolved autocorrelator (FRAC), frequency resolved optical gating (FROG), and the cross-correlation sonogram (CCS). The details of each of these methods are given in this section.

3.2.1 Autocorrelators

Figure 3.1 shows a schematic of a simple background-free autocorrelator that gives a measure of the pulse intensity (temporal) profile. The pulse is split into two at a beam-

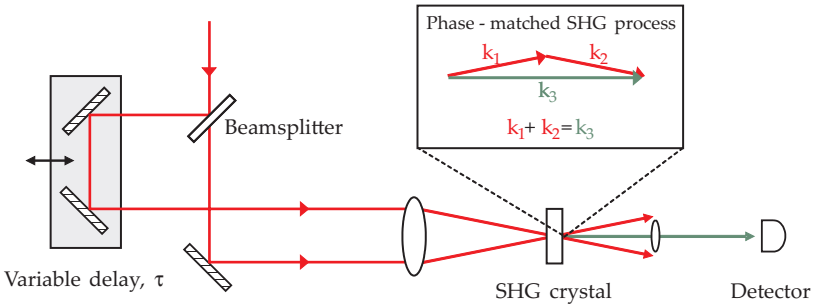

FIGURE 3.1: Experimental configuration for measurement of a background-free intensity autocorrelation.

splitter. One of the pulses picks up a delay relative to the other and the two pulses are then recombined at a SHG crystal. At this point the pulse is compared with itself at another time and the spatial overlap results in a SHG signal field given by,

$$E_{SHG}(t,\tau) \propto E(t)E(t-\tau), \tag{3.1}$$

and correspondingly, intensity is given by,

$$I_{SHG}(t,\tau) \propto I(t)I(t-\tau), \tag{3.2}$$

where E_{SHG} is the SHG electric field, I_{SHG} is the SHG intensity and τ is the delay.

The inset in Fig. 3.1 illustrates that a field contribution from both beams in a non-collinear arrangement results in a SHG field which exits the crystal at the angle bisector of the two fundamental beams to conserve wavevector $\mathbf{k}$ in a phase-matched process. The detected signal is therefore a background-free measurement.

The movable arm ensures that, each successive pulse can be delayed by a different amount resulting in a full intensity autocorrelation profile, $I_{AC}(\tau)$, represented by Eqn. 3.3,

$$I_{AC}(\tau) = \int_{-\infty}^{\infty} I(t)I(t-\tau)dt. \tag{3.3}$$

This equation is a simple overlap integral and shows that the autocorrelation maximum occurs at $\tau = 0$ where the two beams are perfectly overlapped. The resulting autocorrelation is also always symmetric so there is an ambiguity in the direction of time in this technique. As well as such trivial ambiguities, ACs also suffer from more serious ambiguity problems when attempting to reconstruct the original pulse intensity, I(t). This comes from the fact that ACs will wash out any fine detail in the original pulse so it is almost impossible to determine the pulse shape in terms of its intensity and phase without prior knowledge.

Despite the limited amount of information that can be derived from an AC, such a pulse measuring technique is extremely useful for simple unchirped single peak intensity profiles, and if prior knowledge of the pulse shape is assumed, one can accurately determine the pulse width of, for example, Gaussian or sech^2 pulses. The simplicity of the intensity AC technique is therefore valuable for such ultrashort pulse measurements.

As mentioned previously, the phase information of a pulse cannot be extracted from an intensity AC. However, the FRAC technique [2] can be used to determine the presence of chirp by simple interpretation of the FRAC profile. Figure 3.2 shows a Michelson interferometer setup for measuring this type of autocorrelation. The two beams are collinear in this case so it is no longer a background-free measurement. The non-linear

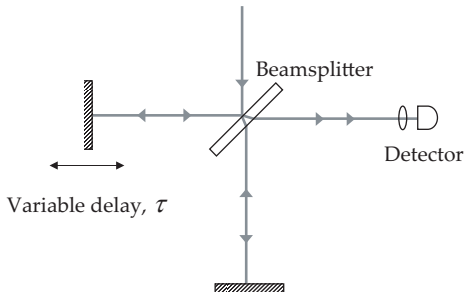

FIGURE 3.2: Two-photon absorption autocorrelator in a Michelson interferometer configuration.

optical process used here is two-photon absorption (TPA) and occurs within the photodiode (or LED) detector, although a SHG crystal, as with the previous AC setup, can be used. The detectors used in TPA autocorrelators can be standard commercially

available devices [13–17] and are therefore a cheap alternative to SHG crystals especially for measuring broadband sources where the crystal would have to be very thin to accommodate the bandwidth.

The interference of the two beams is recorded as a function of the variable delay, τ. Equation 3.4 describes the measured intensity, I_{FRAC}, with τ [2].

$$\begin{aligned} I_{FRAC}(\tau) &= \int_{-\infty}^{\infty} \left\{ I(t)^2 + I(t-\tau)^2 \right\} dt \\ &\quad +4 \int_{-\infty}^{\infty} \left\{ I(t) + I(t-\tau) \right\} Re \left\{ E(t) E^*(t-\tau) \right\} dt \\ &\quad +2 \int_{-\infty}^{\infty} Re \left\{ E(t)^2 E^*(t-\tau)^2 \right\} dt \\ &\quad +4 \int_{-\infty}^{\infty} I(t) I(t-\tau) dt. \end{aligned} \tag{3.4}$$

The first term in Eqn. 3.4 is the background measurement and therefore a constant. The second term is the interferogram of E(t) except for the $I(t)+I(t-\tau)$ term and the third term is the interferogram of the two-photon signal of E(t) resulting in the fringes of the IAC. Finally, the fourth term is the intensity autocorrelation as defined in Eqn. 3.3.

Intensity ACs can be taken with this type of setup by using a slow detector as the time averaged result of Eqn. 3.4 reduces to just the first and last term. Figures 3.3 (a) and (b) show an example of an AC (with background) and FRAC of a theoretical bandwidth-limited femtosecond pulse. For all FRACs, the contrast ratio of the peak to the background level is 8:1 and the contrast ratio for intensity ACs is 3:1. Chirp is observed as a narrowing of the two-photon interferogram component, exposing the shoulders of the intensity AC as shown in Eqn. 3.3(c) in which the theoretical pulse now has linear chirp.

The design, build and development of MIR measurement devices was a significant part in the acquisition of the key results in this thesis. The initial work involved building a TPA autocorrelator similar to the collinear arrangement depicted in Fig. 3.2 but the variable delay arm has a corner cube reflector mounted to a loudspeaker. A silicon wafer was used as a Fresnel reflection 70:25 beamsplitter and the output was focused with a 12.7mm CaF_2 lens on to an extended InGaAs detector. This detector had a TPA

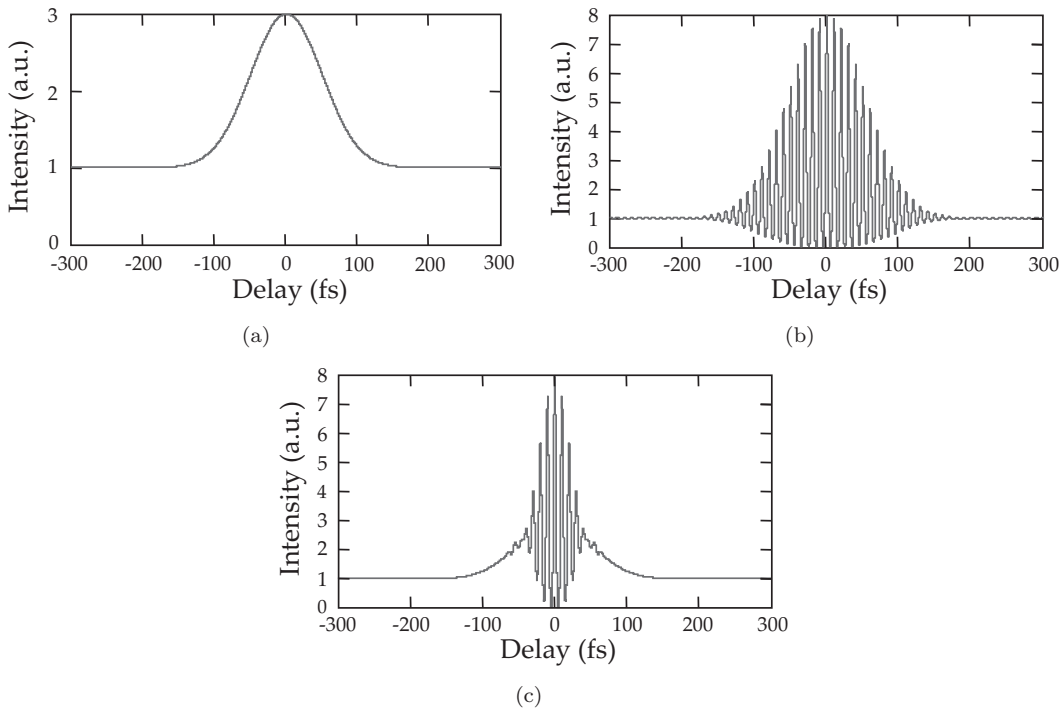

FIGURE 3.3: Theoretical autocorrelation functions for a 83fs bandwidth-limited pulse showing the contrast ratios for, (a) the intensity AC; (b) fringe resolved AC; and (c) a chirped 83fs pulse which has fewer fringes, revealing the intensity autocorrelation component at the wings.

wavelength range of 2.1-4.2 μm, which was suitable for the $\sim$3 μm source. The MIR source was a PPLN SPOPO which was pumped with a train of near-bandwidth-limited pulses at λ_p=1.047 μm, τ_p $\sim$4 ps and a repetition rate of 120MHz. Fringe resolved autocorrelation traces of the 3.2 μm idler output are shown in Fig. 3.4 for a chirped and unchirped pulse showing a good contrast ratio of 8:1 and symmetric autocorrelation profiles demonstrating accurate alignment and stability of the arrangement. Since the pulse width here is much longer than the theoretical pulse from Fig. 3.3, there are significantly more fringes within the FRAC envelope and are therefore indistinguishable. Note that the patterning effect on these measured FRAC traces is due to the sampling rate of the oscilloscope. The inset to Fig. 3.4(a) shows the individual fringes of the FRAC on a smaller timescale between $\pm$0.05 ps. The fringe spacing of $\sim$11 fs corresponds to the idler centre wavelength.

The chirped pulse in Fig. 3.4(b) was achieved by a small positive cavity length adjustment of the OPO to induce pulse compression of the signal and idler pulses. This is a well documented effect [18, 19] and is due to the group velocity mismatch between the pump

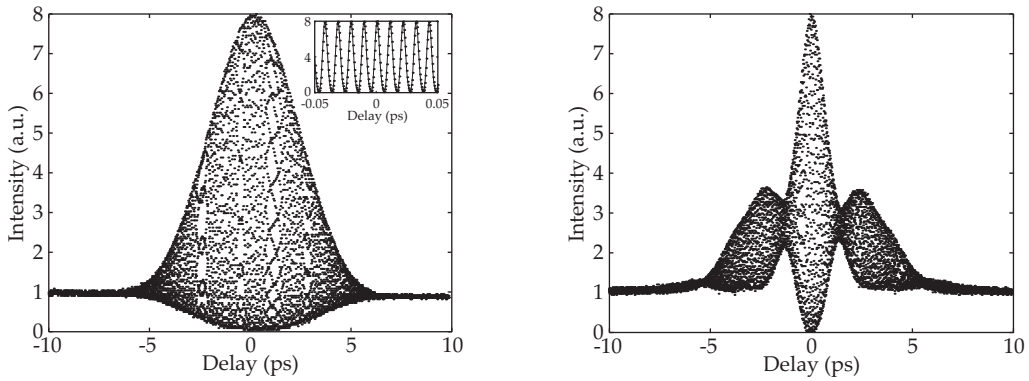

(a) (b)

FIGURE 3.4: Experimental FRAC showing, (a) an unchirped and (b) a chirped, MIR pulse, where the dots correspond to data points. The inset shows the FRAC trace in more detail between ± 0.05 ps to show the individual fringes that make up the trace.

and signal fields. By delaying the synchronism the signal walks through the pump and the leading edge of the signal pulse experiences high gain, strongly depleting the pump such that the resulting signal pulse is much shorter than the pump.

Measurement of the TPA response of various commercial photodetectors and LEDs was carried out by Reid and Sibbett [13] for use in autocorrelators, quantifying performance by the nonlinear response, R_{NL},

$$R_{NL} = \frac{I_{TPA}}{P_{pk} P_{av}} , \tag{3.5}$$

where R_{NL} has units of nA/(mW)^2, I_{TPA} is the photocurrent in nA, and P_{pk} and P_{av} are the peak power and average power, respectively. The sensitivity, S, has the units mW^2 is a measure of the minimum detectable signal and is given by,

$$S = (P_{pk} P_{av})_{min} . \tag{3.6}$$

Typical values for autocorrelator sensitivity for commercial devices are 1-10 mW^2. The TPA detectors investigated by Reid and Sibbett demonstrated comparable performance, and most notably, they achieved a sensitivity of $\sim 0.15 \times 10^{-3}$ mW^2 with the implementation of lock-in detection for an InGaAsP laser diode acting as a TPA detector. Based on the definition of Eqn. 3.5 the nonlinear response of the extended InGaAs detector used in this arrangement was measured to be 0.006 nA/(mW)^2 and with a detector sensitivity

of 84 mW^2, although this was later significantly improved after the implementation of lock-in detection.

Analysis by Diels et al. [2] found that the original electric field could be reconstructed for linearly chirped Gaussian pulses (or other simple pulse shapes) by iterative data fits to the FRAC, intensity AC and spectral intensity. For characterisation of more complex pulses, however, we turn to time-frequency domain techniques.

3.2.2 Frequency Resolved Optical Gating

We have seen from the previous section that time domain techniques like the autocorrelator, give very little information about the structure of the pulse and requires additional measurements, namely the pulse spectrum, for retrieval of phase information. Since the time and spectral components of a pulse are not independent one could gain a 2D mapping of the pulse in time and frequency by combining the autocorrelator and spectrometer techniques into one device. Originally proposed by Treacey [5], this time-frequency picture is otherwise known as a *spectrogram* in which a gate function samples the pulse in time, measuring spectra for each time slice to build up a 2D image of how the pulse spectrum progresses in time. An expression for the spectrogram, $\Sigma_g^E(\omega,\tau)$ is given below,

$$\Sigma_g^E(\omega,\tau) = \left| \int_{-\infty}^{\infty} E(t) g(t-\tau) \exp(-i\omega t) dt \right|^2 , \tag{3.7}$$

where $E(t)$ is the time-domain electric field of the pulse, $g(t-\tau)$ is the variable-delay gate function, τ is the time delay. A well-known device for measuring spectrograms is the FROG [6, 7] for which the gate function is related to $E(t)$ so the method is self-referencing, like the autocorrelator. We can rewrite Eqn. 3.7 to a more general form for the measured FROG trace, $I_{FROG}(\omega,\tau)$.

$$I_{FROG}(\omega,\tau) = \left| \int_{-\infty}^{\infty} E_{sig}(t) \exp(-i\omega t) dt \right|^2 , \tag{3.8}$$

where $E_{sig}(t,\tau)$, in this particular case, is given by,

$$E_{sig}(t,\tau) = E(t)\, g(t-\tau). \tag{3.9}$$

The most simple experimental FROG arrangement is the same as a background free intensity autocorrelator (see Fig. 3.1) except that the linear detector is replaced by a spectrometer. This arrangement is known as SHG FROG and is shown in Eqn. 3.5. The spectrometer measures the spectrum of the SHG autocorrelation signal for each increment of the delay τ. The result is a spectrogram, or FROG trace, mapping out frequency vs. delay, from which one can retrieve the spectral phase and intensity profiles.

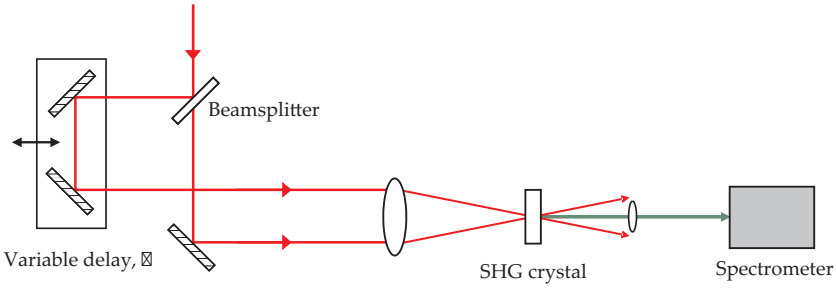

FIGURE 3.5: Schematic of the SHG FROG set-up [8].

The SHG FROG is one of the most popular geometries due to its sensitivity and simplicity. However, there are several limitations such as an ambiguity to the direction of time due to the symmetry of the trace and also the observation of the trace does not give an intuitive interpretation of the pulse. Other more intuitive FROG traces can be achieved with third order nonlinear arrangements such as PG (polarization gate) FROG and SD (self diffracting) FROG [6].

Having measured the FROG trace, it is then desirable to determine the electric field by solving what is known as the two-dimensional phase-retrieval problem [7] which yields an essentially unique solution for $E(t)$. In order to achieve this, we must first rewrite Eqn. 3.8 to a two-dimensional form.

$$I_{FROG}(\omega,\tau) = \left| \int_{-\infty}^{\infty} \int_{-\infty}^{\infty} \widetilde{E}_{sig}(t,\Omega) \exp(-i\omega t - i\Omega\tau)\, dt\, d\Omega \right|^2 , \tag{3.10}$$

where $\widetilde{E}_{sig}(t,\Omega)$ is the Fourier transform, with respect to τ, of $E_{sig}(t,\tau)$. Equation 3.10 can now be solved according to the two-dimensional phase retrieval problem to find $\widetilde{E}_{sig}(t,\Omega)$ from which $E(t)$ can be easily derived. The mathematical form of $E_{sig}(t,\tau)$ places an added constraint on the retrieval problem such that a unique solution might

be found and depends on the FROG geometry, for example [8],

$$E_{sig}(t,\tau) = \begin{cases} E(t)\,|E(t-\tau)|^2 & \text{for PG FROG} \\ E(t)^2 E^*(t-\tau) & \text{for SD FROG} \\ E(t)E(t-\tau) & \text{for SHG FROG} \end{cases} . \tag{3.11}$$

When dealing with pulse retrieval, the Fast Fourier transform (FFT) is a convenient way of switching between the time and frequency domains is required. Due to the use of FFT in FROG algorithms, the data must initially be interpolated to a N×N grid, known as the Fourier grid. This effectively couples the time and frequency domains and so it is important to ensure that the data is sufficiently sampled in both axes.

The most basic FROG retrieval algorithm uses the following procedure [8],

1. Begin with an initial guess for $E(t)$.
2. Generate the signal field $E_{sig}(t,\tau)$ and perform a Fourier transform for $\widetilde{E}_{sig}(t,\Omega)$.
3. Use the measured FROG data, $I_{FROG}(\omega,\tau)$, to generate a new guess for the signal field, $\widetilde{E}^k_{sig}(t,\Omega)$, for the kth iteration,

$$\widetilde{E}^k_{sig}(t,\Omega) = \frac{\widetilde{E}_{sig}(t,\Omega)}{\left|\widetilde{E}_{sig}(t,\Omega)\right|}\sqrt{I_{FROG}(\omega,\tau).} \tag{3.12}$$

4. Perform an inverse Fourier transform for $E^k_{sig}(t,\tau)$.
5. Generate a new guess for the field $E^{k+1}(t)$ using $E^k_{sig}(t,\tau)$ according to,

$$E^{k+1}(t) = \int_{-\infty}^{\infty} E^k_{sig}(t,\tau)\,d\tau\,. \tag{3.13}$$

6. Iterate steps 2 to 6 until convergence.

This algorithm is otherwise known as the iterative Fourier transform algorithm [20] and is quick and simple to implement. Convergence is usually measured by calculating what is known as the root mean square (RMS) error or FROG error, $G^{(k)}$ for each iteration

k, and is defined as [8],

$$G^{(k)} = \sqrt{\frac{1}{N^2}\sum_{m,n=1}^{N}\left|I_{FROG}(\omega_m,\tau_m) - \mu I^{(k)}_{FROG}(\omega_m,\tau_n)\right|^2}, \tag{3.14}$$

where $I_{FROG}(\omega_m,\tau_m)$ is the measured FROG data, $I^{(k)}_{FROG}(\omega_m,\tau_n)$ is the reconstructed FROG from the retrieved pulse and μ is the normalisation constant.

However, the algorithm does not always converge, particularly in the presence of noise or for complex pulse intensities. A more reliable and faster type of algorithm is based on a concept known as generalized-projections (GP) which involves making *projections* or guesses for $E_{sig}(t,\tau)$ that satisfy either Eqn. 3.11 or Eqn. 3.8 on each iteration until eventually both constraints are satisfied. Satifying Eqn. 3.8 can be achieved simply by replacing the magnitude of the current guess with the measured trace, as in Eqn. 3.12 from the iterative Fourier transform algorithm. Conforming to Eqn. 3.11, however, requires a minimization procedure to limit the functional distance between the previous guess calculated from $I_{FROG}(\omega,\tau)$ and the new guess calculated from Eqn. 3.12. Although the GP procedure is faster than the basic FROG algorithm, the convergence is still slow when compared to an even faster method, that does not require this minimization step, called principal component generalized projections (PCGP) [21]. In order to fully appreciate the elegance of the PCGP method, we first introduce another FROG geometry before outlining the main principles of the algorithm.

For more complex pulses, one can use the cross-correlation FROG (XFROG) [22] which measures the SFG or DFG interaction between two different pulses in contrast to the autocorrelation based methods like the SHG FROG. In its simplest case, one of the beams is a signal pulse to be measured and the other is a known reference, but it is also possible to retrieve the original fields of two unknown pulses by solving what is known as the two-dimensional blind deconvolution [23, 24]. This is known as blind-FROG and uses essentially the same geometry as the XFROG. Initial algorithms for the blind-FROG use the previously mentioned GP method which works reliably provided that the measured pulse spectra of the individual pulses are used as added constraints to the algorithm [24]. However, application of the PCGP method results in much faster

convergence as well as no longer requiring the spectral constraints to be essential to the problem [25]. Releasing these constraints means that the PCGP algorithm can be used, with minor modifications, as a general FROG algorithm for many other geometries.

The PCGP approach treats the GP step as an eigenvalue problem. The two unknown pulses, which we will refer to as the probe and gate, E(t) and G(t), are treated as vectors of length N. Each pulse is sampled for N points at different points in time with equal separation. Reconstruction of the FROG trace begins with the outer product matrix, O, of vectors E and G [8, Chap. 21]. O is then a N×N matrix of the pulse and gate interacting with each other at all discrete delay times and therefore contains all the sampling points necessary to reconstruct the FROG trace. This is easily achieved by shifting each row to the left by the row number minus one such that each column of the outer product represents interactions between the probe and gate pulses, $E(t)G(t-\tau)$, for a constant time delay, τ, at all discrete times and the rows are constant in time, t, at all discrete delays. Applying this transformation results in the time domain FROG trace and Fourier transforming each column generates the FROG trace. The next step of the algorithm requires the intensity constraint in Eqn. 3.12 to be applied and then, following an inversion of the FROG construction from E and G, a pseudo-outer product matrix is revealed. This matrix is unlikely to have a unique solution of E and G therefore is not strictly an outer product matrix hence the term *pseudo* is used. It can now be thought of as a superposition of many E and G combinations and with a vector describing weights of each pulse pair. The aim here is to extract the *principal component* of the superposition, i.e. the pulse pair with the largest weight, which is achieved with a reduced form of a mathematical method known as singular value decomposition (SVD) [26, Chap. 7]. This requires only a few iterations to extract the principle pair and hence the next guess of the FROG algorithm.

3.2.3 Sonogram

The sonogram technique [10] is a method of pulse characterisation that relies on frequency gating rather than temporal gating, which is used in FROG techniques. The

standard form for the sonogram is given by the following equation [27],

$$I_{sono}(t,\Omega) = \left| \int_{-\infty}^{\infty} \widetilde{E}(\omega)\widetilde{G}(\omega-\Omega)\exp(-i\omega t)d\omega \right|^2, \tag{3.15}$$

where $\widetilde{E}(\omega)$ describes the original pulse, $\widetilde{G}(\omega-\Omega)$ describes the frequency filter, and Ω is the frequency detuning.

Figure 3.6 shows the setup for a sonogram based on the TPA interferometric autocorrelator described in the previous section. This configuration involves frequency gating using

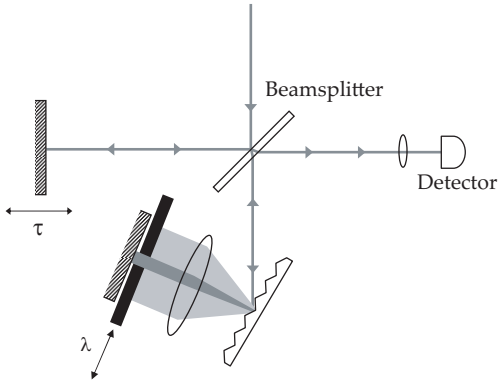

FIGURE 3.6: Schematic of the sonogram setup.

a diffraction grating and a movable mask in a folded 4-f pulse shaper arrangement such that, for each frequency, a cross-correlation is measured and compiled to retrieve similar information to the FROG trace. The resulting sonogram traces are highly intuitive and have no ambiguity in the direction of time so that one can distinguish between positive and negative chirp. Moreover, the sonogram setup can be easily modified for use in different wavelength regions as it only requires the detector to be changed, whereas the SHG FROG requires replacement of the relatively expensive SHG crystal. In this cross-correlation sonogram (CCS) arrangement, Eqn. 3.15 describes only the spectral filtering part of the measurement process. Due to the self-referencing nature of this method, the CCS measures a modified sonogram that can be accurately described by an intensity cross-correlation between the filtered replica and the original pulse intensity [27, 28],

$$I_{xsono}(t,\Omega) = I(t) \otimes I_{sono}(t,\Omega), \tag{3.16}$$

where I(t) is the intensity profile of the input pulse and $\otimes$ is the convolution operator. $I(t)$ can be approximated to a delta function such that $I_{xsono}(t,\Omega) \simeq I_{sono}(t,\Omega)$ for narrow slit widths where the filtered pulse width is temporally much longer than the original pulse, which should ideally be single-peaked. Pulses that are highly chirped cannot satisfy this approximation, in which case retrieval of the pulse requires an initial deconvolution step.

The CCS algorithm developed by Reid [10, 27] is based on the PCGP method used for FROG [21] described earlier in Section 3.2.2. Reconstruction of the sonogram from the two guess pulse vectors uses the same procedure as the FROG but it is in the frequency domain rather than the time domain. Retrieval of the CCS trace has an added step to deconvolve it with the intensity profile from the most recent guess to reveal the true sonogram. The intensity of the true sonogram would then replace the intensity of the current guess of the sonogram before applying the PCGP step to the pseudo-outer product matrix. As a result of the deconvolution step, the CCS algorithm can become unstable and introduce more noise although this can be suppressed by windowing the trace to enforce the finite support condition, i.e. that the trace shows a pulse in a "sea" of zeros, that is required for two-dimensional phase-retrieval problems. If the final retrieved trace does not agree well with measured spectra and autocorrelations, further constraints, such as zero phase on the gate pulse or the measured spectral phase, can be added.

3.3 Experimental comparison of the sonogram and cross-correlation FROG

Laser sources at the MIR wavelength regime have been a growing area of interest for applications in biochemistry. In particular, the development of parametric devices such as OPAs and OPOs for shaped ultrashort pulses in this regime has generated much interest in the area of coherent control. Excitation of the vibrational modes of common organic bonds falls within a wavelength range of 2-20 μm and successful manipulation of

such modes requires the use of ultrafast pulses to ensure that the processes occur within the timescales of the vibrational energy redistribution.

Characterising pulses in the MIR is more difficult than for the visible or NIR regions because commercially available devices like the SHG FROG are not available at these wavelengths. Moreover, off-the-shelf optics such as detectors and nonlinear crystals tend to cater better for the NIR, and in general, MIR devices are more expensive. Previous MIR pulse characterisation techniques have favoured SFG or DFG processes for XFROG [29, 30] although SHG FROG in the 3-5μm range using $AgGaS_2$ [31] has been demonstrated. In addition, the CCS technique developed by Reid et al. [10] is also a reliable method.

In this section, the XFROG and CCS techniques are compared for the measurement of ultrashort MIR pulses. The sensitivity of each method is experimentally determined and the intuitive nature of the spectrogram traces is considered. The practical limitations of each technique in terms of the acquisition process as well as the retrieval algorithms are discussed. The Matlab code used to acquire and retrieve the data was written by Jerry Prawiharjo.

3.3.1 Experimental setups

The MIR source ($\lambda_i = 3440\,\text{nm}$) is a PPLN SPOPO pumped with a train of pulses at $\lambda_p = 1047\,\text{nm}$, $\tau_p \sim 4\,\text{ps}$ and a repetition rate of 120 MHz. The temporally Gaussian pump pulses are coupled into an optical fibre through which they become chirped with a self-phase modulation (SPM) phase profile corresponding to a maximum phase shift of $\sim 10\,\text{rad}$ and a spectral broadening to 3.5 nm (958 GHz).

Independent measurements of the spectral intensity were acquired using a Czerny Turner monochromator (Bentham M300) with a nitrogen-cooled InSb detector. The intensity autocorrelations were measured using the CCS arrangement with no spectral filtering.

3.3.1.1 Cross-Correlation Sonogram

The experimental arrangement for the CCS is shown in Fig. 3.7. The input beam enters the sonogram setup and is split with a 50/50 pellicle beamsplitter. This type of beamsplitter allows for a more efficient Michelson arrangement than the FRAC setup described earlier in Section 3.2.1 where a silicon wafer was used as a 70:25 beamsplitter. The pellicle beamsplitter is made of a 2 μm thick nitrocellulose membrane which has minimal dispersion and no ghosting from multiple reflections.

One replica of the beam was incident on a grating and lens to result in frequency to space mapping at the FP where a variable slit was placed for spectral filtering before retro-reflecting the beam back. The other arm imposed a variable temporal delay so that cross-correlations of the input pulse with a frequency gated version of the pulse could be measured. The nonlinear process used was TPA, for which an extended InGaAs detector was used. Due to the collinearity of the experimental setup, interferometric cross-correlations were measured but the implementation of lock-in detection allowed for the interferometric frequencies to be filtered out as well as significantly increasing the sensitivity of the sonogram. A full sonogram trace comprised of 80 intensity cross-correlations, each at a different frequency, was acquired in less than 7 minutes.

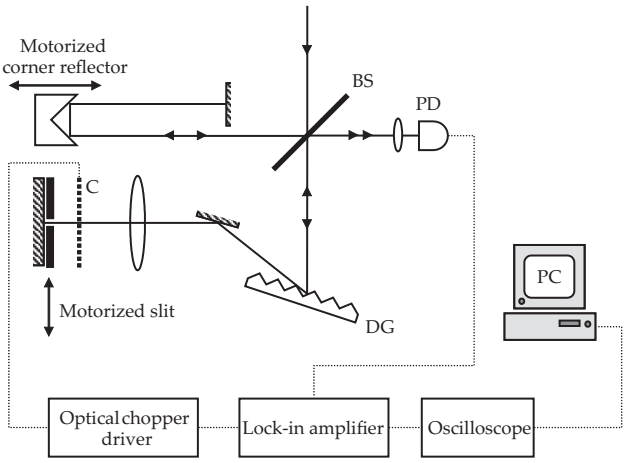

FIGURE 3.7: Schematic of experimental CCS arrangement. BS = beam splitter; PD = photodiode, C = chopper; DG = diffraction grating.

Adjustment of the resolution of the CCS arrangement could be controlled by the slit width of the spectral gating arm. Narrowing the slit corresponded to higher spectral

resolution but resulted in a temporally broadened gate pulse so care was taken to ensure that the motorized stage of the temporal delay arm had enough travel to measure the entire cross-correlation.

Calibration of the temporal domain depended on the speed of the motorized corner reflector and the frequency calibration was calculated using the grating equation for the frequency to space mapping at the FP. For this particular setup, the frequency to space mapping was 10nm/mm and the slit width was 0.4 mm corresponding to ∼1/10th of the total bandwidth.

A retrieval algorithm, as described in Section 3.2.3 was used following noise filtering of the data and interpolation to a Fourier grid. Only the constraints of the measured trace intensity and the mathematical form of the sonogram were used. The quality of the retrieval was assessed by comparison of the retrieved data to measured spectral intensity and autocorrelation traces. The RMS error, which compares the measured and retrieved traces, is also a good measure of retrieval quality but can be misleading for traces with a low signal-to-noise ratio.

A typical CCS trace is shown in Fig. 3.8 with good signal to noise and good agreement of the measured and retrieved AC and spectral intensity. The RMS error was typically 0.01 for a 128×128 grid.

3.3.1.2 Cross-Correlation Frequency Resolved Optical Gating

A schematic of the XFROG setup is shown in Fig. 3.9. The idler and depleted pump beams exit the SPOPO both synchronously and collinearly, and so could be conveniently used in this interferometric arrangement. The pump beam was reflected by a CaF_2 mirror that was highly reflecting at the pump wavelength but transmissive at the idler wavelength. A telescope then resized the pump beam to a spot size of ∼2 mm before a temporal delay was imposed using two turning mirrors on a motorized stage. Meanwhile, the idler beam with a spot size of ∼3 mm travelled a fixed path, passing through a long wave pass (LWP) filter on the way, to filter out any residual wavelengths from the SPOPO, such as the SHG of the pump. The two beams were then recombined with

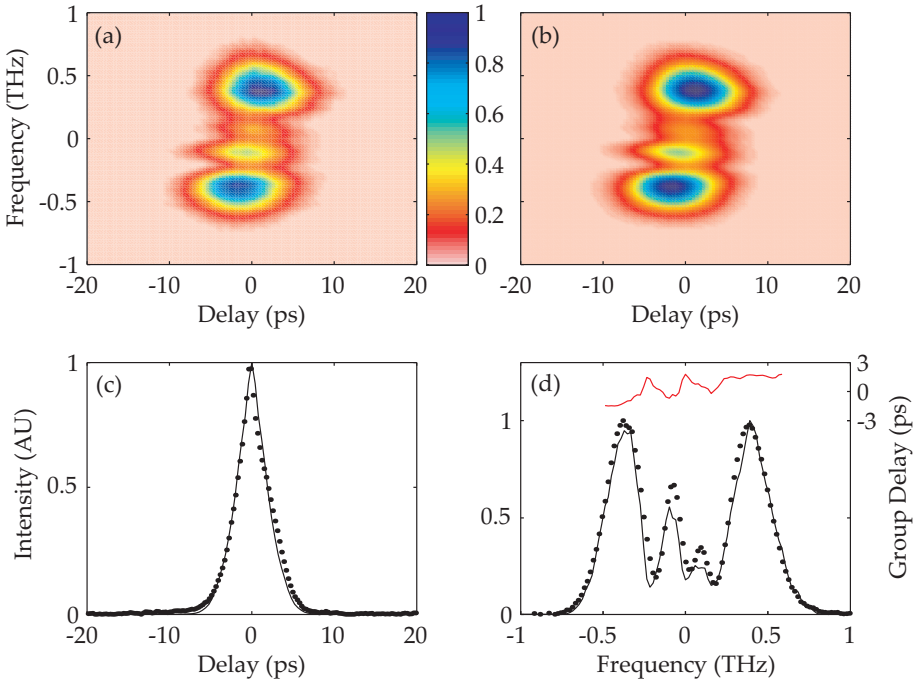

FIGURE 3.8: Typical MIR CCS trace of the (a) measured CCS, (b) retrieved CCS. The measured (circles) and retrieved (solid curve) (c) AC and (d) spectra of the idler are shown with the retrieved group delay (red solid curve).

another CaF_2 mirror/window before being focused with a 50 mm focal length CaF_2 lens into a 1 mm PPLN crystal to host the DFG process. The length of the crystal was chosen such that the effects due to dispersion were negligible. The spot sizes of the pump and idler were chosen carefully such that near confocal focusing could be achieved in the crystal. The grating period used in the PPLN was the same as that used in the SPOPO, generating a signal beam at $\lambda_s = 1505$ nm. Note that a major advantage of the XFROG is that spare PPLN crystals can be used as DFG crystals in this setup and that the output signal is at a wavelength that is regularly monitored in the lab so equipment is readily available. The signal was detected using a fibre-coupled optical spectrum analyser (OSA) (Ando AQ-6310C) that has a minimum resolution of 0.1 nm and a maximum sensitivity of -49 dBm. A spectrum was measured for each time-slice of the cross-correlation and a typical XFROG trace composed of 100 spectra was acquired in less than 3 minutes.

The retrieval algorithm used is the PCGP FROG algorithm, similar to the CCS algorithm but without the deconvolution step. Due to the complexity of the depleted pump and idler pulses, the measured idler spectrum was used as an initial guess to improve

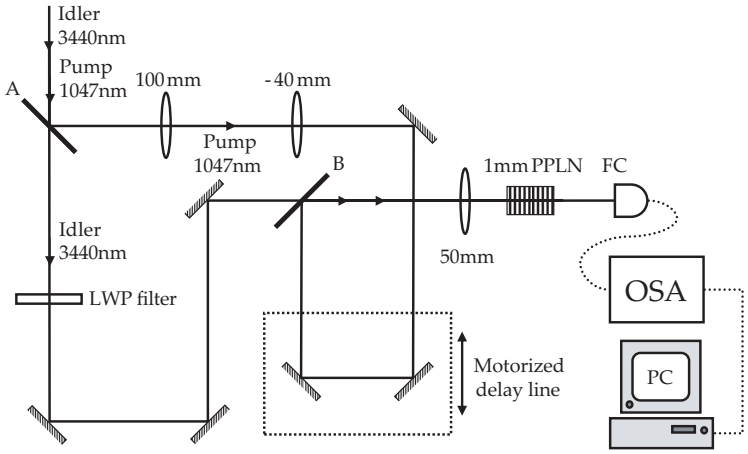

FIGURE 3.9: Schematic of experimental XFROG arrangement. A and B are CaF_2 mirrors that are highly reflecting at the pump wavelength and transmissive at the idler wavelength.

the convergence and hence conformation to the measured data. In contrast to the CCS, both the pump and idler pulses are retrieved and the quality of this retrieval is shown in Fig. 3.10, showing good agreement with the measured AC and spectral data. Although the interest was only in the idler pulse, the agreement between the measured and retrieved pump spectrum was always monitored to ensure a good fit. The RMS error was typically 0.005 for a 128×128 grid.

3.3.2 Results

The experimental results in this section examine the sensitivity of both pulse characterisation methods. The idler power was attenuated by discrete amounts using filters. For the CCS, the ND filters were placed before the the beam enters the system and for the XFROG setup, the ND filters were placed after the pump and idler beams had been separated at mirror A. The pump beam in the XFROG arrangement was also attenuated in this way.

For the CCS arrangement, retrievable traces could be still achieved with idler average powers between 13 and 18 mW. Figure 3.11 shows the measured and retrieved sonogram trace for an average power of 18 mW. The retrieved AC and spectrum is also shown for an average power of 13 mW showing a good fit to the measured AC trace and a fairly noisy but moderate fit to the spectral data.

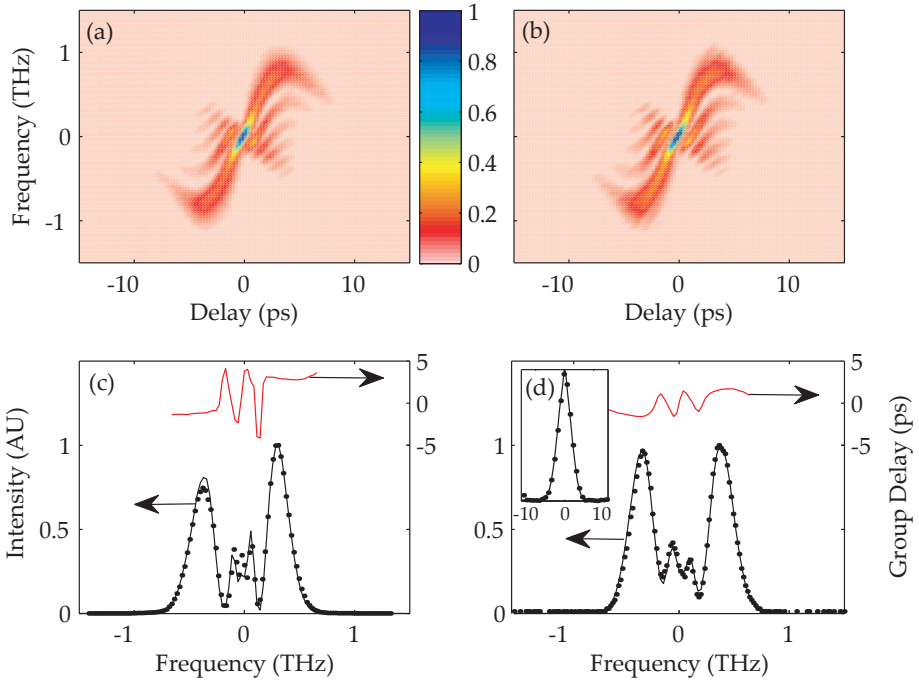

FIGURE 3.10: Typical MIR XFROG trace of the (a) measured XFROG, (b) retrieved XFROG. The measured (circles) and retrieved (solid curve) spectra of the pump, (c), and idler, (d), are shown with the retrieved group delay (red solid curve). The inset for (d) is the measured (circles) and retrieved (solid curve) AC of the idler pulse.

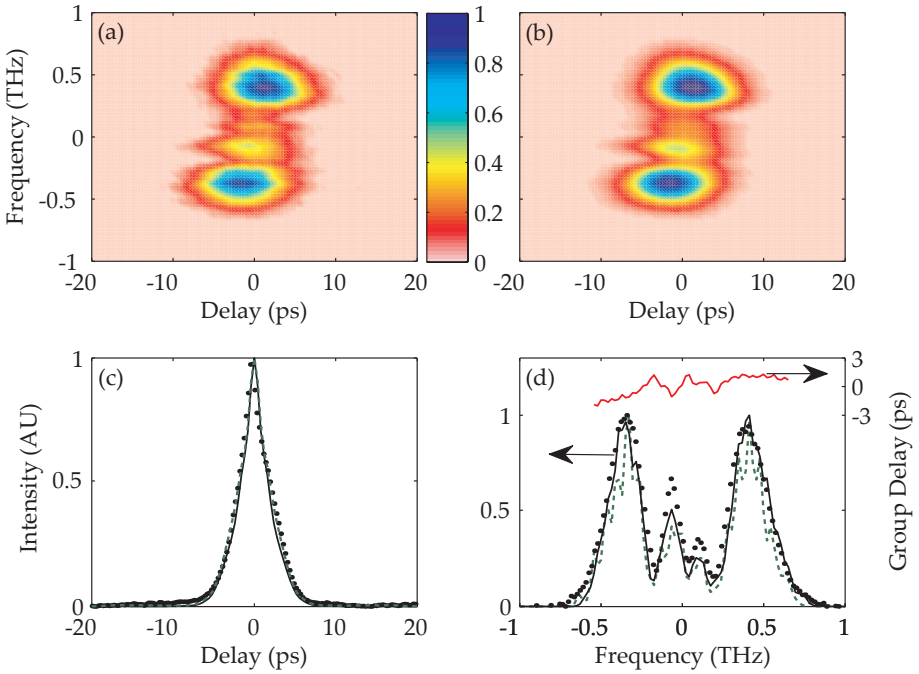

FIGURE 3.11: Low power limit MIR Sonogram trace of the (a) measured sonogram, (b) retrieved sonogram, (c) measured (circles) and retrieved (solid curve) autocorrelation traces and (d) measured (circles) and retrieved (solid curve) spectra with the retrieved group delay (red solid curve) all at an average power of 18 mW. Retrieved data at 13 mW is also shown (green dotted).

The sensitivity of the XFROG arrangement was measured first by keeping the pump power constant and reducing the idler power, and secondly, by reducing both the pump and idler average powers but keeping the ratio of the powers fairly constant. The SPOPO provided maximum powers of 115 and 70 mW for the pump and idler, respectively. Figure 3.12 shows that retrievable XFROG traces could comfortably be achieved with idler powers of 1.8 mW for 115 mW of pump power. XFROG traces measured with idler average powers as low as 1.0mW could also be retrieved with AC and spectrum showing fairly noisy but moderate agreement to the measured data.

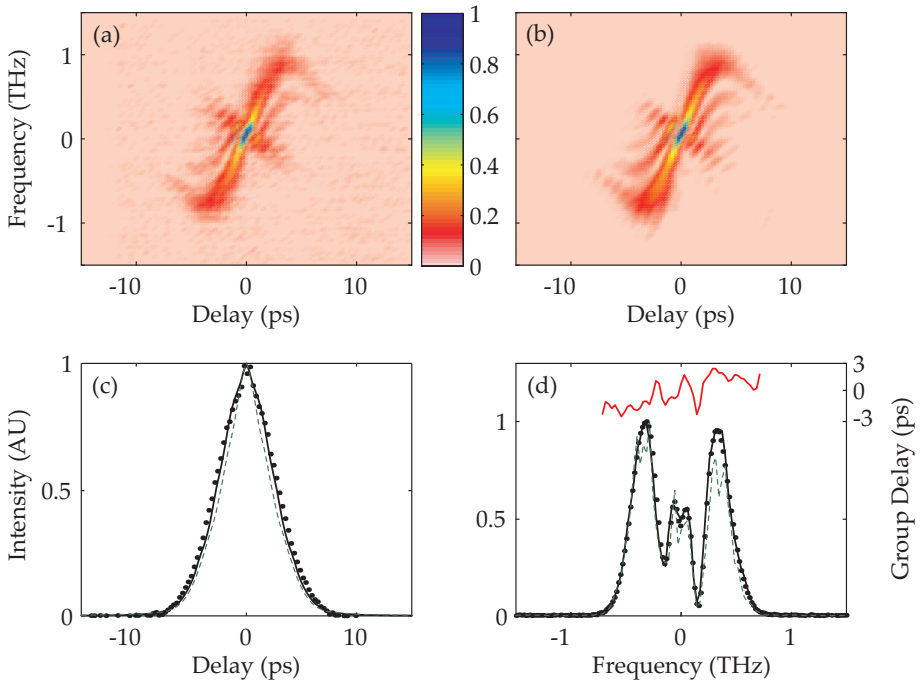

FIGURE 3.12: Low power limit MIR XFROG trace of the (a) measured XFROG, (b) retrieved XFROG, (c) measured (circles) and retrieved (solid curve) autocorrelation traces and (d) measured (circles) and retrieved (solid curve) spectra with the retrieved group delay (red solid curve) all at an average power of 1.8 mW. Retrieved data at 1.0 mW is also shown (green dotted).

In a separate experiment, the maximum available pump and idler powers were 163 and 47 mW, respectively. Maintaining this ratio of powers of 3.5:1, the pump and idler beams were attenuated measuring retrievable XFROG traces at an idler power of 3.1 mW as shown in Fig. 3.13. Measurements taken with ∼1 mW of idler power could not be retrieved at this pump/idler average power ratio.

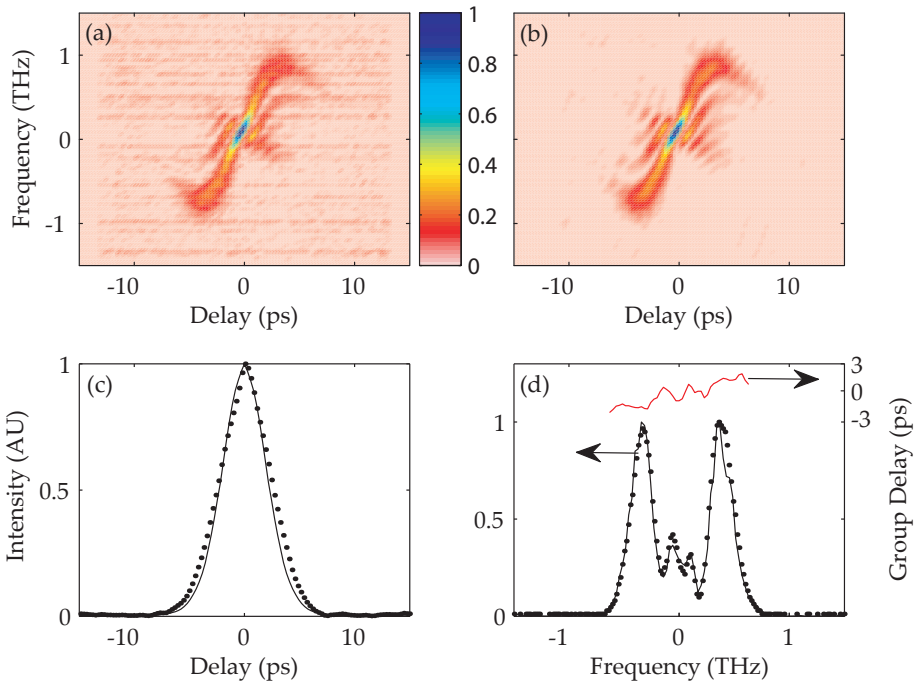

FIGURE 3.13: Low power limit MIR XFROG trace of the (a) measured XFROG, (b) retrieved XFROG, (c) measured (circles) and retrieved (solid curve) autocorrelation traces and (d) measured (circles) and retrieved (solid curve) spectra with the retrieved group delay (red solid curve) all at an average power of 10.5 mW and 3.1 mW for the pump and idler, respectively.

3.3.3 Discussion

The results comparing the sensitivity of the CCS and XFROG arrangement have shown that the XFROG is significantly more sensitive. Retrievable traces could be achieved at a minimum input power of 13mW for the CCS setup. However, the XFROG is capable of characterising pulses with only ~1 mW of idler power using 115 mW of pump power, and 3 mW for a pump/idler ratio of 3.5:1. The sensitivity of the XFROG and CCS, based on Eqn. 3.6 is calculated to be 2×10^3 and 3×10^5 mW^2, respectively. The lower sensitivity of the CCS is largely due to the significant loss induced by the spectrally filtering slit, which is approximately 1/10th of the total bandwidth in order to resolve the pulse, as well as the loss incurred by the diffraction grating. Moreover, the 50/50 beamsplitter introduces, theoretically, a loss of at least 50% such that the signal at the nonlinear detector was measured to be typically no more than 23% of the input power. In contrast, the losses induced in the XFROG setup are due to transmission through the CaF_2 mirrors, the LWP filter which introduces a 30% loss on the idler beam, focusing

into the PPLN crystal, which was not AR coated, and focusing into the fibre-coupled OSA.

As well as the losses in the systems, noise contributions also affect the overall sensitivity of the measurements. The CCS was particularly prone to mechanical noise from the time-delay motor and optical chopper whereas the XFROG setup had no mechanical movement when the data was acquired.

In terms of the practicalities of alignment, both systems required careful alignment procedures. It was important to ensure that the movement of the delay arm was parallel to the beam in both the horizontal and vertical axes to minimise beam movement at the point of detection. Both systems are also polarisation sensitive since the diffraction grating efficiency in the CCS arrangement favours s-polarization and parametric generation in PPLN favours polarisation parallel to the domains which, in this case, is also s-polarisation.

The size of the beams is also an important alignment issue for both setups. For the CCS, the size of the MIR beam determines the spectral resolution of the filter arm (see pulse shaping theory in Section 2.2.1) but one must also consider that the beam needs to fill the small focusing lens to the TPA detector to achieve a small spot size on the detector area. For the XFROG, the pump and idler beams should ideally have equal confocal lengths for confocal focusing at the nonlinear crystal to optimise the spatial overlap and the interaction length. However, care must be taken to avoid high intensities due to unwanted high order nonlinear effects that could distort the signal output pulse.

Wavelength tuning of the CCS was achieved by rotating the grating, keeping the difference between the incident angle and diffracted angle constant for a large range of centre wavelengths. The extended InGaAs detector has a large TPA wavelength range of 2.1 to 4.2 μm providing flexible tunability. The XFROG is wavelength tuned by translating the PPLN crystal to a grating that has a similar poling period than the one in the OPO setup. Temperature tuning can also be used if fine wavelength tuning is required.

Another advantage of the XFROG is the simplicity of the calibration. The spectral calibration is internal to the commercial OSA which should be accurately calibrated.

In contrast, for the CCS, the spectral calibration is calculated based on the grating incident angle which is prone to measurement errors. The temporal calibration in both cases simply related to the distance travelled and the speed of light, but in the case of the CCS, the calibration also depends on speed of the motor.

Once the spectrogram traces are acquired however, the CCS technique has the advantage that it creates highly intuitive traces. One can immediately identify the four distinct spectral peaks and the temporal position of those peaks gives a good indication of the instantaneous frequency of the pulse. In contrast, although the XFROG trace is, in this case, particularly reminiscent of the instantaneous frequency, one cannot get a sense of the spectral or temporal shape of the pulse. With few exceptions, FROG techniques generally do not yield immediately intuitive traces for complex pulses like the SPM pulse studied here. Early work by DeLong et al. investigated how to visually interpret PG, SD and SHG FROG traces [32] and identify the instantaneous frequency behaviour. However, issues like intuitiveness may not be of particular importance if the algorithm is fast and reliable.

Independent measurements of the spectral amplitude and autocorrelation are often required to verify the quality of the pulse retrieval. Both arrangements require the MIR spectral intensity to be measured in a separate setup using a monochromator, whereas for the intensity AC, the CCS arrangement can conveniently be used in an open slit arrangement to act as an autocorrelator. The XFROG, however, requires a separate apparatus for the intensity AC measurement.

Retrieval of the traces both use the PCGP algorithm described in previous sections. The CCS algorithm was generally less successful in retrieving the pulse accurately since the traces were more noisy that the XFROG traces, due to mechanical noise and low signal-to-noise. The success of the retrieval depended on the size of the filtering window and the accuracy of the frequency calibration factor. Accurate retrievals could be achieved, after several attempts at running the algorithm, by small variations in either of these factors. Retrieval of the XFROG traces however, were found to be reliably retrieved if the measured idler spectrum was used as an initial guess and if the trace had sufficient signal-to-noise. No data filtering or calibration factors were necessary.

Finally, both systems are fairly inexpensive, especially if equipment such as lock-in detection systems and an OSA are readily available in the lab. The advantage of the CCS nonlinear detection is that it uses cheap photodiodes rather than nonlinear crystals like PPLN, however, for this particular XFROG setup, the PPLN was from spare OPO crystals in the lab.

In conclusion both techniques can be achieved with fairly simple and inexpensive arrangements, however overall the XFROG method is a more robust technique than the CCS. The XFROG has no sources of mechanical noise, and significantly lower loss in the system, making it a more sensitive technique. With traces that are less noisy and prone to calibration errors, the retrieval is reliable provided that the measured idler spectrum is used as an added constraint.

Initial development of MIR pulse characterisation for this project began with the TPA autocorrelator arrangement and results with this system are shown later in Chapter 4. Since the CCS is a simple modification of the TPA autocorrelator arrangement, initial spectrogram measurements used this technique for which the results are shown in Chapter 6. Development of the XFROG arrangement described in this section occurred after this experiment. The design of the XFROG setup is particularly suited to MIR OPO measurements due to the collinearity and synchronism between the pump and idler outputs. In addition, there is a relatively large amount of pump power compared with the idler power which, as we have seen from the results here, is an advantage when characterising pulses with low idler average power. As a consequence of the results shown in this chapter, it is anticipated that future experiments will use the XFROG for MIR pulse characterisation.

References

[1] H. P. Weber, "Method for pulsewidth measurement of ultrashort light pulses generated by phase-locked lasers using nonlinear optics," *J. Appl. Phys.* **38**(5), pp. 2231–2234, 1967.

[2] J. C. M. Diels, J. J. Fontaine, I. C. McMichael, and F. Simoni, "Control and measurement of ultrashort pulse shapes (in amplitude and phase) with femtosecond accuracy," *Appl. Optics* **24**(9), pp. 1270–1282, 1985.

[3] K. Naganuma, K. Mogi, and H. Yamada, "Time direction determination of asymmetric ultrashort optical pulses from second-harmonic generation autocorrelation signals," *Appl. Phys. Lett.* **54**(13), pp. 1201–1202, 1989.

[4] C. Yan and J.-C. M. Diels, "Amplitude and phase recording of ultrashort pulses," *J. Opt. Soc. Am. B* **8**(6), p. 1259, 1991.

[5] E. B. Treacy, "Measurement and interpretation of dynamic spectrograms of picosecond light pulses," *J. Appl. Phys.* **42**(10), pp. 3848–3858, 1971.

[6] D. J. Kane and R. Trebino, "Characterization of arbitrary femtosecond pulses using frequency-resolved optical gating," *IEEE J. Quantum Electron.* **29**(2), pp. 571–579, 1993.

[7] R. Trebino and D. J. Kane, "Using phase retrieval to measure the intensity and phase of ultrashort pulses: frequency-resolved optical gating," *J. Opt. Soc. Am. A* **10**(5), p. 1101, 1993.

[8] R. Trebino, *Frequency-Resolved Optical Gating: The Measurement of Ultrashort Laser Pulses*, Klewer Academic Publishers, 2002.

[9] J. L. A. Chilla and O. E. Martinez, "Direct determination of the amplitude and the phase of femtosecond light-pulses," *Opt. Lett.* **16**(1), pp. 39–41, 1991.

[10] D. T. Reid, "Algorithm for complete and rapid retrieval of ultrashort pulse amplitude and phase from a sonogram," *IEEE J. Quantum Electron.* **35**(11), pp. 1584–1589, 1999.

[11] I. G. Cormack, W. Sibbett, and D. T. Reid, "Rapid measurement of ultrashort-pulse amplitude and phase from a two-photon absorption sonogram trace," *J. Opt. Soc. Am. B* **18**(9), pp. 1377–1382, 2001.

[12] C. Iaconis and I. A. Walmsley, "Spectral phase interferometry for direct electric-field reconstruction of ultrashort optical pulses," *Opt. Lett.* **23**(10), pp. 792–794, 1998.

[13] D. T. Reid, W. Sibbett, J. M. Dudley, L. P. Barry, B. Thomsen, and J. D. Harvey, "Commercial semiconductor devices for two photon absorption autocorrelation of ultrashort light pulses," *Appl. Optics* **37**(34), pp. 8142–8144, 1998.

[14] D. T. Reid, M. Padgett, C. McGowan, W. E. Sleat, and W. Sibbett, "Light-emitting diodes as measurement devices for femtosecond laser pulses," *Opt. Lett.* **22**(4), pp. 233–235, 1997.

[15] J. K. Ranka and A. L. Gaeta, "Autocorrelation measurement of 6-fs pulses based on the two-photon-induced photocurrent in a GaAsP photodiode," *Opt. Lett.* **22**(17), pp. 1344–1346, 1997.

[16] K. A. Briggman, L. J. Richter, and J. C. Stephenson, "Imaging and autocorrelation of ultrafast infrared laser pulses in the 3-11μm range with silicon ccd cameras and photodiodes," *Opt. Lett.* **26**(4), pp. 238–240, 2000.

[17] A. C. Millard, D. N. Fittinghoff, and J. A. Squier, "Using GaAsP photodiodes to characterise ultrashort pulses under high numerical aperture focusing in microscopy," *J. Microsc.* **193**(3), pp. 179–181, 1999.

[18] J. D. V. Khaydarov, J. H. Andrews, and K. D. Singer, "Pulse-compression in a synchronously pumped optical parametric oscillator from group-velocity mismatch," *Opt. Lett.* **19**(11), pp. 831–833, 1994.

[19] L. Lefort, K. Puech, S. D. Butterworth, Y. P. Svirko, and D. C. Hanna, "Generation of femtosecond pulses from order-of-magnitude pulse compression in a synchronously pumped optical parametric oscillator based on periodically poled lithium niobate," *Opt. Lett.* **24**(1), pp. 28–30, 1999.

[20] J. R. Fienup, "Phase retrieval algorithms: a comparison," *Appl. Opt.* **21**(15), p. 2758, 1982.

[21] D. J. Kane, "Real-time measurement of ultrashort laser pulses using principal component generalized projections," *Selected Topics in Quantum Electronics, IEEE Journal of* **4**(2), pp. 278–284, 1998.

[22] S. Linden, H. Giessen, and J. Kuhl, "XFROG - a new method for amplitude and phase characterization of weak ultrashort pulses," *Physica Status Solidi B-Basic Research* **206**(1), pp. 119–124, 1998.

[23] G. R. Ayers and J. C. Dainty, "Interative blind deconvolution method and its applications," *Opt. Lett.* **13**(7), p. 547, 1988.

[24] K. W. DeLong, R. Trebino, and W. E. White, "Simultaneous recovery of two ultrashort laser pulses from a single spectrogram," *J. Opt. Soc. Am. B* **12**(12), p. 2463, 1995.

[25] D. J. Kane, G. Rodriguez, A. J. Taylor, and T. S. Clement, "Simultaneous measurement of two ultrashort laser pulses from a single spectrogram in a single shot," *J. Opt. Soc. Am. B* **14**(4), pp. 935–943, 1997.

[26] D. C. Lay, *Linear algebra and its applications*, Addison Wesley, 3rd ed., 2006.

[27] D. T. Reid and J. Garduno-Mejia, "General ultrafast pulse measurement using the cross-correlation single-shot sonogram technique," *Opt. Lett.* **29**(6), pp. 644–646, 2004.

[28] V. Wong and I. A. Walmsley, "Ultrashort-pulse characterization from dynamic spectrograms by iterative phase retrieval," *J. Opt. Soc. Am. B* **14**(4), pp. 944–949, 1997.

[29] H. S. Tan and W. S. Warren, "Mid infrared pulse shaping by optical parametric amplification and its application to optical free induction decay measurement," *Opt. Express* **11**(9), pp. 1021–1028, 2003.

[30] S. Linden, J. Kuhl, and H. Giessen, "Amplitude and phase characterization of weak blue ultrashort pulses by downconversion," *Opt. Lett.* **24**(8), pp. 569–571, 1999.

[31] T. Witte, D. Zeidler, D. Proch, K. L. Kompa, and M. Motzkus, "Programmable amplitude- and phase-modulated femtosecond laser pulses in the mid-infrared," *Opt. Lett.* **27**(2), pp. 131–133, 2002.

[32] K. W. Delong, R. Trebinoi, and D. J. Kane, "Comparison of ultrashort-pulse frequency-resolved-optical-gating traces for 3 common beam geometries," *J. Opt. Soc. Am. B* **11**(9), pp. 1595–1608, 1994.

Chapter 4

Adaptive Control of Mid-infrared Pulses using an Optical Parametric Oscillator

4.1 Introduction

Pulse shaping of MIR sources has significant applications in coherent control of molecules through vibrational modes that are resonant in the MIR wavelength range. With the development of ultrashort sources in this wavelength region, as well as the advances in pulse shaping techniques, adaptive MIR pulse shaping is becoming a growing area of interest.

Recently, direct shaping of MIR pulses using a Ge AOM [1, 2] has been demonstrated with an OPA based system which has led to coherent control of vibrational excitations of a CO stretching mode using adaptive phase shaping [3]. However, in such an arrangement, wavelength tuning of the MIR beam would require adjustment of the very sensitive 4-f shaper alignment. Moreover, AOM shapers are limited to repetition rates of $\sim$1 MHz.

In general, pulse shaping optics such as LCMs and AOMs are commonly only transparent in the visible and NIR regions. As a result, an indirect approach is generally used by

initially shaping a pulse at the visible or NIR wavelengths before transferring the pulse shape to the MIR, through interaction with an unshaped pulse, using a single pass parametric process [4–9]. Several groups have considered high fidelity transfer of the pulse shape by using a narrow bandwidth pulse for the unshaped field [7–9].

In this chapter indirect pulse shaping of MIR pulses from a SPOPO is demonstrated [10], in contrast to the OPA-based systems previously demonstrated by other groups. In addition to only requiring one input beam, the use of a SPOPO will allow for significantly higher efficiency of MIR generation as well as higher average powers. Moreover, a SPOPO allows for wavelength tuning without the need for a tunable pump source.

The results presented in this chapter examine the feasibility of the system for adaptive MIR pulse shaping, showing control over the temporal shape of the pulse, demonstrating pulse compression and the generation of a double pulse [10]. The results also highlight the need for further investigation into pulse shape transfer in the SPOPO for control of the spectral resolution of MIR pulses, as will be discussed in later in Chapters 5 and 6.

The experimental work in this chapter was carried out in collaboration with Naveed Naz, who constructed the OPO used in this experiments, whilst I was involved with the build and development of the MIR autocorrelator as well as the acquisition of the MIR autocorrelation data.

4.2 Detailed system outline

A schematic of the pulse shaping system is shown in Fig. 4.1. The source is a mode-locked 1.047 μm Nd:YLF laser (Microlase DPM-1000-120) and delivers ~4 ps pulses at a repetition rate of 120 MHz with a maximum average power of 2 W. The beam was then passed through to a second Nd:YLF laser system (Q-Peak MPS-1047 CW-10) in an amplifier configuration which produced a 4 W average power output.

Near transform-limited pulses of 0.3 nm bandwidth were produced by the laser system. Propagation of these pulses through a ~55 cm length of PM, single-mode fibre (Fibercore, HB980T) increased the bandwidth to 3.5 nm through SPM whilst retaining

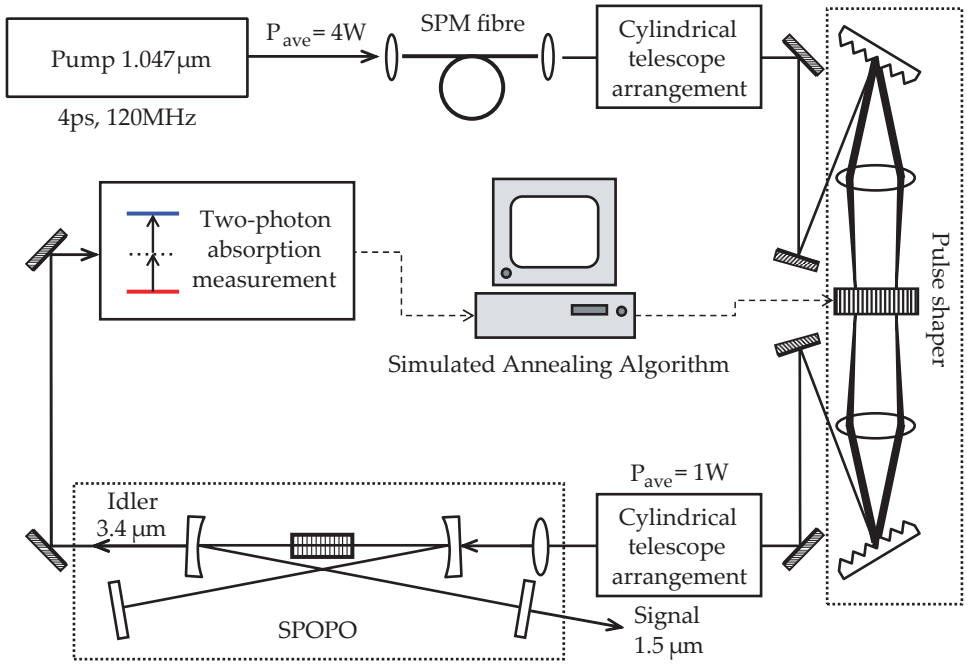

FIGURE 4.1: Full system schematic of the MIR adaptive shaper.

a similar pulse duration. Due to the high intensity of the 4 W beam coupled into the fibre, a $\sim$400 μm length of 125μm diameter coreless fibre was spliced as an endcap to the PM fibre to avoid damage due to heating effects. The resulting coupling efficiency was $\sim$50%.

A cylindrical telescope then expanded the beam in the horizontal direction to fill the 5 cm wide grating of the zero-dispersion pulse compressor in which the NIR pulse was temporally shaped using a phase-only 128-pixel liquid crystal SLM (CRI SLM-128-MIR). The beam was incident at an angle of 53.4° to the grating, which had a groove density of 1714 grooves per mm, and exited with a diffracted angle of 82.7°. The bandwidth of the input beam filled the 12.8 mm aperture of the SLM at the FP with a wavelength-to-space mapping of 0.3 nm/mm. The initial spatial expansion of the beam to fill the grating was necessary to maximise the shaper resolution to 0.02 nm corresponding to an available complexity, η, of 181 and a time window of 84 ps. Note, however, that the pixellated nature of the SLM limited the overall complexity to 128 and therefore the time window to 59 ps. The individually shaped frequencies were recombined at a second grating which was angled at 82.7° such that the shaped NIR beam was diffracted out of the shaper at an angle of 53.4°. The shaper arrangement was therefore symmetric at

the FP and the spatial profile of the output beam was the same as the input. The NIR elliptical beam leaving the shaper was then spatially reshaped to a circular beam with a series of cylindrical telescopes before it was delivered to the SPOPO.

The SPOPO was arranged in a bow-tie configuration which was comprised of two curved mirrors with a radius of curvature of 150mm and two flat mirrors. The cavity mirrors were highly transmitting at the pump wavelength and highly reflecting (HR) at the signal wavelength, from 1.2 to 2.0 μm, although one of the flat mirrors could be replaced with a 65% reflecting output coupler (OC). The effect of off-axis beam distortions due to the angled curved mirrors, known as comatic aberrations [11, Sec. 5.3], was minimised by keeping the reflected angle to within a few degrees. The flat mirrors were arranged such that they retro-reflected the signal beam rather than support a ring cavity configuration. Although this results in higher loss due to a double pass through the PPLN, the retro-reflecting arrangement allows for easy cavity length adjustment and hence a simpler alignment. Stable operation could be achieved at three times above threshold where the OPO worked with good efficiency whilst avoiding back-conversion [12, 13]. Having an OC instead of a HR mirror increases the threshold such that higher idler output powers can be achieved in this stable regime. A maximum average power of 1W could be delivered to the OPO.

The pump beam was focused with a 150 mm focal length lens into a 10.7 mm-long PPLN crystal, heated at 120°C, to a spot size ($1/e^2$ radius of intensity) of 44 μm for which the measured M^2 values were 1.6 and 1.5, in the horizontal and vertical directions, respectively. The embedded fundamental Gaussian mode [14, Chap. 11] of the beam corresponded to near-confocal focusing in the crystal. A poling period of 29.2 μm was chosen, resulting in a signal wavelength of 1508 nm and an idler wavelength of 3440 nm. With no phase applied by the shaper, the OPO had a threshold of 100 mW. Note that the choice of wavelength was not critical for these experiments, although a large tuning range was available.

The pump autocorrelations were measured with a commercial background free autocorrelator. Figure 4.2 shows the AC trace of the chirped pump pulse with a pulse width

of 4.2 ps assuming a sech^2 pulse shape, which is typical of the additive pulse mode-locked laser used here. The pump spectrum was measured with an OSA and is shown in Fig 4.2(b) showing four spectral peaks due to SPM broadening of ∼10 rad. A theoretical compressed pulse is shown by the red dashed curve in Fig. 4.2(a) and is calculated from a Fourier transform (FT) of the spectrum with flat phase, showing that the pulse could be compressed to an AC FWHM of ∼800 fs, which corresponds to a pulse intensity FWHM of ∼600 fs. Characterisation of the MIR idler pulses was achieved with a fringe-

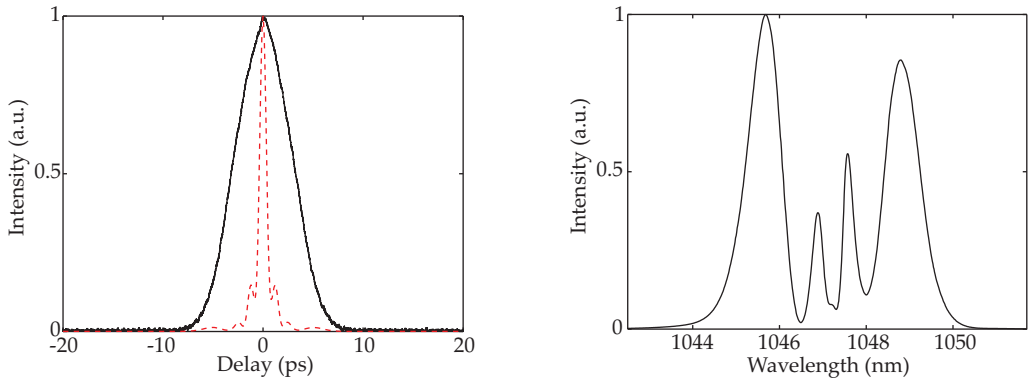

FIGURE 4.2: (a) Autocorrelation of a chirped pump (solid curve) with the theoretical flat phase AC calculated from a FT of the measured spectrum (red dashed); (b) pump spectrum due to SPM broadening.

resolved autocorrelator which was built in a Michelson interferometer configuration with an extended InGaAs detector for TPA (see Section 3.2.1 for a fuller description of the autocorrelator used here).

Pulse shaping was achieved by relaying a feedback signal to a computer to optimise the phase applied by the SLM using a SA algorithm written by Naveed Naz. A Taylor series expansion was used to represent the phase profile where the Taylor coefficients correspond to nth order dispersion as was discussed earlier in Section 2.2.1, Eqn. 2.19. The first two terms of the expansion for the phase offset and group delay could be ignored and the dispersion terms, $\beta_2 - \beta_4$, were used as optimisation parameters for the SA algorithm.

The SA algorithm is based on the ASA algorithm developed by Ingber [15, 16], which was developed as a much faster algorithm than the Boltzmann or Cauchy-Lorentz based SAs [17, 18]. The code made use of the generating function and optimal annealing

schedule, although the implementation of re-annealing was not included. The SA used in this experiment typically converged within 500 iterations which took 125 seconds due to the 4 Hz refresh rate of the SLM.

4.2.1 Numerical Simulation

Initial analysis of the experiment considered the phase required by the pulse shaper to compress the pump pulse, thereby lowering the OPO threshold. Full compression of the pump pulse could be achieved if the applied phase cancelled out the phase induced by SPM in the fibre. However, due to the 4th order Taylor series approximation of the phase profile, a perfect flat phase pulse cannot be achieved. Numerical modelling of the SPM-chirped pump pulse (τ_p =4.2 ps, maximum SPM phase = 10 rad) was carried out to compare the quality of pulse compression from a 4th order Taylor series approximation of the phase to a pulse with a perfect flat phase. The spectral intensity profile of the modelled pump pulse is shown in Fig. 4.3(a) with the spectral phase shown by the solid red curve. Ideally, to compress the pulse, the phase applied by the pulse shaper should follow this exact phase profile, except for an inversion, to result in a perfect flat phase. We theoretically achieve this complete pulse compression by applying a flat phase to the spectral amplitude and performing a fast Fourier transform, resulting in a fully compressed pulse which is shown by the solid line in Fig. 4.3(b).

To adaptively achieve the required phase to be applied by the shaper, control of each individual pixel would provide an accurate, but computationally expensive optimisation method. By approximating the phase profile to a 4th order Taylor series expansion, the optimisation algorithm now has the three terms, β_2, β_3, and β_4, to optimise. Numerical modelling of adaptive pulse compression of the pump pulse found that the pulse could be compressed by an optimum phase profile where β_2 = -0.886 ps^2rad^{-1}, β_3 = 0 ps^3rad^{-2}, and β_4 = 0.164 ps^4rad^{-3}. This adaptively optimised phase shows a close match to the unshaped spectral phase in Fig. 4.3(a) where the applied phase has been inverted for comparison. Due to the 4th order approximation, the high frequency phase modulation near the centre frequency could not be followed. However, the resulting shaped intensity profile shown by the red dashed curve in Fig. 4.3(b) shows a good match to the perfect

flat phase pulse except for slightly larger wings in the profile. We can therefore conclude that in these numerical simulations the 4th order Taylor series expansion results in a good approximation to the phase profile required for a flat phase pulse.

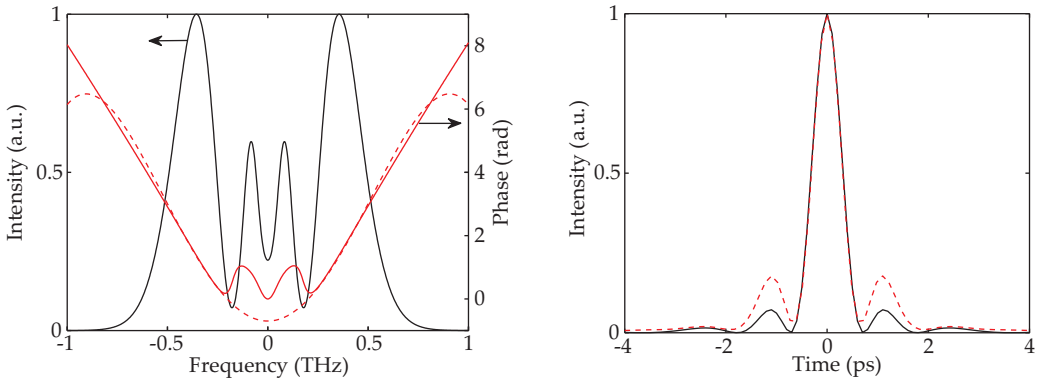

FIGURE 4.3: Numerical data for, (a) the pump spectrum due to SPM (solid curve) with the spectral phase (solid red) and the applied fourth order inverted phase required to compress the pulse (dashed red); (b) the flat phase pump intensity profile (solid curve) and the adaptively compressed phase (dashed red).

4.3 Experimental results

The results described in this section experimentally demonstrate adaptive optimisation of a MIR pulse for pulse compression and double pulse generation. For pulse compression, the applied phase profile agreed well with the above numerical predictions of $\beta_2 - \beta_4$ described in Section 4.2.1 to completely compensate for the 2nd and 4th order dispersion induced by SPM in the fibre. Optimisation was achieved by maximising the OPO signal power or the TPA of the MIR idler output. The generation of a double pulse was also achieved by maximising the TPA of the MIR, but an interferometer arrangement, where the two arms were offset, was used. In this configuration, the SA algorithm would optimise the overlap between a leading and lagging pulse.

4.3.1 Pulse compression for OPO threshold minimisation

Before the adaptive shaping experiments, the numerically calculated $\beta_2 - \beta_4$ phase was applied and resulted in pulse compression of the pump pulse to 800 fs, assuming a sech^2

intensity profile, and a reduction in SPOPO threshold from 100 mW to 48 mW. Figures 4.4 (a) and (b) show the measured idler FRAC traces before and after applying the theoretical phase with the corresponding intensity ACs shown in Fig. 4.4(c). The intensity ACs were extracted from the FRAC data by filtering out the high frequencies that cause the interference fringes. As a result of the numerically calculated phase, the chirped idler pulse is compressed from an AC FWHM of 1.90 ps to 960 fs which corresponds to 620 fs assuming a sech^2 pulse shape. This is very close to the compression limit which is also shown by the blue in Fig. 4.4(c). This is the FT limit due to the measured idler spectrum shown in Fig. 4.4(d).

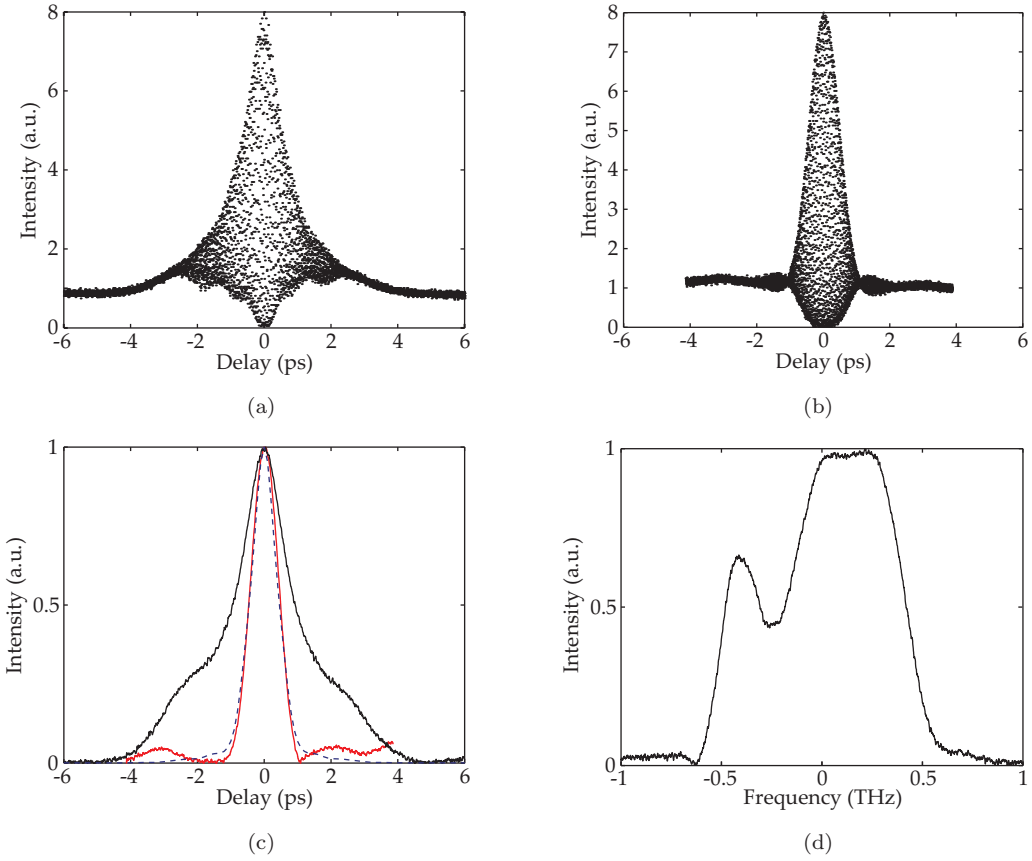

FIGURE 4.4: (a) Idler FRAC trace with no shaping; (b) Idler FRAC trace with theoretical phase applied; (c) Intensity ACs of the pulses generated from a frequency filter of the data of (a) (solid curve) and (b) (red curve). The flat phase AC calculated from a FT of the idler spectrum is also shown (blue dashed); and, (d) the spectral intensity of the idler pulse.

Having applied the pre-calculated phase, the next experiment looked at adaptive pulse compression. The SPOPO signal output power, as detected by a Ge photodiode, was used as the optimisation parameter with the SPOPO operating at two times above

the unshaped 100mW threshold. The SA algorithm was therefore used to find the $\beta_2 - \beta_4$ parameters that gave the maximum photodiode response. This resulted in an optimal phase whose dispersion parameters matched well to the earlier stated numerical predictions (β_2 = -0.786 $\mathrm{ps^2 rad^{-1}}$, β_3 = -0.0376 $\mathrm{ps^3 rad^{-2}}$ and β_4 = 0.136 $\mathrm{ps^4 rad^{-3}}$). The profile is plotted in Fig. 4.5, along with the pump spectrum, which shows that the applied phase (dashed red) is in good agreement with the numerically expected phase (solid red). The idler pulse that resulted from optimising to the signal power gave a very similar FRAC trace to the non-adaptive result shown in Fig. 4.4(b) so is not shown here. However, this adaptive optimisation resulted in an improvement in SPOPO threshold to 42 mW.

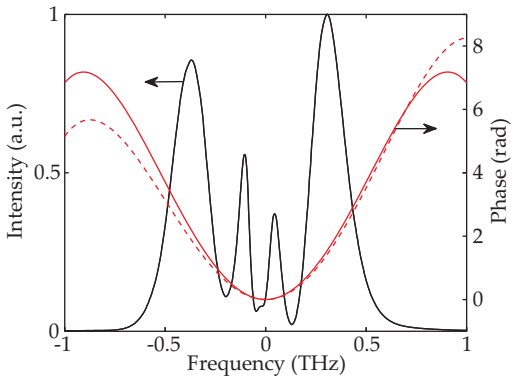

FIGURE 4.5: Comparison of the numerical phase (solid red) and adaptively optimised phase (red dashed) with the pump spectrum (solid) also shown.

It is interesting to note that comparison of the pump and idler spectra, in Fig. 4.4(d) and 4.5, shows that both pulses have similar bandwidth but there is very poor transfer of detail from the pump to the idler. The loss of the central peaks in the spectrum is due to the relatively broad signal spectrum, which was not actively controlled in these experiments. The details of pulse transfer are discussed in later in Chapters 5 and 6.

More direct adaptive control of the idler pulse shaper was demonstrated, by optimising the idler TPA signal in an extended InGaAs photodiode, achieving similar results to those that were obtained by signal power optimisation. The SPOPO used a 65% OC which increased the signal loss of the SPOPO, thereby increasing the threshold. The SPOPO could therefore be operated in a high power regime for a high average power idler output, which could be easily measured by the TPA detector. Taking into account the fact that optimisation of the idler TPA would lower the threshold, the OPO was

operated at only 1.5 times above threshold for the unshaped pump pulse to reduce the chance of reaching back conversion regime during the optimisation process.

Figure 4.6(a) shows the resulting idler FRAC trace with slightly smaller side lobes compared to Fig. 4.4(b). However, the calculated AC FWHM is found to be slightly broader at 1.02 ps corresponding to a pulse width of 660 fs assuming a sech^2 pulse shape. The optimised phase profile had parameters that were still in good agreement with the theoretical values (β_2 = -0.851 $\text{ps}^2\text{rad}^{-1}$, β_3 = 0.00488,$\text{ps}^3\text{rad}^{-2}$ and β_4 = 0.333 $\text{ps}^4\text{rad}^{-3}$) and comparison of the the phase profile in Fig. 4.6(b) shows that it is similar to the calculated phase, for optimum pulse compression, but deviates with larger phase delays at the edge of the spectrum.

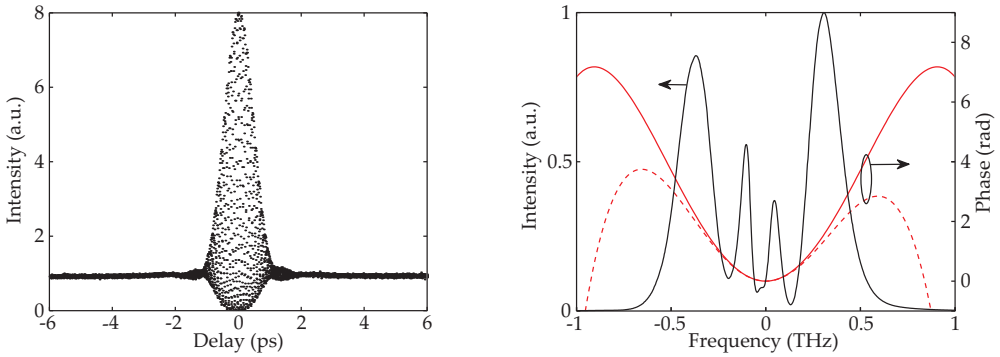

(a) (b)

FIGURE 4.6: (a) FRAC trace of the idler pulse for an optimised idler pulse; (b) Applied phase profiles from theory (solid red), and idler optimisation (red dashed) with the measured pump spectral intensity.

4.3.2 Double pulse generation

Having demonstrated adaptive control of the MIR idler pulse for pulse compression, the experimental results in this section go beyond this simple case and demonstrate the creation of a MIR double-pulse train from a single pump pulse. This was achieved by optimising the idler TPA signal in the autocorrelator setup, with one arm detuned by a fixed distance resulting in an optimised cross correlation signal due to the leading and lagging pulse. Similar to the previous experiment, the SPOPO arrangement used a 65% OC but operation was at four times above threshold as the new threshold, with the shaped pump pulse, was expected to increase.

Figure 4.7 shows the resulting FRACs for two different offsets where the trace showing a definite pulse separation is from the larger offset. It is therefore possible to adaptively generate a double pulse with controllable peak separation. The results of this experiment show the capability of the adaptive pulse shaping system for direct control over the idler beyond simple pulse shapes.

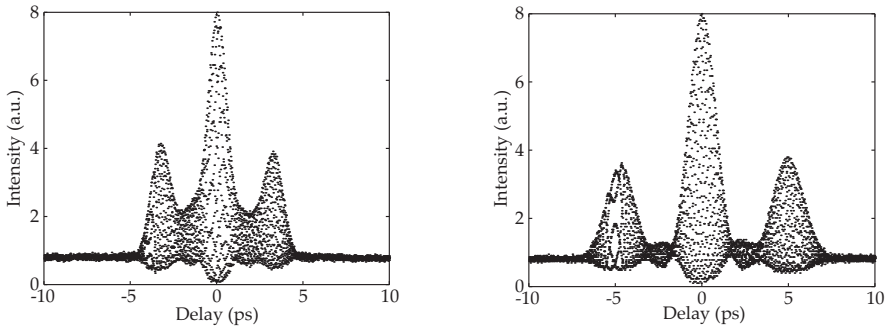

FIGURE 4.7: FRACs of idler double pulse trains where the arm-length detuning is larger in (b) than (a).

4.4 Conclusions

The results in this chapter have demonstrated adaptive control of MIR pulses for simple pulse compression and for the generation of a double pulse train. This proof-of-principle investigation has shown that the system used here has great potential for applications in chemistry, where for example, the optimisation of a fluorescence signal could be used as the feedback parameter to find the complex shaped idler pulse required for a certain experiment. However, Fig. 4.4(d) has highlighted that the idler spectrum has picked up very few features of the pump spectrum. Ideally, the pump characteristics should be transferred to the idler pulse in order to preserve the resolution of control over the adaptive pulse shaping. This *high fidelity transfer* is therefore an important issue when using an indirect pulse shaping method and will be investigated both theoretically and experimentally in Chapters 5 and 6.

Moreover, spectrographic pulse characterisation techniques for a more complete picture of the pulses are required, to develop a better understanding of the pulse shaping and

pulse transfer mechanisms involved. The design and build of a sonogram for both the pump and idler wavelengths was carried out and later used for the experimental investigation of pulse transfer in an SPOPO in Chapter 6.

As well as demonstrating adaptive control of MIR pulses, the results in this chapter also show that the adaptive pulse shaping loop works efficiently due to the implementation of the SA algorithm. The simple demonstration of adaptive pulse compression has many applications particularly in high power fibre CPA systems where dispersion and nonlinear effects can degrade pulse quality. The implementation of an adaptive phase-only pulse shaping system, based on the one demonstrated here, to a fibre CPA system, is shown later in Chapter 7. The results of the CPA experiments carried out are a crucial step in the progression from this *picosecond* system to a high power *femtosecond* adaptive MIR pulse shaping system for which the timescales should allow for the demonstration coherent control experiments.

References

[1] S. H. Shim, D. B. Strasfeld, E. C. Fulmer, and M. T. Zanni, "Femtosecond pulse shaping directly in the mid-IR using acousto-optic modulation," *Opt. Lett.* **31**(6), pp. 838–840, 2006.

[2] S. H. Shim, D. B. Strasfeld, and M. T. Zanni, "Generation and characterization of phase and amplitude shaped femtosecond mid-IR pulses," *Opt. Express* **14**(26), pp. 13120–13130, 2006.

[3] D. B. Strasfeld, S.-H. Shim, and M. T. Zanni, "Controlling vibrational excitation with shaped Mid-IR pulses," *Phys. Rev. Lett.* **99**(3), pp. 038102–4, 2007.

[4] F. Eickemeyer, R. A. Kaindl, M. Woerner, T. Elsaesser, and A. M. Weiner, "Controlled shaping of ultrafast electric field transients in the mid-infrared spectral range," *Opt. Lett.* **25**(19), pp. 1472–1474, 2000.

[5] T. Witte, D. Zeidler, D. Proch, K. L. Kompa, and M. Motzkus, "Programmable amplitude- and phase-modulated femtosecond laser pulses in the mid-infrared," *Opt. Lett.* **27**(2), pp. 131–133, 2002.

[6] H. S. Tan and W. S. Warren, "Mid infrared pulse shaping by optical parametric amplification and its application to optical free induction decay measurement," *Opt. Express* **11**(9), pp. 1021–1028, 2003.

[7] H. S. Tan, E. Schreiber, and W. S. Warren, "High-resolution indirect pulse shaping by parametric transfer," *Opt. Lett.* **27**(6), pp. 439–441, 2002.

[8] T. Witte, K. L. Kompa, and M. Motzkus, "Femtosecond pulse shaping in the mid infrared by difference-frequency mixing," *Applied Physics B: Lasers and Optics* **76**(4), pp. 467–471, 2003.

[9] M. Tsubouchi and T. Momose, "Femtosecond pulse shaping in the mid-infrared generated by difference-frequency mixing: a simulation and experiment," *J. Opt. Soc. Am. B* **24**(8), pp. 1886–1900, 2007.

[10] N. A. Naz, H. S. S. Hung, M. V. O'Connor, D. C. Hanna, and D. P. Shepherd, "Adaptively shaped mid-infrared pulses from a synchronously pumped optical parametric oscillator," *Opt. Express* **13**(21), pp. 8400–8405, 2005.

[11] M. Born and E. Wolf, *Principles of optics*, Electromagnetic theory of propagation interference and diffraction of light, Pergamon Press, 6th (with corrections) ed., 1983.

[12] E. C. Cheung and J. M. Liu, "Theory of a synchronously pumped optical parametric oscillator in steady-state operation," *J. Opt. Soc. Am. B* **7**(8), pp. 1385–1401, 1990.

[13] M. J. McCarthy and D. C. Hanna, "All-solid-state synchronously pumped optical parametric oscillator," *J. Opt. Soc. Am. B* **10**(11), p. 2180, 1993.

[14] O. Svelto and D. C. Hanna, *Principles of lasers*, Springer, 4th ed., 1998.

[15] L. Ingber, "Very fast simulated re-annealing," *Mathematical and Computer Modelling* **12**(8), pp. 967–973, 1989.

[16] L. Ingber, "Simulated annealing: Practice versus theory," *Mathematical and Computer Modelling* **18**(11), pp. 29–57, 1993.

[17] S. Geman and D. Geman, "Stochastic relaxation, Gibbs distributions, and the Bayesian restoration of images," *IEEE Transactions on Pattern Analysis and Machine Intelligence* **6**(6), pp. 721–741, 1984.

[18] H. Szu and R. Hartley, "Fast simulated annealing," *Physics Letters A* **122**(3-4), pp. 157–162, 1987.

Chapter 5

Numerical Modelling of Parametric Transfer

5.1 Introduction

In the previous chapter adaptive shaping of a MIR pulse via a SPOPO was experimentally demonstrated via an indirect shaping approach. Shaped MIR pulses were achieved by initial shaping of the pump pulse using a phase-only pulse shaper before transferring the pump pulse shape to the MIR idler pulse. Although the results of adaptive pulse shaping for pulse compression and double-pulse generation were successful, comparison of the input pump and output idler spectra showed minimal resemblance. This therefore raised the question of the fidelity of transfer in a parametric process, which will be discussed here.

In this chapter, numerical modelling of parametric transfer in PPLN will be investigated. Initial analysis will be carried out for a single-pass DFG process [1] in Section 5.2, before extending the work to a full analysis of parametric transfer in a SPOPO [2] in Section 5.3.

The numerical work in this chapter was carried out by Jerry Prawiharjo, whilst I was involved in the analysis of the results obtained and which parametric transfer effects should be numerically investigated. Preliminary experiments of parametric transfer

in an SPOPO were carried out, prior to these numerical investigations, by myself and Naveed Naz. I also carried out the experimental investigations described later in Chapter 6 for confirmation of the numerical results presented here.

5.2 Parametric Transfer Theory for Difference Frequency Generation

Consider the DFG process depicted in Fig. 5.1 in which a shaped NIR ultrashort pump pulse with a centre frequency, ω_p, is mixed collinearly with a NIR signal pulse at a centre frequency, $\omega_s < \omega_p$. Through the process of DFG in a second-order nonlinear material, an idler pulse in the MIR regime with a centre frequency at $\omega_i = \omega_p - \omega_s$ is generated.

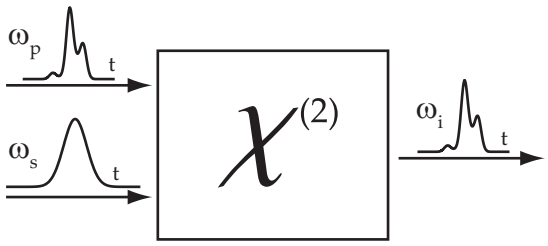

FIGURE 5.1: Illustration of indirect pulse shaping via parametric transfer by DFG.

In this scheme, it is intended that the pump pulse shape is transferred to the idler. This has been experimentally demonstrated in Ref. [3], but other schemes in which the signal pulse shape is transferred have also been demonstrated [4–6].

5.2.1 The convolution relation

In this section, a theoretical analysis of the parametric transfer process, which is similar to the frequency domain treatment used in Refs. [7] and [8], is presented. In order to simplify our analysis here, we consider a collinear geometry with a non-critical phase-matching condition, and assume plane-wave fields.

In Section 2.3.4, a simple frequency domain analysis of DFG was performed in which a simple convolution relationship, between the pump, signal and idler fields, was derived

for the simple case where no dispersion, no pump depletion and no signal amplification, is assumed. The convolution given by Eqn. 2.65 and is redefined here with an additional parameter, τ_{ps}, for the temporal delay between the pump and signal pulses at the crystal input face,

$$\begin{aligned} \widetilde{A}_i(L,\Omega_i) &= i\alpha_i \widetilde{A}_p \otimes \widetilde{A}_s^* \\ &= i\alpha_i \int_{-\infty}^{\infty} \widetilde{A}_p(0,\Omega_s+\Omega_i)\widetilde{A}_s^*(0,\Omega_s)\exp(-i\tau_{ps}\Omega_s)d\Omega_s \,. \end{aligned} \tag{5.1}$$

or in the time domain,

$$A_i(L,t) = i\alpha_i A_p(0,t)A_s^*(0,t-\tau_{ps}) \,, \tag{5.2}$$

where α_i is the nonlinear coupling coefficient at the idler wavelength defined in Eqn. 2.40, L is the length of the nonlinear crystal, and $\Omega_j = \omega - \omega_j$ is the frequency detuning, where j represents the subscripts *p, s, i* which denote the pump, signal, and idler, respectively. Note that the time delay, τ_{ps}, is defined such that a negative delay corresponds to the signal arriving at the crystal face at a later time. Finally, $\widetilde{A}_j(L,\Omega_j)$ is the Fourier transform of $A_j(L,t-\tau_{ps})$ and is the slowly varying electric field envelope at the crystal exit face in the frequency domain and comes from the following description of the electric field,

$$\widetilde{E}_j(z,\Omega_j) = \widetilde{A}_j(z,\Omega_j) exp\left[ik(\omega_j+\Omega_j)\right] z \,. \tag{5.3}$$

Furthermore, $\widetilde{A}_j(z,\Omega_j)$ can be written as,

$$\widetilde{A}_j(z,\Omega_j) = \psi(z,\Omega_j) exp[i\phi(z,\Omega_j)] \,, \tag{5.4}$$

where $\psi(z,\Omega_j)$ is the spectral amplitude profile, and $\phi(z,\Omega_j)$ is the spectral phase.

Equation 5.1 states that the pump pulse amplitude and phase can be transferred perfectly to the idler, if the signal field is a delta function. However, approximation of this delta function to a pulse with a narrow spectrum will yield good transfer fidelity if the signal spectrum is narrow with respect to the finest spectral detail of the pump

spectrum that is to be transferred. In addition, the signal pulse must be symmetric to preserve the transfer of the pump pulse intensity, and the signal pulse must be chirp free to preserve the transfer of the relative phase of the pump pulse. Full temporal overlap ($\tau_{ps} = 0$) between the interacting pulses is also required.

For the purposes of this study, the shaped pump pulse to be transferred to the idler is similar to the experimental SPM chirped pulse used previously in Chapter 4. Since pulse shaping can often be required to deal with complex pulses, the investigation of parametric transfer of a highly chirped complex pulses is of general interest.

The pump pulse is described as an unchirped Gaussian pulse which has undergone SPM in a Kerr medium, such as a length of PM fibre, resulting in a maximum intensity dependent phase-shift of 10 rad.

$$A_p(t) = A_p^{(0)} f(t) \exp\left(i10|f(t)|^2\right), \tag{5.5}$$

where $A_p^{(0)}$ is the pump envelope peak, and $f(t)$ is the normalised temporal intensity profile given by,

$$f(t) = \exp\left[-2\ln 2\left(\frac{t}{\delta t_p}\right)^2\right], \tag{5.6}$$

where δt_p is the FWHM. We chose a temporal FWHM of 1 ps, leading to a spectral FWHM of 4.44 THz, equivalent to ∼16 nm for a central wavelength at around 1 μm. Such a spectral FWHM is able to support transform-limited Gaussian pulses with a temporal FWHM of ∼100 fs and is of the order that would be expected from the proposed fibre CPA pump system (see Chapter 7). Figure 5.2 shows the temporal and spectral characteristics of the pump pulse. Note that the lower frequency peak is at the leading edge of the pulse, while the higher frequency peak at the trailing edge.

Using the form of the pump pulse given in Eqn. 5.5, and the convolution relation given in Eqn. 5.2 the transfer fidelity to the idler for transform-limited Gaussian signal pulses of varying width will now be considered. Figure 5.3(a) shows the generated idler spectrum for signal pulses with temporal FWHM of 1 ps, 2 ps, and 3 ps, corresponding to spectral FWHM of 0.44 THz, 0.22 THz, and 0.15 THz respectively, and with the pump spectrum shown by the solid curve for comparison. The figure shows that as the signal pulse width

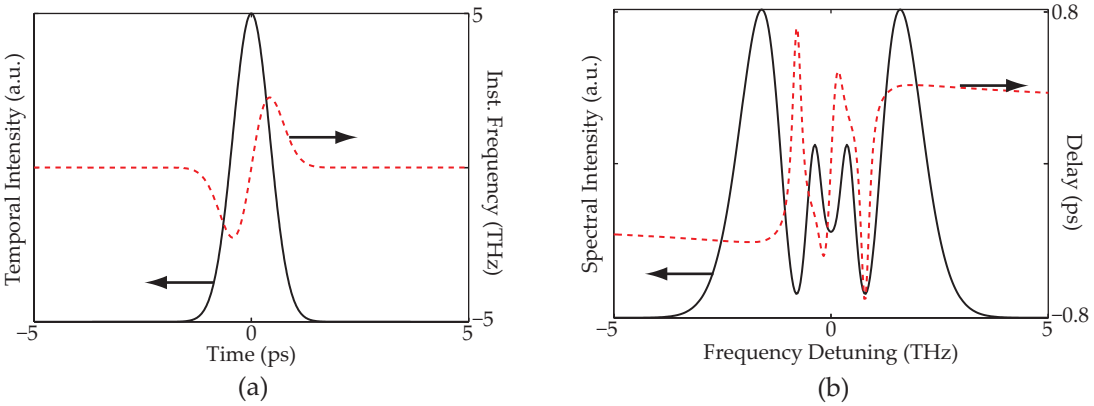

FIGURE 5.2: a) Temporal intensity and instantaneous frequency, and b) spectral intensity and group delay of the input pump pulse.

increases (spectral width narrows), the spectral transfer improves, indicating that the width of the signal pulse effectively controls the spectral transfer resolution. Although one can qualitatively observe the trend here, more detailed analysis of the system will require a quantitative measure of transfer fidelity.

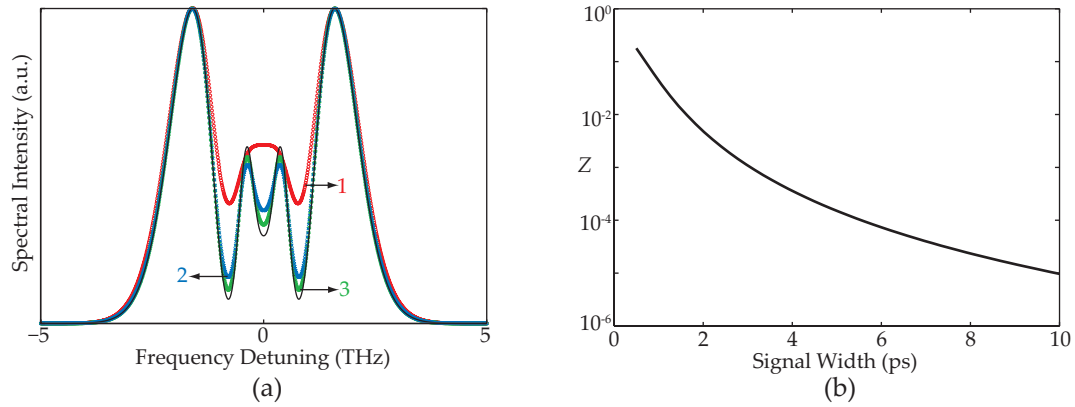

FIGURE 5.3: a) Spectral intensities of the generated idler pulses from the interaction between pump pulses as described in the text and transform-limited Gaussian signal pulses of temporal FWHM 1 ps (red), 2 ps (blue), 3 ps (green) and with the pump spectrum shown by the solid curve. b) Transfer fidelity Z in logarithmic scale as a function of the signal pulsewidth.

The expression below defines a quantitative measure for the fidelity of parametric transfer in terms of the spectral phase and intensity,

$$Z = 1 - \frac{\int S_p(\Omega, \tau_{ps}; z = 0) S_i(\Omega, \tau_{ps}; z = L) d\Omega d\tau_{ps}}{\left[\int S_p^2(\Omega, \tau_{ps}; z = 0) d\Omega d\tau_{ps} \int S_i^2(\Omega, \tau_{ps}; z = L) d\Omega d\tau_{ps}\right]^{\frac{1}{2}}}, \tag{5.7}$$

where the polarization gate spectrogram $S_j(\Omega, \tau_{ps}, z)$, is the mathematical description of the polarization gate FROG, and is given by [9],

$$S_j(\Omega, \tau_{ps}; z) = \left| \int_{-\infty}^{\infty} A_j(z,t) \left| A_j(z, t-\tau_{ps}) \right|^2 \exp(i\Omega t) dt \right|^2 . \tag{5.8}$$

The transfer fidelity, Z, is therefore a quantitative measure of the overlap between the spectrograms of the output idler pulse and the input pump pulse. Its value ranges from 0, indicating a perfect overlap, to 1, indicating no overlap.

Applying Eqn. 5.7 to the numerical data for Fig. 5.3(a) results in a transfer fidelity Z of 4.38×10^{-2}, 4.83×10^{-3}, and 1.08×10^{-3}, for signal temporal widths of 1 ps, 2 ps, and 3 ps, respectively. Figure 5.3(b) shows the trend of how the transfer fidelity improves with increasing signal pulse width. For perfect overlap, the convolution relation requires that the signal spectrum is a delta function but this can not be achieved in practice. We therefore choose a limit to Z, $Z < 5 \times 10^{-3}$, that we define as an acceptable level of transfer fidelity. Note that in practice, the choice of the signal spectral FWHM depends on the finest spectral structure of the shaped pump pulse that we wish to transfer.

5.2.2 Theoretical Analysis of Parametric Transfer in Dispersive Media

We have so far considered the simple DFG process under the conditions where there is no pump depletion, no signal amplification and no dispersion and as a result, only the form of the signal affects the transfer fidelity. Experimentally, these ideal conditions can be achieved with very low input powers and short crystal lengths to avoid pump depletion and signal amplification. However, this would result in very low conversion efficiency to the MIR idler, seriously restricting the practicality of the device. To increase conversion efficiency, the analysis is extended to longer crystal lengths such that chromatic dispersion becomes important but where negligible pump depletion and signal amplification are still assumed. Due to chromatic dispersion, the interacting pulses travel at different group velocities in the nonlinear medium. This is known as group velocity mismatch (GVM) and leads to a temporal walk-off between the pulses at the crystal exit face. Chromatic dispersion also causes group velocity dispersion (GVD)

whereby different spectral components of a single pulse travel at different speeds (or phase velocities) causing temporal broadening of the pulse.

Earlier analysis of parametric transfer in Section 2.3.4 showed an expression for the generated idler pulse under the above-mentioned conditions of chromatic dispersion and no pump depletion or signal amplification. Equations 2.61 to 2.64 are redefined here.

$$\begin{aligned}\widetilde{A}_i(L,\Omega_i) &= \int_{-\infty}^{+\infty} i\alpha_i \widetilde{A}_p(\Omega_s+\Omega_i)\widetilde{A}_s^*(\Omega_s)\exp(i\tau_{ps}\Omega_s) \\ &\quad \times L\,\mathrm{sinc}\left[\Delta k_{DFG}(\Omega_s,\Omega_i)\frac{L}{2}\right]\exp\left[i\Delta k_{DFG}(\Omega_s,\Omega_i)\frac{L}{2}\right]d\Omega_s\,, \end{aligned} \quad (5.9)$$

where, to a second order approximation, $\Delta k_{DFG}(\Omega_s,\Omega_i)$ is given by,

$$\Delta k_{DFG}(\Omega_s,\Omega_i) = \Delta k_0 + \Omega_s\delta\nu_{ps} + \Omega_i\delta\nu_{pi} + \frac{1}{2}\left[\Omega_s^2\delta b_{ps} + \Omega_i^2\delta b_{pi} + b_p\Omega_s\Omega_i\right]\,, \quad (5.10)$$

where $\Delta k_0 = k(\omega_p) - k(\omega_s) - k(\omega_i)$ is the wavevector mismatch, $\delta\nu_{jk}$ is the GVM parameter between the group velocities ν_j and ν_k,

$$\delta\nu_{jk} = \frac{1}{\nu_j} - \frac{1}{\nu_k} \quad , \quad \nu_j = \left[\frac{dk(\omega)}{d\omega}\right]^{-1}_{\omega=\omega_j}\,, \quad (5.11)$$

and δb_{jk} is the GVD mismatch between the GVD parameters b_j and b_k,

$$\delta b_{jk} = b_j - b_k \quad , \quad b_j = \left.\frac{d^2k(\omega)}{d\omega^2}\right|_{\omega=\omega_j}\,. \quad (5.12)$$

To simplify the problem the individual trends, for each of the terms in Eqn. 5.10 on the parametric transfer, will be presented under the assumption that all interactions are phase matched, i.e. $\Delta k_0 = 0$. Before this numerical investigation, we consider the analytical expressions of the idler pulse in the first order approximation of the wavevector mismatch, $\Delta k_{DFG}(\Omega_s,\Omega_i)$. i.e.,

$$\Delta k_{DFG}(\Omega_s,\Omega_i) = \Omega_s\delta\nu_{ps} + \Omega_i\delta\nu_{pi}\,. \quad (5.13)$$

The wavevector mismatch is now reduced to only two terms and the effect of each of these individual terms will now be considered analytically. In the case where the GVM

between the pump and signal pulses, $\delta\nu_{ps}$ can be ignored, Eqn. 5.9 becomes,

$$\begin{aligned}\widetilde{A}_i(L,\Omega_i) &= i\alpha_i \int_{-\infty}^{\infty} \widetilde{A}_p(\Omega_s+\Omega_i)\widetilde{A}_s^*(\Omega_s)\exp(i\tau_{ps}\Omega_s) \\ &\quad \times L\,\mathrm{sinc}\left[\Omega_i\delta\nu_{pi}\frac{L}{2}\right]\exp\left[i\Omega_i\delta\nu_{pi}\frac{L}{2}\right]d\Omega_s\,, \end{aligned} \tag{5.14}$$

In this expression, the sinc function and exponential term are not dependent on Ω_s so they can be factored out of the integral. Equation 5.14 can then be rewritten as,

$$\widetilde{A}_i(L,\Omega_i) = D(L,\Omega_i)[\widetilde{A}_p \otimes \widetilde{A}_s^*]\,, \tag{5.15}$$

where,

$$D(L,\Omega_i) = i\alpha_i\, L\,\mathrm{sinc}\left[\Omega_i\delta\nu_{pi}\frac{L}{2}\right]\exp\left[i\Omega_i\delta\nu_{pi}\frac{L}{2}\right]\,, \tag{5.16}$$

Equation 5.15 shows that the idler field is given by a filter function, $D(L,\Omega_i)$ acting on a convolution between the pump and signal. The filter function is described by a sinc function with a FWHM given by $\delta f = 0.88/(\delta\nu_{pi}L)$. Note that this resembles the acceptance bandwidth for the pump wavelength, which was defined earlier in Eqn. 2.50. When the bandwidth of this filter is much larger than the spectral FWHM of the pump pulse, then the effect on the parametric transfer will be negligible. However, when the filter bandwidth is comparable to the pulse bandwidths, the sinc term dominates and spectral clipping will occur, thus degrading the parametric transfer. Therefore, one must ensure that the FWHM of the filter function is much larger than the pump FWHM to avoid this spectral clipping, which can be achieved with having a relatively small temporal walk-off between the pump and idler given by, $\delta\nu_{pi}L$.

We now consider the case where $\delta\nu_{pi}$ is negligible, such that Eqn. 5.9 becomes,

$$\begin{aligned}\widetilde{A}_i(L,\Omega_i) &= i\alpha_i \int_{-\infty}^{+\infty} \widetilde{A}_p(\Omega_s+\Omega_i)\widetilde{A}_s^*(\Omega_s)\exp(i\tau_{ps}\Omega_s) \\ &\quad \times L\,\mathrm{sinc}\left[\Omega_s\delta\nu_{ps}\frac{L}{2}\right]\exp\left[i\Omega_s\delta\nu_{ps}\frac{L}{2}\right]d\Omega_s\,, \end{aligned} \tag{5.17}$$

In contrast to the previous case, the sinc function and exponential term are both functions of Ω_s and can be rewritten into the following convolution,

$$\widetilde{A}_i(L,\Omega_i) = \widetilde{A}_p \otimes \widetilde{A}_e \,, \tag{5.18}$$

where $\widetilde{A}_e(\Omega_s)$ is the effective signal field and is given by,

$$\widetilde{A}_e(\Omega_s) = i\alpha_i \, L \,\mathrm{sinc}\left[\Omega_s \delta\nu_{ps}\frac{L}{2}\right] \widetilde{A}_s^*(\Omega_s) \exp\left[i\left(\tau_{ps} + \frac{\delta\nu_{ps}L}{2}\right)\Omega_s\right]. \tag{5.19}$$

In this case, there is no filter function that can cause serious degradation of the transfer fidelity. The idler is instead given by a simple convolution between the pump and an effective signal pulse, which is essentially a time-delayed filtered signal pulse. In order to achieve good transfer fidelity, the effective signal pulse must have a narrow signal bandwidth, which was also derived in the previous section for a dispersion-free model. Here, the sinc filter actually improves the parametric transfer since as it becomes narrower, it reduces the spectral FWHM of the effective signal pulse, $\widetilde{A}_e$. However, there is also a time delay factor in the exponential term of Eqn. 5.19, which can degrade the transfer. This can be avoided if a time delay of $\tau_{ps} = \tau_c = -\delta\nu_{ps}L/2$ is introduced between the input pump and signal pulses. This results in the signal walking through the pump pulse symmetrically in the crystal such that the pump-signal delay as the pump enters the crystal, is the same as the signal-pump delay as the pump exits the crystal.

The analysis from this section has found that high fidelity parametric transfer in a dispersive material can be achieved if the pump-idler temporal walk-off, $\delta\nu_{pi}L$, is small to avoid spectral clipping, and if a temporal delay between the pump and signal pulses is introduced to ensure a symmetric temporal overlap in the crystal.

5.2.3 Numerical Analysis of Parametric Transfer

In the previous section, a frequency-domain analysis provided a qualitative understanding of the parametric transfer process in DFG. A more quantitative understanding can be obtained with an extensive numerical simulation based on the coupled-wave equations

which were defined earlier in Section 2.3.2. Equations 2.37 to 2.38 are redefined here.

$$\begin{aligned}
\frac{\partial A_p}{\partial z} + \frac{1}{u_p}\frac{\partial A_p}{\partial t} + \frac{ib_p}{2}\frac{\partial^2 A_p}{\partial t^2} &= i\alpha_p A_s A_i \exp(-i\Delta k_0 z), \\
\frac{\partial A_s}{\partial z} + \frac{1}{u_s}\frac{\partial A_s}{\partial t} + \frac{ib_s}{2}\frac{\partial^2 A_s}{\partial t^2} &= i\alpha_s A_p A_i^* \exp(i\Delta k_0 z), \\
\frac{\partial A_i}{\partial z} + \frac{1}{u_i}\frac{\partial A_i}{\partial t} + \frac{ib_i}{2}\frac{\partial^2 A_i}{\partial t^2} &= i\alpha_i A_p A_s^* \exp(i\Delta k_0 z),
\end{aligned} \tag{5.20}$$

Here, $A_p = A_p(z,t)$, $A_s = A_s(z,t)$, and $A_i = A_i(z,t)$. Equation 5.20 includes material dispersion up to GVD, nonlinear evolution of the pump and signal pulses, and the phase-mismatch term.

Equations 5.20 were solved using the symmetric split-step Fourier method [10] with a fourth order Runge-Kutta integrator, in the frame of reference of the pump pulse. We assume that the phase-matching condition is achieved, i.e. $\Delta k_0 = 0$, through appropriate phase-matching methods. The nonlinear coupling coefficients used in our numerical simulations were $\alpha_p = 4.42 \times 10^{-5}\,\mathrm{V}^{-1}$, $\alpha_s = 3.11 \times 10^{-5}\,\mathrm{V}^{-1}$, $\alpha_i = 1.38 \times 10^{-5}\,\mathrm{V}^{-1}$, which corresponds to bulk periodically-poled lithium niobate (PPLN). The length of the material was chosen to be 1 cm, unless stated otherwise. The signal pulse used was a transform-limited Gaussian with a temporal FWHM of 4 ps, yielding a parametric transfer fidelity $Z = 3.6 \times 10^{-4}$ assuming a dispersion-free material, with no pump depletion or signal amplification.

5.2.3.1 Temporal Walk-off

We initially consider the effects of the GVM parameters to confirm the findings of the frequency-domain analysis in the previous section. The quality of the transfer is expected to depend on the GVM and the crystal length, i.e. $\delta\nu_{jk}L$, and we refer to this factor as the temporal walk-off. As with the frequency-domain analysis, in the numerical simulations we ignore GVD and use low input pump and signal intensities such that pump depletion and signal amplification are negligible.

We will begin by studying the effect of the pump-idler temporal walk-off, $\delta\nu_{pi}L$, by defining $\delta\nu_{ps} = 0$. Figure 5.4 shows results of the numerical simulations for the spectral transfer to the idler as $\delta\nu_{pi}L$ increases from 0 to 1 ps, with the pump and signal temporally overlapped ($\tau_{ps} = 0$).

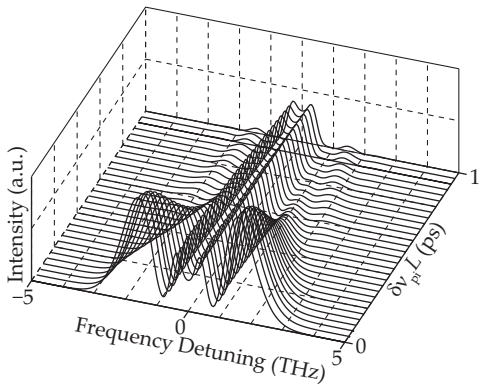

FIGURE 5.4: Generated idler spectra as a function of $\delta\nu_{pi}L$ at $\delta\nu_{ps} = 0$ and $\tau_{ps} = 0$.

When $\delta\nu_{pi}L = 0$, the pump spectrum is transferred well, but as the temporal walk-off increases, the bandwidth of the filter function $D(L, \Omega_i)$ decreases causing spectral clipping. As the sinc function begins to dominate and clip the transferred spectrum, the main spectral peaks decrease in intensity and additional side lobes from the sinc function begin to appear. Parametric transfer for $\tau_{ps} \neq 0$ was also considered but with no compensation of the effects of degradation due to $\delta\nu_{pi}L \neq 0$, and hence no improvement to the fidelity.

The effect of the pump-signal temporal walk-off, $\delta\nu_{ps}L$, by defining $\delta\nu_{pi} = 0$, will now be considered. Figure 5.5(a) shows the numerical results for the generated idler spectra for $\delta\nu_{ps}L = 0$, 0.5, 1 ps, with the input pulses fully temporally overlapped ($\tau_{ps} = 0$). As the pump-signal temporal walk-off increases, the idler spectrum remains mostly unchanged except for a decrease in the higher frequency peak height and a small increase in the lower frequency peak height. This can be explained by considering the nonlinear interaction in the time-domain and the instantaneous frequency of the pump pulse as the signal interacts with different parts of the pulse. When $\delta\nu_{ps}L > 0$, the signal group velocity is higher than that of the pump, so the signal walks through the pump in the nonlinear medium. If the input pulses enter the crystal at the same time, then the peak of the signal pulse walks through the leading edge of the pump pulse, corresponding to the

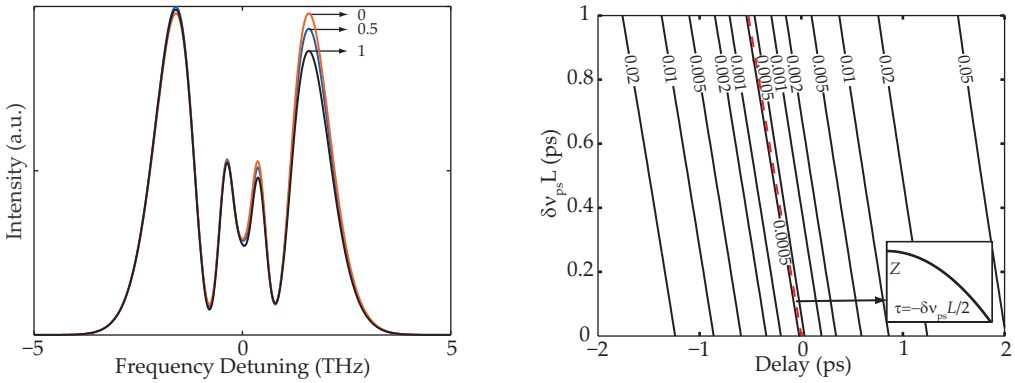

FIGURE 5.5: (a) Generated idler spectra at $\delta\nu_{pi} = 0$ and $\tau_{ps} = 0$ for $\delta\nu_{ps}L = 0, 0.5, 1$ ps, as indicated by the numbers. (b) Contour plot of transfer fidelity Z as a function of $\delta\nu_{ps}L$ and τ_{ps} with $\delta\nu_{pi} = 0$. The inset shows Z along $\tau_{ps} = -\delta\nu_{ps}L/2$ as indicated by the red dashed line. Note that this line is not part of the contour plot, i.e. it does not show a constant value of Z.

lower frequency peak, and the trailing edge of the pulse has significantly less interaction with the signal pulse. Therefore the spectral transfer of the pump pulse's trailing edge, corresponding to the higher frequency peak, is degraded as $\delta\nu_{ps}L$ increases.

Figure 5.5(b) shows the contour plot of the transfer fidelity, Z, as a function of $\delta\nu_{ps}L$ and τ_{ps}. As the temporal walk-off increases, the signal delay corresponding to optimum fidelity also increases. The condition for optimum fidelity occurs at a time delay of τ_c between the input pulses which is indicated by the red dashed line in Fig. 5.5(b). The transfer fidelity along this line improves as $\delta\nu_{ps}L$ increases, as shown by the inset of Fig. 5.5. This is caused by the narrowing of the sinc function of Eqn. 5.19 and the minimisation of Z at $\tau_{ps} = \tau_c$ is due to the symmetric walk-through of the interacting pulses.

5.2.3.2 Pump Depletion and Signal Amplification

In this section, the effect of pump depletion and signal amplification will be considered by increasing the input intensities but ignoring effects due to dispersion. It is expected that the inclusion of these factors will degrade the transfer since the generated idler pulses are no longer proportional to the convolution of the input pulses.

Figure 5.6 shows the contour plot of the transfer fidelity Z as a function of both input pump and signal peak intensities. This figure shows that good parametric transfer, i.e. $Z < 0.005$, occurs for peak intensities of input pump pulses up to $\sim 8\,\mathrm{MW/cm^2}$ and input signal pulses up to $\sim 10\,\mathrm{MW/cm^2}$. To understand this picture more clearly, we consider the effects of pump depletion and signal amplification separately.

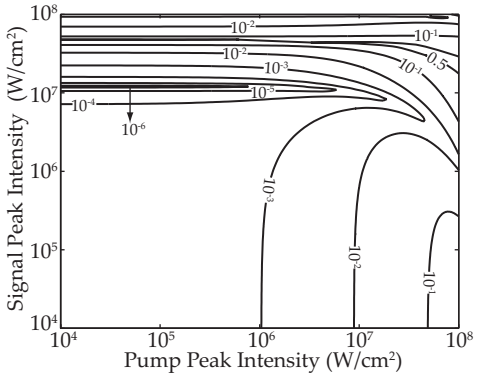

FIGURE 5.6: Contour plot of transfer fidelity Z as a function of input pump and signal peak powers with $\delta\nu_{ps} = \delta\nu_{pi} = 0$, and $\tau_{ps} = 0$.

Figure 5.7(a) shows the transfer fidelity Z as a function of signal peak intensity $I_s^{(0)}$ with input pump peak intensity being kept constant at $I_p^{(0)} = 10\,\mathrm{kW/cm^2}$ such that there is negligible signal amplification for all values of signal peak intensities. The pump depletion, given by $1 - \frac{U_p(L)}{U_p(0)}$, where $U(z) = \int I(z,t)dt$ is the pulse energy, is also shown in Fig. 5.7(a). As the input signal peak intensity increases, the pump depletion increases, but with Z remaining constant for several orders of magnitude before decreasing rapidly as the pump depletion continues to increase until the pump pulse almost completely depleted. At this point, the maximum pump depletion peak coincides with the minimum Z where fidelity of transfer is best. After the depletion, Z starts to increase again due to back-conversion, degrading the transfer fidelity.

The behaviour of the effect due to pump depletion can be explained more fully by considering the problem analytically. Since the pump intensity used in the simulation of Fig. 5.7(a) was such that the signal amplification was negligible, we can ignore the equation for signal pulse evolution in Eqn. 5.20. The temporal derivatives in these equations can also be ignored since we assume no dispersion. Analytically solving the remaining

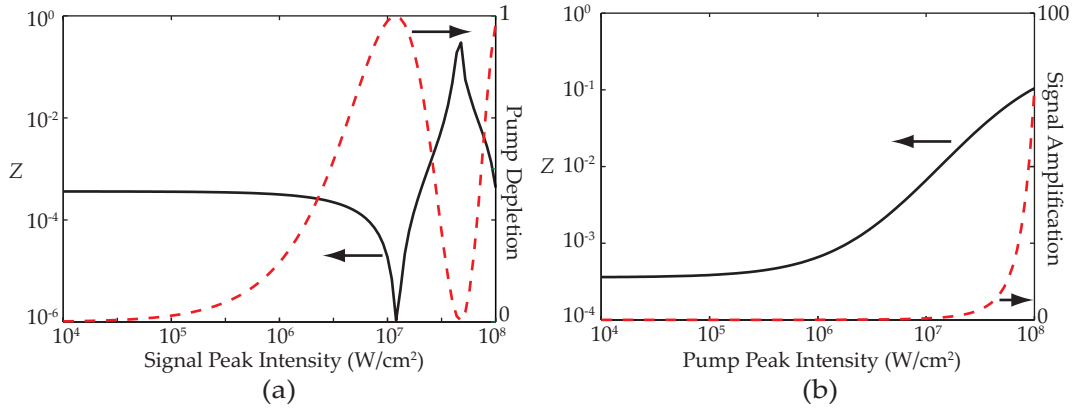

FIGURE 5.7: (a) Transfer fidelity Z and pump depletion as a function of signal peak intensity, with input pump peak intensity being kept constant $10\,\mathrm{kW/cm^2}$. (b) Transfer fidelity Z and signal amplification as a function of pump peak intensity, with input signal peak intensity being kept constant $10\,\mathrm{kW/cm^2}$.

two equations yields the following z dependence of the idler pulse envelope:

$$A_i(z,t) = iA_p(0,t)\sqrt{\frac{\alpha_i}{\alpha_p}}\sin\left[\sqrt{\alpha_i\alpha_p}\,|A_s(0,t)|\,z\right]\exp\left[-i\phi_s(0,t)\right]. \tag{5.21}$$

This expression shows that $A_i(L,t) \propto A_p(0,t)$, and since $A_s(0,t)$ has been chosen to be wider than $A_p(0,t)$, this explains the fact the transfer fidelity is constant over a range of large range of signal peak intensities. The improvement of parametric transfer fidelity due to maximum pump depletion, can be explained by the fact that the signal envelope $|A_s(0,t)|$ is inside a sine function in Eqn. 5.21. As the signal pulse peak intensity is increased, the peak is the part of the pulse that will cause the argument of the sine function to approach $\pi/2$ first. Since the gradient of the sine function around $\pi/2$ is low, the change of the sine term around the high intensity part will be low. Therefore, this term results in an artificial broadening of the signal pulse as its peak intensity is increased, causing the improvement of the parametric transfer fidelity. When the peak signal intensity makes the argument of the sine function equal to $\pi/2$, the pump almost completely depletes, especially as it is narrower than the signal pulse. This condition corresponds to the best transfer fidelity in Fig. 5.7(a). As the signal peak intensity increases further, the argument of the sine function approaches π corresponding to an increase in Z as the fidelity worsens. This coincides with the onset of back-conversion. The fidelity improves as the signal peak intensity is increased further and the argument

of the sine function tends towards $3\pi/2$.

Figure 5.7(b) shows the transfer fidelity Z as a function of the pump peak intensity with the signal peak intensity kept constant at $10\,\mathrm{kW/cm^2}$ such that there is negligible pump depletion for all values of pump peak intensities. The figure also shows the amount of amplification, $\frac{U_s(L)}{U_s(0)} - 1$, experienced by the signal pulse. As the input pump peak intensity increased, the signal was amplified, and correspondingly, transfer fidelity Z increased.

As with the previous case, we can consider the behaviour of the effect of signal amplification on the transfer fidelity analytically. This time we ignore the equation for pump pulse evolution as pump depletion is assumed to be negligible. The remaining two equations can then be solved to yield the following expression:

$$A_i(z,t) = i \sinh\left[\sqrt{\alpha_i \alpha_s}\,|A_p(0,t)|\,z\right] \exp\left[i\phi_p(0,t)\right] \sqrt{\frac{\alpha_i}{\alpha_s}} A_s^*(0,t)\,. \tag{5.22}$$

In contrast to the previous case, $A_i(L,t)$ is not directly proportional to $A_p(0,t)$. Instead, the pump pulse envelope becomes the argument of a hyperbolic sine function. Under conditions of small gain, $\sinh(x) \approx x$, explaining the fact that Z remains constant over a range of pump peak intensities when the gain (or signal amplification) is small. However, as the pump peak intensity increases further, signal amplification becomes larger, and the small gain approximation is no longer valid, causing the parametric transfer fidelity to degrade quickly.

5.2.3.3 Group Velocity Dispersion

The effect of GVD will now be considered. From Eqns. 5.9 and 5.10, the three terms b_p, δb_{ps}, and δb_{pi} are responsible for the GVD effects. In these numerical simulations, we can neglect δb_{ps} since the signal pulse width is sufficiently wide, and both the input pump and signal pulses are in the NIR region. From Eqn. 5.10, one can see that the δb_{ps} term is related to the factor Ω_i^2 and can therefore be factored out of the integration in Eqn. 5.9 yielding a result similar to Eqns. 5.15 and 5.16. The filter function would now have a linear group delay due to the Ω_i^2 term. This linear group delay can be compensated by

introducing an opposite group delay onto the input pump or the output idler pulses. It was found that either scheme of pre- or post-compensation yielded the same result. In practice, the required compensation can be conveniently included directly in the shaped input pulse, but in the strict context of parametric transfer, we would no longer be looking at getting the best replication of the shaped pump pulse but rather the best production of a certain target pulse.

If we perform the analysis on the b_p term, we see that from Eqn. 5.10, it is related to the mixed term $\Omega_s\Omega_i$, and so it cannot be factored out of the integration in Eqn. 5.9. Moreover, this also does not lead to a simple convolution relation similar to Eqn. 5.17, and would therefore significantly degrade the parametric transfer. It is also expected that, due to the mixed term, the required delay τ_{ps} to compensate $\delta\nu_{ps}$ is not equal to τ_c.

Figure 5.8 shows contour plot of the calculated transfer fidelity Z as a function of b_pL and $\delta b_{pi}L$, with $\delta\nu_{pi} = 0$, $\delta\nu_{ps}L = 1\,\text{ps}$, and $I_p^{(0)} = 10\,\text{kW/cm}^2$. The input peak intensity was such that signal amplification was low and the input pulse delay, τ_{ps}, was a variable so that the results plotted in Fig. 5.8 correspond to minimum Z for a given b_pL and $\delta b_{pi}L$ pair. In calculating the minimum Z, it was necessary to implement an optimization algorithm to locate the delay τ_{ps} which compensates $\delta\nu_{ps}$ and some of the GVD. The algorithm chosen was the Nelder-Mead algorithm [11].

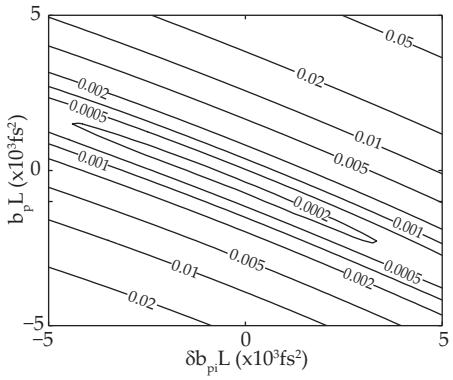

FIGURE 5.8: Contour plot of transfer fidelity Z as a function of b_pL and $\delta b_{pi}L$.

From the figure, it can be seen that the rate of change of Z with b_pL is higher than that with $\delta b_{pi}L$. Figure 5.8 also shows, that there exists a line of minimum Z, which does not

coincide with the origin, i.e. $(b_pL, \delta b_{pi}L) = (0, 0)$. Since the resolution of the transferred phase is limited by the convolution, introduction of group delay in the material by GVD may improve the transfer fidelity as the resolution limit is relaxed.

5.2.4 Parametric Transfer via Difference Frequency Generation in PPLN

In this section we consider the parametric transfer in a real material such that choice of pump, signal and idler wavelengths and their associated group velocities are constrained. In the condition of zero temporal walk-off between the pump and idler, the group velocity profile of the material must have a turning point which corresponds to zero GVD. The choice of material here is PPLN and Fig. 5.9 shows the group velocity and GVD of lithium niobate. From this figure, one can see that for a pump wavelength of $\sim$1 μm, the idler wavelength must be $\sim$3.5 μm in order to satisfy $\delta\nu_{pi} = 0$. Consequently, the phase matching condition derives that the signal wavelength must be $\sim$1.5 μm.

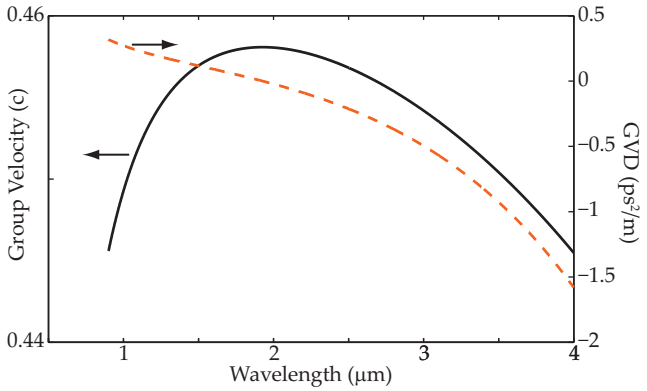

FIGURE 5.9: Group velocity (solid curve) and group velocity dispersion (GVD, dashed curve) of lithium niobate at a temperature of $T = 120\,^0$C as calculated from the Sellmeier equation [12].

In order to numerically model parametric transfer in PPLN, we included the dispersion parameters (GVM and GVD) of lithium niobate at a temperature of $T = 120\,^0$C calculated from the Sellmeier equation given in Ref. [12] into the numerical analysis. The nonlinear coupling coefficients are the same as the ones used in the previous section.

Figure 5.10 shows the numerical results of parametric transfer fidelity Z as a function of the idler carrier wavelength (λ_i) for four different pump carrier wavelengths ($\lambda_p = 0.95$, 1.00, 1.05, and 1.10 μm) in a 1 cm long crystal with input pump and signal peak intensities at $I_p^{(0)} = I_s^{(0)} = 5\,\mathrm{MW/cm^2}$, resulting in an idler peak intensity of $I_i^{(0)} \approx 1\,\mathrm{MW/cm^2}$. These power levels correspond to low signal amplification, and some pump depletion. Tuning of the idler wavelength was achieved by varying the input signal wavelength and under conditions of non-critical phase matching. In practice, this can be achieved by careful choice of PPLN poling period and/or temperature tuning. Values of $\delta\nu_{pi}L$ as a function of λ_i for different λ_p are also plotted in Fig. 5.10. Results of the parametric transfer are shown under the working conditions of no GVD and with GVD in which, for both cases, the temporal walk-off, $\delta\nu_{ps}$, and GVD are compensated for by optimisation of the relative delay, τ_{ps}, using the Nelder-Mead algorithm. The condition of GVD with pre-compensation of the group delay due to GVD is also considered, again with the use of the Nelder-Mead algorithm, finding both the optimum delay and GVD post-compensation required. Note that experimentally, a pre-compensating scheme would be used since the pulse shaper could be used to apply the required group delay to the pump pulse. Numerically it was found that both pre- and post-compensation yielded the same results, therefore a post-compensation scheme was used here since it was computationally less expensive.

The figure shows that in all cases, the optimum fidelity coincides with the condition of $\delta\nu_{pi} = 0$. In general, results without GVD yield a lower Z than the ones with GVD, while the results that use post-compensation fall in between. For different pump carrier wavelengths, the corresponding idler wavelength for minimum Z also changes accordingly since there is a shift under which the condition $\delta\nu_{pi} = 0$ is satisfied. As $\delta\nu_{pi}$ increases, Z also increases, so the individual curves in Fig. 5.10 describe the fidelity of the MIR PPLN source as it is tuned. If a tunable pump source is available, it is observed from the figure that a significant MIR wavelength range can be achieved without any change in the fidelity for $\delta\nu_{pi} = 0$ in the case of no GVD. However, in the cases with GVD, as λ_p becomes shorter, the transfer fidelity becomes worse due to an increase in b_p. This is supported by the fact that the post-compensation is less able to improve the transfer fidelity at shorter λ_p. A similar picture can be obtained for lower input

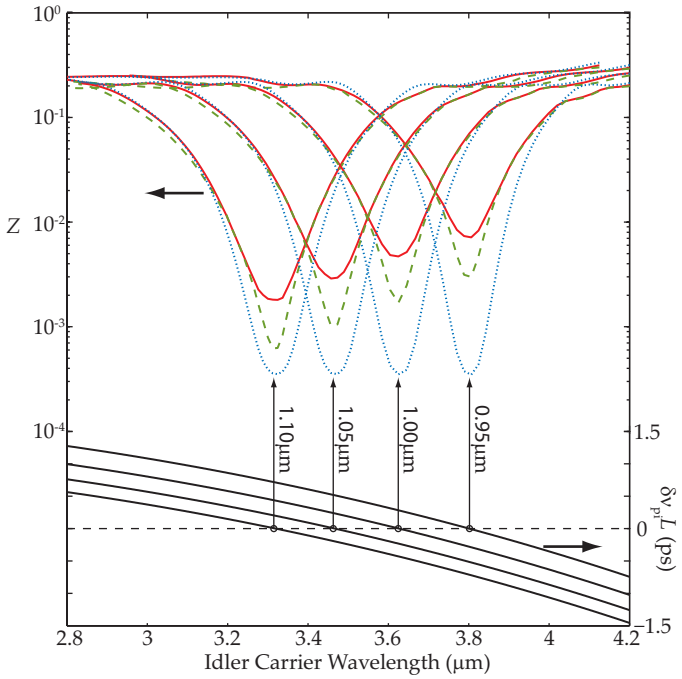

FIGURE 5.10: Parametric transfer fidelity Z (top) and temporal walk-off $\delta\nu_{pi}L$ (bottom) as a function of the idler carrier wavelength λ_i using different pump carrier wavelength λ_p, as indicated by the numbers, in a 1 cm long PPLN. The peak intensities for both input pump and signal pulses were 5 MW/cm^2. Parametric transfer fidelities for different cases are shown: with GVD (solid red curves), with GVD and post-compensation (dashed green curves), and without GVD (dotted blue curves).

peak intensities. Note that from Fig. 5.9, zero GVD would correspond to a wavelength of $\sim 1.7\,\mu$m, which is not a practical pump wavelength for many reasons including the fact that a DFG interaction under the condition $\delta\nu_{pi} = 0$ would not be possible.

Further improvements in tunability can be acquired by using shorter crystal lengths as the current crystal length of 10 mm in this numerical simulation is relatively long. Figure 5.11 shows the calculated transfer fidelity Z as a function of λ_i using $\lambda_p = 1.05\,\mu$m in three different lengths of PPLN ($L = 10, 5, 2.5$ mm). The peak intensities for both input pump and signal pulses were $I_p^{(0)} = I_s^{(0)} = 5$, 10, 20 MW/cm^2, respectively which produced similar output idler peak intensities of $I_i^{(0)} \approx 1$ MW/cm^2 for the different crystal lengths. Results including GVD, GVD with post-compensation, and not including GVD, are shown. When comparing the 10 and 5 mm crystals, the shorter crystal length improves the transfer fidelities, due to a reduction in the $\delta\nu_{ps}L$ and $\delta b_{pi}L$, and the post-compensation scheme always improves the results where GVD is included. However,

in the 2.5 mm long PPLN crystal, results that include GVD (with or without compensation) provide better transfer fidelities than the one that without GVD. As explained earlier in Section 5.2.3.3, in this particular example, the amount of chirp introduced in the material fortuitously improves the limited resolution resulting from the convolution. Inspection of the tunability of the DFG process for good transfer fidelity (i.e. $Z < 0.005$)

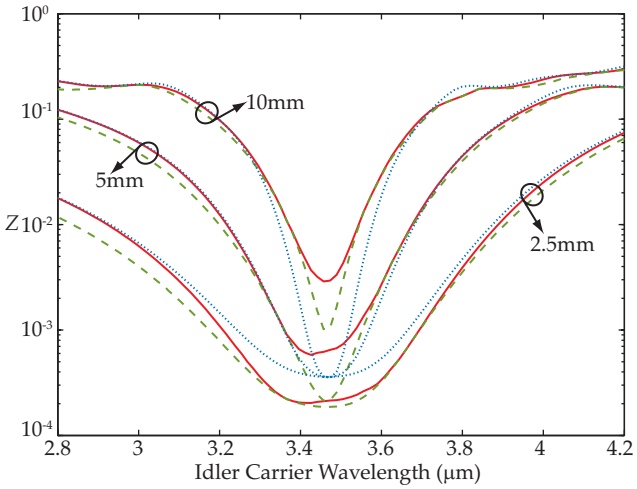

FIGURE 5.11: Parametric transfer fidelity Z (bottom) as a function of the idler carrier wavelength λ_i using a pump carrier wavelength $\lambda_p = 1.05\,\mu$m in three different lengths of PPLN ($L = 10, 5, 2.5$ mm). The peak intensities for both input pump and signal pulses were $I_p^{(0)} = I_s^{(0)} = 5$, 10, 20 MW/cm^2, respectively. Parametric transfer fidelities for different cases are shown: with GVD (solid red curves), with GVD and post-compensation (dashed green curves), and without GVD (dotted blue curves).

finds that the idler wavelength tunability improves from an idler range of approximately $\pm 0.03\,\mu$m to $\pm 0.4\,\mu$m when the crystal length is decreased from 10 mm to 2.5 mm.

5.2.5 Discussion of Parametric Transfer via Difference Frequency Generation

In this section, a comprehensive study of the effects that can affect parametric transfer from a NIR pump to a MIR idler via DFG have been addressed. The parametric transfer is fundamentally limited by the convolution through which the signal pulse effectively controls the resolution of transfer to the idler. Therefore, using a signal with a narrow bandwidth is imperative for good transfer fidelity.

Effects due to material dispersion have also been investigated. The temporal walk-off between pump and idler pulses restricts the amount of spectral bandwidth one can transfer, while the pump-signal temporal walk-off shifted their temporal overlap. Experimentally, this can be compensated for by using a delay line to introduce a temporal delay τ_c, for which good transfer can be achieved due to a symmetric walk-through.

The effects of process nonlinearity that are pump depletion and signal amplification have also been studied. Good transfer fidelity was found to be achieved at input pump intensities where significant pump depletion occurred before the onset of back-conversion. Signal amplification however, was found to degrade the parametric transfer, therefore limiting the idler intensities generated. Contributions of from other nonlinear effects in the material, such as self- and cross-phase modulation, were also considered but these were found to be negligible under the conditions of the calculations presented here.

Finally, with appropriate care, results of high fidelity transfer can be achieved within a large idler tunability of $\sim 1\mu$m with the idler wavelength centred on $3.44\,\mu$m and with the pump wavelength at $1.05\,\mu$m.

5.3 Parametric Transfer in an Optical Parametric Oscillator

In this section the previous numerical model for a DFG process is extended to a SPOPO and the same factors affecting transfer fidelity are examined. A schematic representation of the SPOPO used in the numerical model is shown in Fig. 5.12. The SPOPO consists of four mirrors arranged in a bowtie configuration where, from Fig. 5.12, mirrors M1 and M2 would in practice be curved mirrors to focus the pump and signal beams for near confocal focusing. In this numerical work, however, a plane wave approximation is assumed. The cavity resonates the signal pulse and an optical band-pass filter (OBPF) is placed after the nonlinear crystal to act as a spectral filter. The OBPF narrows the signal bandwidth to control the resolution of the parametric transfer.

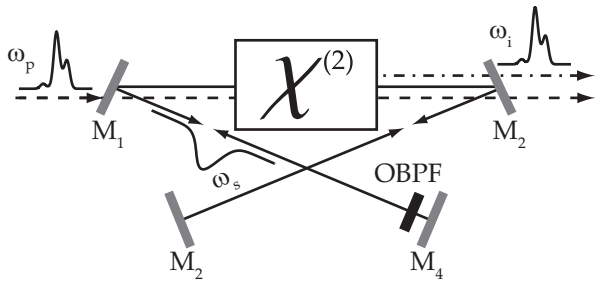

FIGURE 5.12: Illustration of indirect pulse shaping via parametric transfer in a SPOPO.

The equations used to model the system are the same as for the DFG model except that it is no longer a single pass system. We modelled the SPOPO illustrated in Fig. 5.12 by allowing the signal to pass through the crystal for many round-trips, after which, a stable signal would be achieved. For each round trip, the modified signal would be propagated back through the crystal but with a new pump and idler pulse, thereby simulating the effect of synchronous pumping. We describe the pump, signal and idler for each round trip using the following initial value boundary conditions (IVBC):

$$\begin{aligned} A_p^{(q)}(0,t) &= A_p(t), \\ A_s^{(q)}(0,t) &= \mathcal{M}\left[A_s^{(q-1)}(L,t)\right], \\ A_i^{(q)}(0,t) &= 0, \end{aligned} \tag{5.23}$$

where q is the number of round-trips, and $\mathcal{M}$ is an operator which describes the modified signal pulse from the previous round-trip and is given by,

$$\mathcal{M}\left[A_s(L,t)\right] = \sqrt{R}\mathcal{F}^{-1}\left\{G_F(\Omega_s)\exp[i\Omega_s(\delta\nu_{ps}L+\tau_{ps})]\hat{A}_s(L,\Omega_s)\right\}, \tag{5.24}$$

where τ_{ps} is the delay between the pump and signal pulses as defined earlier which, in this case, is due to a resonator mismatch. The symbol, $\mathcal{F}^{-1}$, denotes an inverse Fourier transform, R represents the total signal reflectivity of the cavity mirrors in the resonator, and $G_F(\Omega_s)$ is the mathematical representation of the OBPF in the resonator with a Gaussian intensity transmission having a FWHM δf_F, given by:

$$G_F(\Omega_s) = \exp\left[-4\ln 2\left(\frac{\Omega_s}{2\pi\delta f_F}\right)^2\right]. \tag{5.25}$$

Note that the above equation includes the fact that the resonating signal pulses make a double-pass through the OBPF in the resonator, and that its centre frequency always coincides with ω_s.

The pump pulse is the same SPM pulse as for the DFG model from Section 5.2. As with the previous simulation, we chose a a temporal FWHM of 1 ps, leading to a spectral FWHM of 4.44 THz, equivalent to ~ 16 nm for a carrier wavelength at $\sim 1\,\mu$m.

Equation 5.20 was iteratively solved with the IVBC given by Eqn. 5.23 using, as before, the symmetric split-step Fourier method with a fourth order Runge-Kutta integrator. For the first round trip, the signal starts as a transform-limited Gaussian pulse with the peak intensity significantly lower than that of the pump. A temporally broad pulse was used but it was found that the initial signal pulse only affected the time required to achieve a steady-state and did not affect the final result. The convergence to steady state was defined by a constant signal pulse energy (within $\pm 0.01\%$) over five consecutive iterations. It was assumed that the phase-matching condition was satisfied, i.e. $\Delta k_0 = 0$, and the nonlinear coupling coefficients used in the simulations, as before, assumed PPLN to be the nonlinear material.

5.3.1 Resonator Parameters and Process Nonlinearity

Numerical investigations began by considering the effect of the signal bandwidth and signal amplification on the parametric transfer. In the SPOPO, the signal bandwidth is controlled by the OBPF and the signal amplification is controlled by the overall reflectivity of the cavity. These two factors affecting transfer fidelity are therefore termed the resonator parameters.

In these numerical simulations, no chromatic dispersion was present in the nonlinear crystal, and unless stated otherwise, the OBPF's FWHM was chosen to be $\delta f_F = 0.5$ THz and the resonator reflectivity was $R = 95\%$.

The results of parametric transfer for narrowing signal bandwidth were found to be in agreement with the DFG numerical results. For the three different OBPFs used in the numerical modelling of the SPOPO, the signal pulse spectral rms widths at the crystal

entrance for $\delta f_F = 1.0, 0.5$, and $0.2\,\mathrm{THz}$ were respectively $0.075, 0.043$, and $0.019\,\mathrm{THz}$, while the temporal rms widths were $1.25, 2.45$, and $6.05\,\mathrm{ps}$, which remain almost constant for all pump depletion values. The transfer fidelity was found to improve with decreasing the FWHM of the OBPF from 1.0 to 0.2 THz, as shown in Fig. 5.13, but this improvement in fidelity is gained at the expense of an increase in the oscillation threshold. This is caused by an increased signal loss as the spectrum of the pulse is clipped by the OBPF.

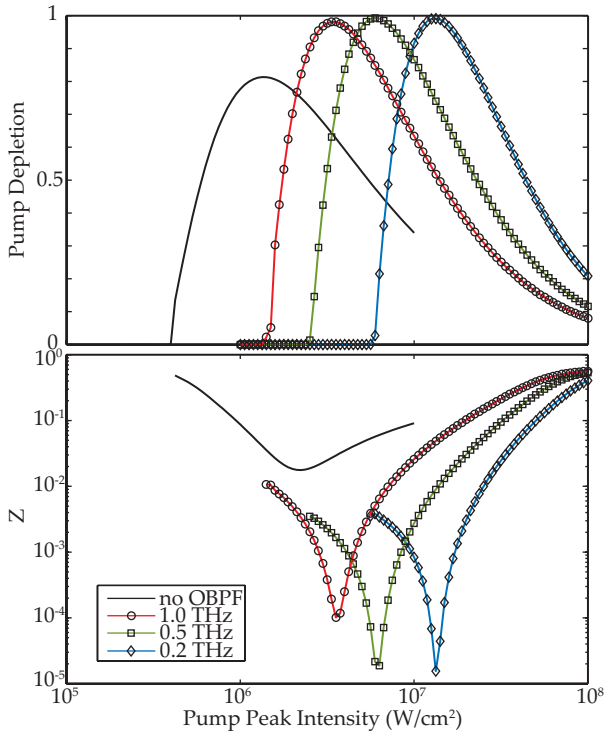

FIGURE 5.13: Pump depletion and transfer fidelity as functions of input pump peak intensity for SPOPO without and with OBPF having various FWHM δf_F, as indicated by the legend. In this calculation, no chromatic dispersion in the nonlinear crystal was present, while the resonator reflectivity was $R = 95\%$.

From Fig. 5.13 it can also be observed that the peak intensity that results in the best transfer fidelity, coincides with the maximum pump depletion and then the fidelity degrades as back-conversion occurs. This behaviour is in agreement with the DFG modelling from the previous section. However, without an OBPF, the signal pulse spectral width is not restricted, and consequently its temporal width is comparable to that of the pump pulse. Therefore, the pump does not deplete uniformly, causing the pump

depletion not to reach $\sim 100\%$ and the optimum transfer fidelity not to occur when the pump depletion reaches its maximum.

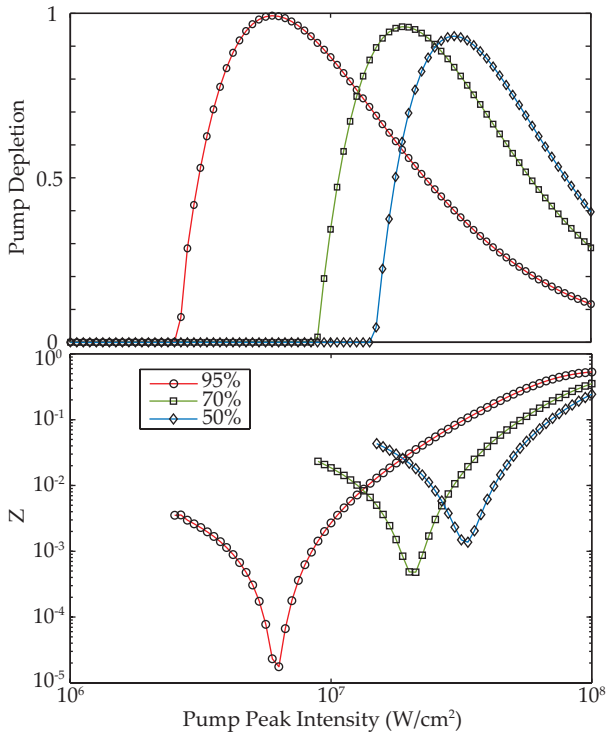

FIGURE 5.14: Pump depletion and transfer fidelity as functions of input pump peak intensity for different resonator reflectivities R, as indicated by the legend. In this calculation, no chromatic dispersion was present, while the OBPF's FWHM was $\delta f_F = 0.5\,\text{THz}$.

Next the effect of the resonator reflectivity is considered to simulate the effect of using M4 from Fig. 5.12 as a signal output coupler and hence acquiring more signal gain. Figure 5.14 shows the pump depletion and transfer fidelity as functions of pump peak intensity $I_p^{(0)}$, for resonator reflectivities $R = 95\%, 70\%$, and 50%. Although the OBPF FWHM was kept constant at $\delta f_F = 0.5\,\text{THz}$, the changing reflectivity resulted in different signal pulse widths. When a steady-state condition was reached, the signal pulse temporal rms widths for $R = 95\%, 70\%$, and 50% were $2.45, 1.05$, and $0.85\,\text{ps}$, while the spectral rms widths were $0.043, 0.082$, and $0.099\,\text{THz}$, respectively, for all pump depletion values. The results show that, in agreement with the DFG modelling results, the transfer fidelity degrades as the resonator reflectivity decreases. The signal amplification required to compensate for the higher loss contributes to the degradation of the transfer fidelity in two ways. Firstly, the parametric transfer degrades in a similar manner to the

effect on parametric transfer in a single-pass DFG process (see Eqn. 5.22), and secondly, decreasing the resonator reflectivity results in a spectrally broader signal pulse as can be seen in the spectral rms widths stated earlier. From the simple convolution relation, one can see that this also degrades the transfer. Note that again, in Fig. 5.14, we see that the optimum fidelity coincides with maximum pump depletion and degrades when back-conversion occurs.

The fact that parametric transfer degrades with resonator loss is convenient for MIR pulse shaping applications since only the idler wavelength is required. Moreover, having a low loss cavity yields a lower oscillation threshold. Finally, working under the condition of maximum pump depletion is also beneficial for efficient and stable operation as well as the fidelity of transfer.

5.3.2 Temporal Walk-off and Group Velocity Dispersion

As with the DFG model, the effects due to temporal walk-off and GVD are now considered. Beginning with the temporal walk-off between the pump and idler it is assumed that $\delta\nu_{ps} = 0$ whilst $\delta\nu_{pi}L = 0$, 0.1, and 0.2 ps. Figure 5.15 shows the effect of $\delta\nu_{pi}$ on the parametric transfer and pump depletion as functions of the input pump peak intensity. In a similar trend to the DFG model, one can identify that the parametric transfer significantly degrades as $\delta\nu_{pi}$ increases. As well as the onset of spectral clipping, this degradation is also due to the pump and idler not being fully temporally overlapped, resulting in an increase in oscillation threshold and a reduction in the maximum achievable pump depletion. However, in contrast to the previous results on resonator parameters, the optimum fidelity for $\delta\nu_{pi} \neq 0$ does not coincide with maximum pump depletion. This is due to a more complex interaction as a result of the temporal walk-off causing non-uniform depletion and back-conversion of the pump as it propagates through the crystal.

The effect of the pump and signal temporal walk-off with $\delta\nu_{pi} = 0$ is considered next. Figure 5.16 shows the results for $\delta\nu_{ps}L = 0$, -1, and -2 ps, plotting pump depletion, transfer fidelity, and temporal and spectral widths of the signal pulse as functions of the round-trip mismatch, τ_{ps}. The results show that as $\delta\nu_{ps}L$ increases, the fidelity improves

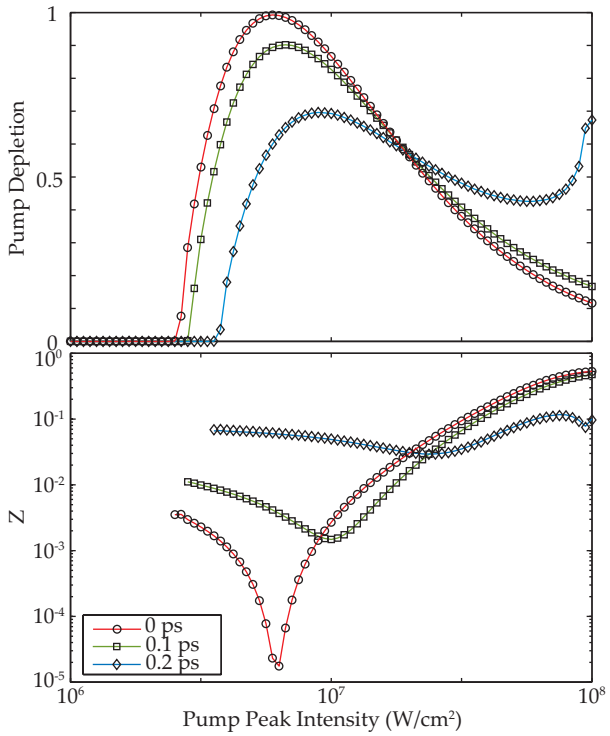

FIGURE 5.15: Pump depletion and transfer fidelity as functions of input pump peak intensity for temporal walk-off between the idler and pump pulses $|\delta\nu_{ip}L|$, as indicated by the legend, at zero round-trip mismatch ($\tau_{ps} = 0$). The resonator reflectivity was $R = 95\%$, the OBPF's FWHM was $\delta f_F = 0.5\,\text{THz}$, and there was no GVD or temporal walk-off between the pump and signal pulses.

and is therefore in agreement with the DFG model due to broadening of the effective signal pulse in Eqn. 5.19. However, the optimum round-trip mismatch is significantly less than the value of $\tau_{ps} = \delta\nu_{ps}L/2$ predicted by the DFG model.

Results examining the effects of the GVD due to the pump and that of the idler were in agreement with the DFG model showing that the transfer fidelity degrades significantly due to GVD. It is expected that compensation of the GVD effect by applying an optimum group delay to the pump (or idler) pulse, will result in an improvement in transfer fidelity, as was the case in the DFG model.

5.3.3 Discussion of Parametric Transfer in an Optical Parametric Oscillator

Following an in depth analysis of parametric transfer in DFG and a discussion of the results of the SPOPO model, we can identify the parameters affecting transfer and the

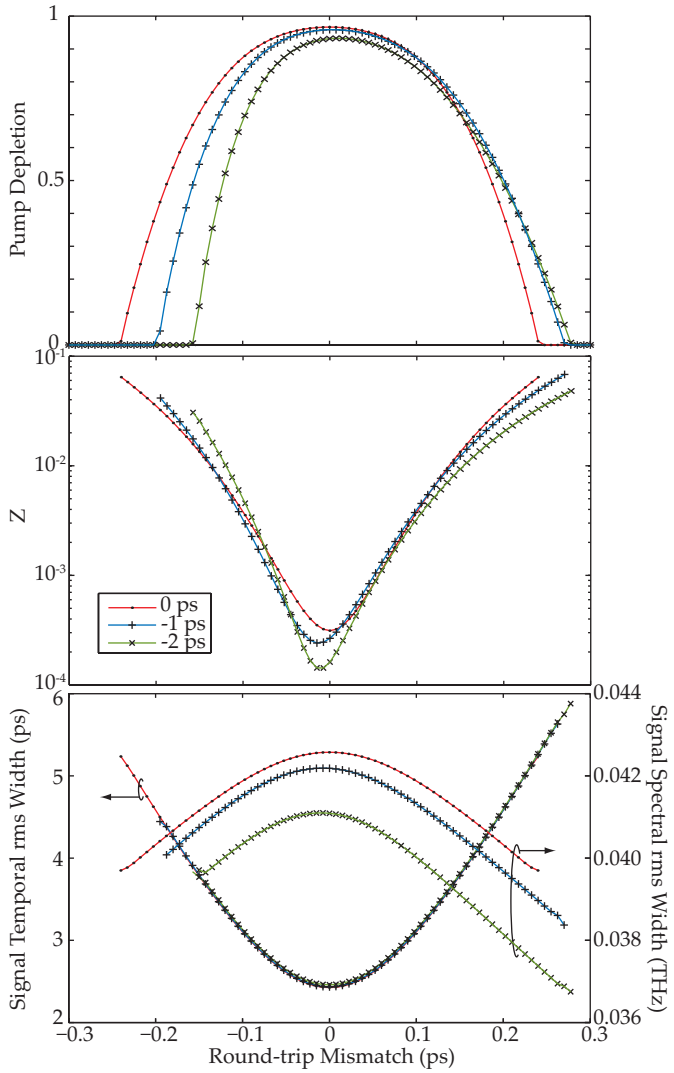

FIGURE 5.16: Pump depletion (top), transfer fidelity (middle), and temporal and spectral rms widths of the signal pulse at steady-state condition at the entrance of the nonlinear crystal (bottom) as functions of round-trip mismatch τ_{ps} for different temporal walk-offs between signal and pump pulses in the nonlinear crystal ($\delta\nu_{sp}L$), as indicated by the legend. The input pump peak intensity was $I_{p,0} = 5\,\mathrm{MW/cm^2}$, the resonator reflectivity was $R = 95\%$, the OBPF's FWHM was $\delta f_F = 0.5\,\mathrm{THz}$, and there were no GVD and temporal walk-off between the idler and pump pulses.

relative importance of these parameters.

The most important criteria for achieving good parametric transfer is dictated by the convolution relation and therefore requires the use an OBPF to narrow the signal spectrum. The bandwidth of the filtered signal ultimately determines the resolution of spectral transfer from the pump to the idler and improves the transfer fidelity values by at least several orders of magnitude in the results presented in this section.

The pump-idler temporal walk-off can also cause significant degradation of the fidelity and cannot be compensated for using external influences like the OPBP or detuning of the cavity length. Instead, one must ensure that $\delta\nu_{pi}L$ is small to minimise the effect of the walk-off. The effect of $\delta\nu_{pi}L$ in a PPLN SPOPO can be seen in Fig. 5.17 where results for idler wavelengths, at $\delta\nu_{pi}L = 0$ (red) and idler wavelength detunings of $\pm 0.05\,\mu m$ (blue and green), are shown for 3 different pump wavelengths $\lambda_p = 1.00, 1.05$, and $1.10\,\mu$m. For wavelength detunings of $\pm 0.05\,\mu m$ the results still yield satisfactory para-

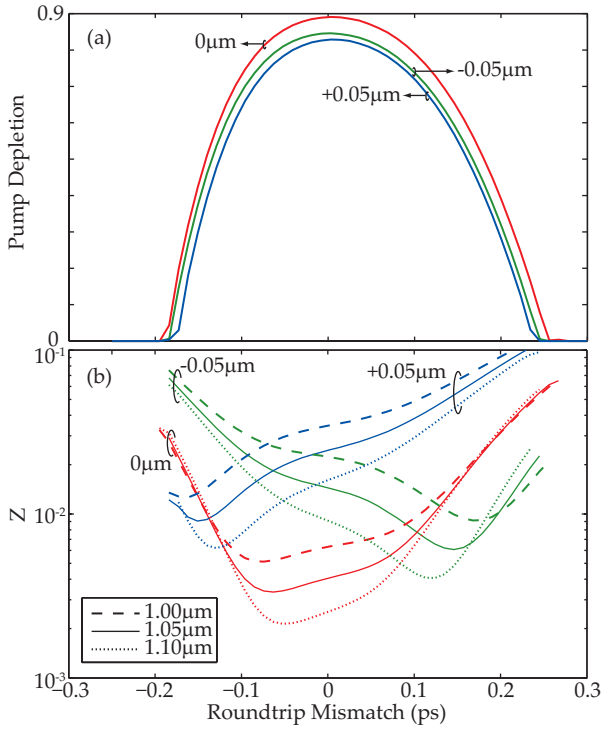

FIGURE 5.17: (a) Pump depletion and (b) transfer fidelity of a PPLN SPOPO as functions of round-trip mismatch for different idler wavelength shifts, as indicated by the numbers. The pump depletion curves (a) show the wavelength shift from $\lambda_i = 3.467\,\mu$m, while the transfer fidelity curves (b) are from $\lambda_i = 3.627, 3.467$, and $3.320\,\mu$m that satisfies $\delta\nu_{ip} = 0$ with input pump wavelengths $\lambda_p = 1.00, 1.05$, and $1.10\,\mu$m, respectively, as indicated by the legend. The PPLN length was $L = 10\,$mm, the resonator reflectivity was $R = 95\%$, and the OBPF's FWHM was $\delta f_F = 0.5\,$THz.

metric transfer although the optimum fidelity occurs at longer round-trip mismatches. From Fig. 5.17(a) one can see that the rate of change of pump depletion is significantly higher at the round-trip mismatch times for optimum fidelity with idler wavelength detuning and consequently, the parametric transfer is more sensitive to the round-trip mismatch compared with idler wavelengths that satisfy $\delta\nu_{pi}L = 0$. Finally, Fig. 5.17(b) shows that the parametric transfer improves with increasing pump wavelength due to

the decreasing GVD. This reflects the results from earlier in this chapter that have also shown that as well as minimising $\delta\nu_{pi}L$ it is also important to minimise the GVD for the pump and idler wavelengths. The GVD for the signal wavelength is not critical due to the large temporal width of the pulse. Note, however, that the DFG model shows that the effect of GVD is to introduce a group delay to the output pulse. Compensation of this group delay can be achieved by pre-compensation using, for example, a pulse shaper to apply the correct phase to the pump. The results in Fig. 5.17(b) also imply an idler wavelength tunability of less than $\pm 0.05\,\mu$m if good fidelity at $Z < 0.005$ is to be achieved.

Numerical results showed that the wavelength tunability could be improved with a shorter crystal length. Figure 5.18 shows the transfer fidelity as a function of round-trip mismatch for a crystal length of 2.5 mm for a pump wavelength of $1.05\,\mu$m. Results for different idler wavelength shifts from $\delta\nu_{ip} = 0$ show that an idler wavelength tunability of almost $\pm 0.3\,\mu$m can be achieved with this crystal length.

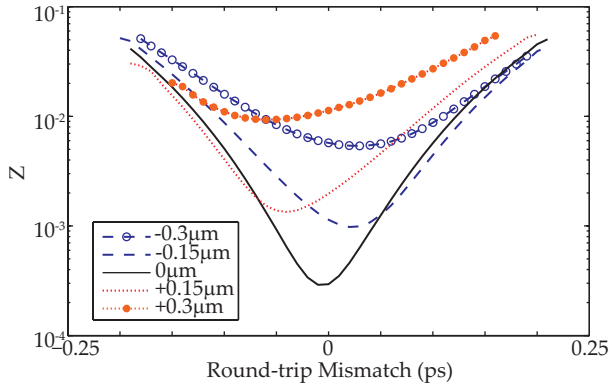

FIGURE 5.18: Transfer fidelity of a PPLN SPOPO as functions of round-trip mismatch for different idler wavelength shifts, as indicated by the legend, from $\lambda_i = 3.467\,\mu$m that satisfies $\delta\nu_{ip} = 0$ with input pump wavelength $\lambda_p = 1.05\,\mu$m. The PPLN length was $L = 2.5$ mm, the resonator reflectivity was $R = 95\%$, and the OBPF's FWHM was $\delta f = 0.5$ THz.

The GVM between the pump and signal also affects the transfer but it can easily be compensated for by introducing a round-trip mismatch which would be achieved by a detuning of the cavity length. When $\delta\nu_{ps}L > 0$, the signal can walk through the pump pulse and the numerical results found that by delaying the signal relative to the pump, i.e. negative round-trip mismatch, τ_{ps}, corresponding to a cavity length increase, the

transfer fidelity improved. For the case of DFG, the round-trip mismatch required is $\delta\nu_{ps}L/2$ for a symmetric walk-through but for the SPOPO, the mismatch required is significantly less due to the effect of the resonator.

It was also found that for good transfer fidelity, the signal amplification should ideally be kept to a minimum, a condition that is ideally suited for an SPOPO where only the idler wavelength is required. Finally, for $\delta\nu_{pi}L \simeq 0$ it was found that, in general, good fidelity could be achieved by increasing the pump peak intensity since this increases the pump depletion until back-conversion when the fidelity degrades.

In summary, the fidelity of transfer of the pump pulse shape to the idler has been numerically investigated, initially in a DFG process and then extending the analysis to a SPOPO. The individual effects of signal bandwidth, signal amplification, pump depletion, GVM, and GVD were considered and analyses of parametric transfer in PPLN in which the interplay between these effects could be studied were also provided. An experimental investigation into parametric transfer in a SPOPO will be presented in the next chapter.

References

[1] J. Prawiharjo, H. S. S. Hung, D. C. Hanna, and D. P. Shepherd, "Theoretical and numerical investigations of parametric transfer via difference-frequency generation for indirect mid-infrared pulse shaping," *J. Opt. Soc. Am. B* **24**(4), pp. 895–905, 2007.

[2] J. Prawiharjo, H. S. S. Hung, D. C. Hanna, and D. P. Shepherd, "Numerical investigations of parametric transfer in synchronously pumped optical parametric oscillators for indirect mid-infrared pulse shaping," *J. Opt. Soc. Am. B* **24**(9), pp. 2484–2493, 2007.

[3] H. S. Tan and W. S. Warren, "Mid infrared pulse shaping by optical parametric amplification and its application to optical free induction decay measurement," *Opt. Express* **11**(9), pp. 1021–1028, 2003.

[4] H. S. Tan, E. Schreiber, and W. S. Warren, "High-resolution indirect pulse shaping by parametric transfer," *Opt. Lett.* **27**(6), pp. 439–441, 2002.

[5] T. Witte, D. Zeidler, D. Proch, K. L. Kompa, and M. Motzkus, "Programmable amplitude- and phase-modulated femtosecond laser pulses in the mid-infrared," *Opt. Lett.* **27**(2), pp. 131–133, 2002.

[6] T. Witte, K. L. Kompa, and M. Motzkus, "Femtosecond pulse shaping in the mid infrared by difference-frequency mixing," *Applied Physics B: Lasers and Optics* **76**(4), pp. 467–471, 2003.

[7] G. Imeshev, M. A. Arbore, M. M. Fejer, A. Galvanauskas, M. Fermann, and D. Harter, "Ultrashort-pulse second-harmonic generation with longitudinally nonuniform quasi-phase-matching gratings: pulse compression and shaping," *J. Opt. Soc. Am. B* **17**(2), pp. 304–318, 2000.

[8] G. Imeshev, M. M. Fejer, A. Galvanauskas, and D. Harter, "Pulse shaping by difference-frequency mixing with quasi-phase-matching gratings," *J. Opt. Soc. Am. B* **18**(4), pp. 534–539, 2001.

[9] R. Trebino, K. W. DeLong, D. N. Fittinghoff, J. N. Sweetser, M. A. Krumbugel, B. A. Richman, and D. J. Kane, "Measuring ultrashort laser pulses in the time-frequency domain using frequency-resolved optical gating," *Rev. Sci. Instrum.* **68**(9), pp. 3277–3295, 1997.

[10] G. P. Agrawal, *Nonlinear Fiber Optics*, Academic Press, 3rd ed., 2001.

[11] J. C. Lagarias, J. A. Reeds, M. H. Wright, and P. E. Wright, "Convergence properties of the nelder-mead simplex method in low dimensions," *Siam Journal on Optimization* **9**(1), pp. 112–147, 1998.

[12] D. H. Jundt, "Temperature-dependent sellmeier equation for the index of refraction, n_e, in congruent lithium niobate," *Opt. Lett.* **22**(20), pp. 1553–1555, 1997.

Chapter 6

Experimental Investigation of Parametric Transfer in a Synchronously Pumped Optical Parametric Oscillator

6.1 Introduction

Following the numerical work for parametric transfer in a DFG and SPOPO process in the previous chapter, experimental work to verify the previously discussed parameters that affect parametric transfer in a SPOPO will be carried out in this chapter [1]. The effects of the signal bandwidth, resonator reflectivity, input pump power, cavity length tuning and pump-idler temporal walk-off will be investigated.

In Section 6.2 the experimental arrangement of the SPOPO and pulse characterization are described. Results for experiments investigating the factors affecting parametric transfer are shown in Section 6.3. Finally, we conclude in Section 6.4 with a discussion of the results.

The experimental work was carried out by myself whilst the code required to acquire and retrieve the sonogram data was written by Jerry Prawiharjo.

6.2 Experimental Arrangement

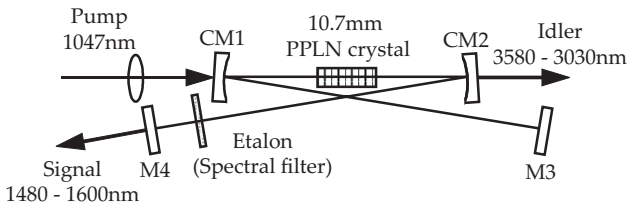

FIGURE 6.1: Schematic arrangement of the SPOPO setup.

A schematic representation of the SPOPO setup is shown in Fig. 6.1. The SPOPO comprises a resonator of four mirrors arranged in a bow-tie configuration, a PPLN crystal as the nonlinear medium, and an etalon to act as a spectral filter for the signal pulse. The mirrors are highly reflecting at $\sim 1200 - 2000$ nm, though a small amount of the signal is detected through M4 for SPOPO monitoring purposes. Two curved mirrors (CM1, CM2) are used to achieve a near-confocal focusing condition for the resonating signal pulse over the crystal length for optimum gain. The overall resonator length is set such that the signal round-trip time is comparable to the pump repetition period. This SPOPO design allows for simple alignment as synchronism can be easily achieved if M4 is mounted on a translation stage such that the movement is parallel to the beam. Moreover, tuning of the cavity length is required for the work presented in this chapter.

The continuous pump pulse train was generated by the Nd:YLF laser/amplifier system described earlier in Chapter 4, which was then spectrally broadened via SPM in a polarization-maintaining single-mode fibre. This delivers a train of pulses into the SPOPO at a repetition rate of 120 MHz, each with a $\sim$4 ps pulse width at a central wavelength of 1047 nm and a spectral FWHM of ~ 3.5 nm (958 GHz), with an average power of up to 1.15 W. It should be noted that the operation of this system varied slightly from day to day, resulting in a small variation of the spectral intensity profile in the different experiments.

The pump beam was focussed into the SPOPO with a 160 mm focal length lens, achieving an embedded fundamental Gaussian mode spot size of $\sim 30\,\mu$m. The measured M^2 of the pump beam was 1.1 in both the horizontal and vertical axes.

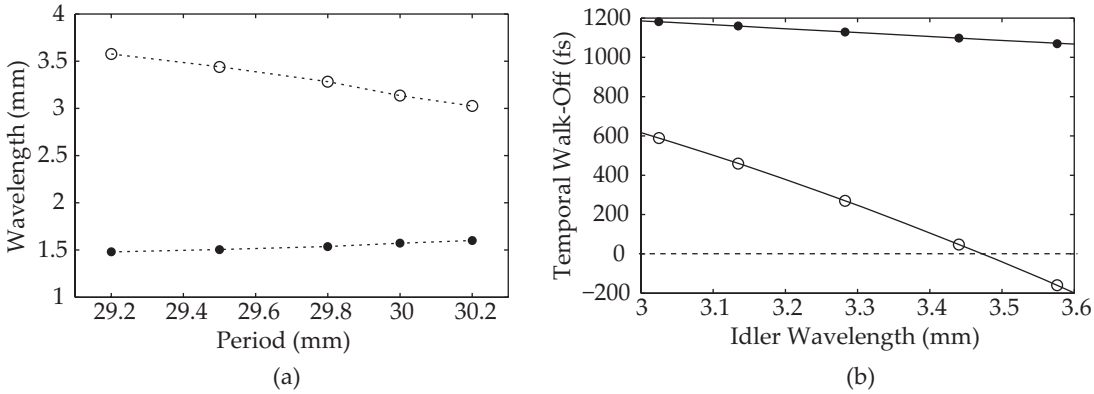

FIGURE 6.2: (a) The SPOPO signal (solid circles) and idler (open circles) wavelengths corresponding to the 5 different poling periods used, (b) pump-idler temporal walk-off (open circles) and pump-signal temporal walk-off (solid circles) as a function of the idler wavelength for operation at 110°C. The data points correspond to the discrete idler wavelengths from the poling periods available.

The 10.7 mm long PPLN crystal was operated at a fixed temperature of 110°C and had five different poling periods ranging from 29.2 μm to 30.2 μm to allow signal wavelengths between 1480 nm and 1600 nm to be obtained, corresponding to an idler wavelength range of 3580 nm to 3030 nm. These parameters are summarized in Fig. 6.2(a). The Sellmeier equation [2] was used to estimate the group velocity and its dispersion parameter (GVD) for the interacting pulses in lithium niobate. The calculated temporal walk-off between the pump and idler pulses and that between the pump and signal pulses for the wavelengths used in our experiment are given in Fig. 6.2(b). It can be seen that minimum pump-idler temporal walk-off occurs at signal and idler wavelengths of 1505 and 3440 nm, respectively. For the pump pulse parameters used here, it was calculated that the effect of the GDD in the lithium niobate could be neglected.

Spectral intensity measurements were acquired using an OSA with a resolution of 0.1 nm for the pump and signal wavelengths. The idler was measured using a monochromator (Bentham M300) and a nitrogen cooled InSb detector with a resolution of ~ 0.4 nm.

Complete characterization of the pump and idler pulses was achieved using the cross-correlation sonogram technique [3], schematically depicted in Fig. 6.3. This same arrangement was described fully in Section 3.3. The setup consists of a temporal delay

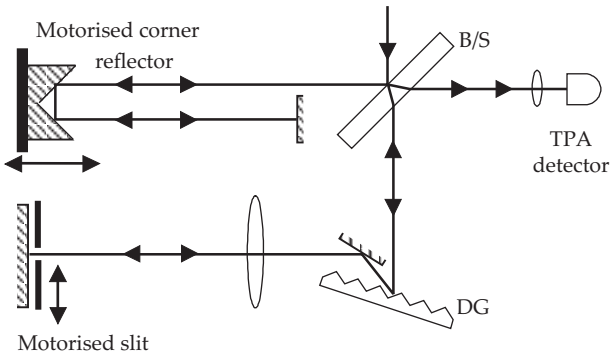

FIGURE 6.3: Schematic arrangement of the cross-correlation sonogram setup.

arm and a spectral gating arm arranged in a zero dispersion configuration. TPA cross-correlations between the temporally delayed and spectrally filtered pulses were taken at discrete frequencies to build sonogram traces, from which the spectral phase and amplitude of the input pulse were retrieved with an iterative deconvolution algorithm. Verification of the sonogram retrieval was achieved by comparison with measured spectral intensity and autocorrelation data where the autocorrelations were measured using the sonogram setups with open slits. A full sonogram trace made of fifty discrete frequencies was acquired in less than four minutes. Characterization of the pump and idler pulses used similar setups but with one of the major differences being the use of different detectors, a GaAsP detector for the NIR and an extended InGaAs detector for the MIR. In both cases, the spectral gating arm employed a slit of width one-tenth of the total spectral width. Furthermore, a phase-sensitive detection scheme using a lock-in amplifier was employed to improve the sensitivity of the setup. A measured and retrieved sonogram trace together with the retrieved spectral phase and amplitude, and the autocorrelation of a typical input pump pulse are shown in Fig. 6.4.

6.3 Results

In this section, investigations on the effects of various SPOPO parameters on the parametric transfer are presented, covering the effect of parameters such as etalon thickness, input pump power and resonator reflectivity. In addition, the effects of chromatic dispersion, specifically the temporal walk-off between the interacting pulses, are investigated.

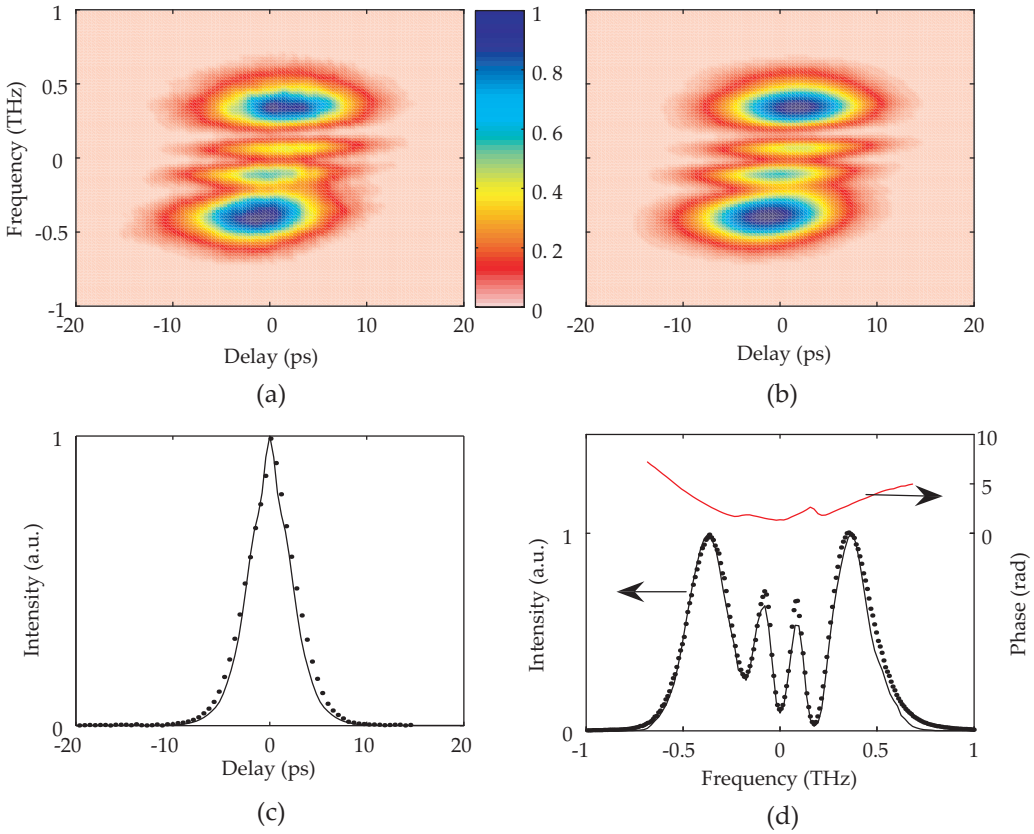

FIGURE 6.4: Sonogram data of the input pump pulse: (a) measured sonogram, (b) retrieved sonogram, (c) measured (circles) and retrieved (solid curve) autocorrelation traces and (d) measured (circles) and retrieved (solid curve) spectra with the retrieved spectral phase.

In analysing the transfer fidelity, comparisons of the autocorrelations, spectral intensities, and sonograms of the pump and idler were made. However, later results will mainly show the comparison between the pump and idler spectra since, for many of the results, it was found that the autocorrelations and spectral phases showed similar profiles, and that much of the change was in the frequency domain. A quantitative measure of the fidelity was therefore chosen, based on spectral intensity via the following overlap relation:

$$Z_S = 1 - \frac{\int \left|\widetilde{E}_p(\Omega)\right|^2 \left|\widetilde{E}_i(\Omega)\right|^2 d\Omega}{\left[\int \left|\widetilde{E}_p(\Omega)\right|^4 d\Omega \int \left|\widetilde{E}_i(\Omega)\right|^4 d\Omega\right]^{1/2}}, \tag{6.1}$$

where Ω is the frequency detuning and $\left|\widetilde{E}_{p,i}(\Omega)\right|^2$ is the spectral intensity of the pump or idler, as denoted by the subscripts p and i, respectively. This equation is analogous

to the expression for Z given in Eqn. 5.7, comparing the overlap of the pump and idler polarisation gate spectrograms. As with Z, the spectral transfer fidelity Z_S, ranges between zero and unity, where zero corresponds to perfect overlap and unity indicates no overlap. Note that the spectral intensity of the pump varied slightly from day to day. As a result, while comparison of Z_S values for the data set of one day's experiment prove a reliable indicator of the trend of fidelity, this does not extend to comparisons between data sets from experiments taken on separate occasions.

From the numerical investigations [4] in Chapter 5, the parameters leading to a high fidelity parametric transfer were identified, such as, placing an optical band-pass filter in the resonator, working at high pump depletion and low signal amplification, tuning the cavity length to compensate for the pump-signal temporal walk-off, and selecting the appropriate crystal length and/or idler wavelength to minimise pump-idler temporal walk-off. These requirements were satified by providing the cavity with an etalon whilst maintaining a low loss cavity by using mirrors that are highly reflecting at the signal wavelengths, working with a pump power at three times above threshold to achieve significant pump depletion whilst avoiding the back-conversion regime, and choosing the idler wavelength to be 3440 nm. Subsequent investigations were based on altering individual parameters around this operating condition.

6.3.1 Resonator Parameters and Process Nonlinearity

Operating the SPOPO using the standard configuration described in the previous section, the effect of the etalon on the signal bandwidth and on the transfer fidelity is investigated first. Without an etalon in the cavity, the signal bandwidth at 1505 nm was measured to be 1.3 nm (172 GHz), and the threshold was ∼100 mW average power. After placing an etalon in the resonator, an increase in threshold was observed due to the losses induced by the etalon. Two etalons of different thicknesses were used, resulting in signal bandwidths of 0.5 and 0.8 nm (66 and 106 GHz), and both with similar thresholds at 180mW. The etalon angle was adjusted to ensure that the centre wavelength of the resonating signal pulse was the same in all cases. In addition, all results were taken operating at three times above threshold.

The numerical investigations suggested that signal narrowing improves the resolution of transfer. In order to aid the qualitative assessment of transfer, a small adjustment of the cavity length was made to symmetrize the spectral transfer such that the two main idler spectral peaks were of the same height, as is the case for the pump spectrum (see Fig. 6.4). As a result of the bandwidth narrowing, the signal pulse is lengthened such that the SPOPO is stable over a wider range of cavity lengths. Therefore, such small detunings do not affect the resolution of transfer investigated here. Figure 6.5 shows the retrieved idler sonogram data for signal bandwidths of 1.3, 0.8, and 0.5 nm, corresponding to $Z_S = 0.069, 0.020$, and 0.012, respectively. These results clearly show a significant improvement in fidelity of transfer when an etalon is placed within the resonator. Moreover, further narrowing of the signal bandwidth results in a better transfer of the two central peaks of the spectrum, a consequence of the convolution relation. One can therefore confirm from these results that the signal bandwidth determines the resolution of transfer.

We next consider the effect of the pump depletion on the transfer fidelity. According to the numerical investigations, higher pump depletion without going to the back-conversion regime results in an improvement of the transfer fidelity, except in the presence of GDD. The improvement of transfer fidelity with pump depletion is due to an effective temporal broadening of the signal pulse relative to the pump when considering a single pass DFG process. The experimental SPOPO results were found to be in agreement with these numerical predictions. Figure 6.6 shows the idler spectra for pump power ranging from two to six times above the threshold of 180 mW. It can be easily seen that, in addition to the variation in the symmetry of the idler spectra, the transfer resolution improves with increasing input power. The corresponding spectral transfer fidelity is plotted in Fig. 6.7(b) showing an optimum at an operation of around four times above threshold. This point roughly coincides with the maximum pump depletion shown in Fig. 6.7(a), which is in agreement with the numerical investigations for negligible GDD.

The final resonator parameter that was investigated was the resonator loss by replacing mirror M4 from Fig. 6.1 with mirrors of different signal reflectivities. The numerical

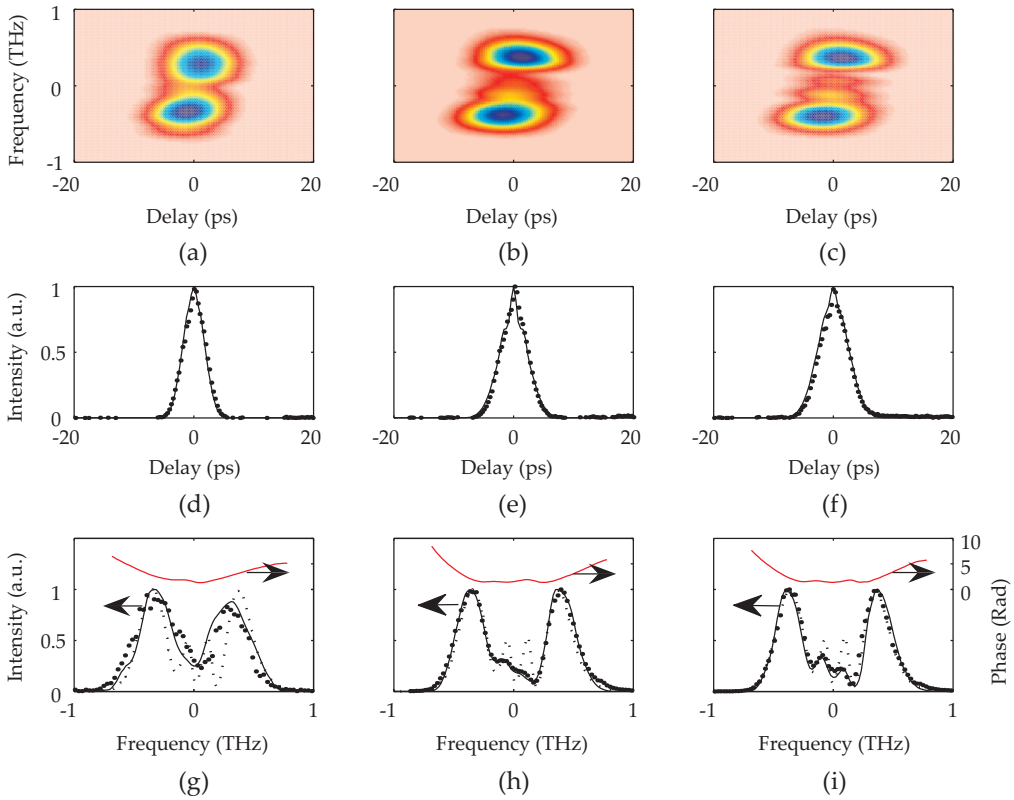

FIGURE 6.5: Idler sonogram data for signal bandwidths of 1.3nm (first column), 0.8nm (second column) and 0.5nm (third column). (a)-(c) Retrieved sonograms, (d)-(f) measured (circles) and retrieved (solid curve) autocorrelations and (g)-(i) measured (circles) and retrieved (solid curve) spectra with the retrieved spectral phases (solid red curve) and measured pump spectrum (dotted curve) for comparison.

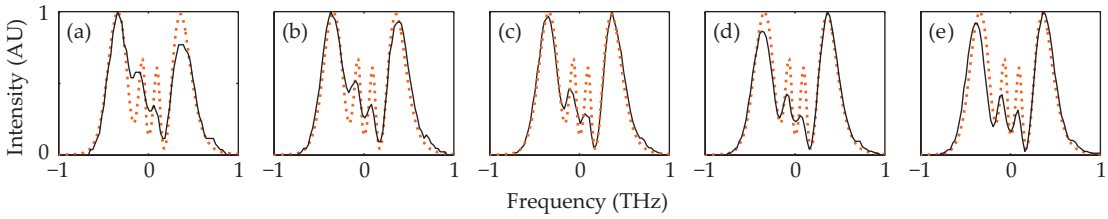

FIGURE 6.6: Measured pump (dashed) and idler spectra (solid) for increasing input pump power at (a) 2×, (b) 3×, (c) 4×, (d) 5× and (e) 6× above oscillation threshold.

investigations found that increasing the resonator loss and hence increasing the required signal gain worsens the transfer fidelity. Moreover, it was observed both theoretically (Fig. 5.14) and experimentally that a high resonator loss reduced the effect of the etalon as the signal bandwidth was broader at steady state. The SPOPO was operated using the standard configuration at two-and-a-half times above the threshold in this investigation, due to the maximum available pump power. The resulting idler spectra for M4 reflectivities of 65%, 85% and 100%, corresponding to $Z_S = 0.040, 0.017$ and 0.014,

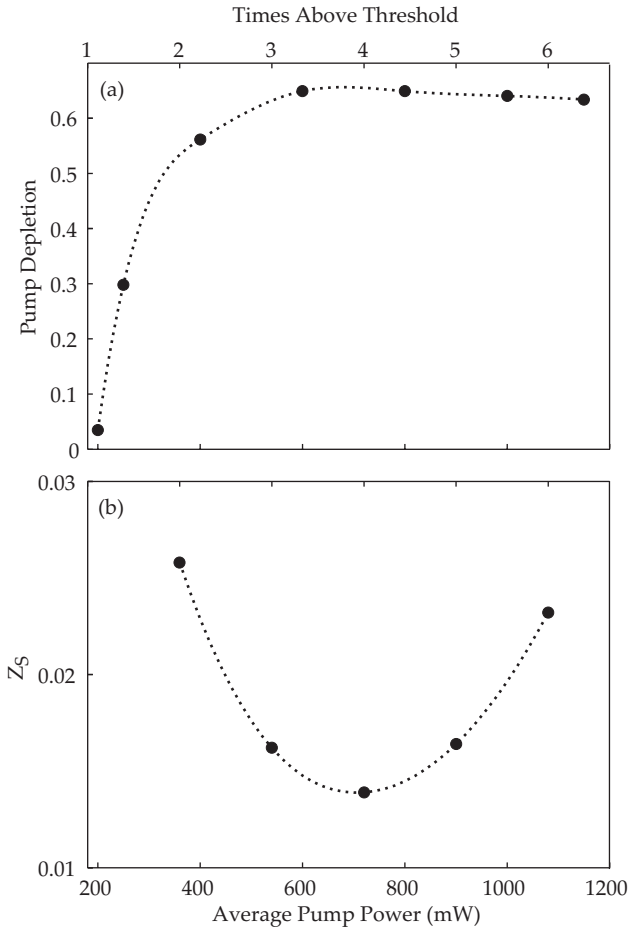

FIGURE 6.7: (a) Pump depletion, and (b) spectral transfer fidelity as functions of the average input pump power. The points represent data and the lines are a guide for the eye.

respectively, are shown in Fig. 6.8. It can be clearly observed that the fidelity improves with increasing M4 reflectivity, in agreement with the numerical investigations. The resolution of the central peaks also improves due to an associated narrowing of the signal spectrum but, unlike the results for increasing pump power, the overall symmetry of the spectra remain unchanged.

Note that the experimental conditions for Fig. 6.8(c) are similar to those in Fig. 6.6(a)-(b) where operation is at 2 and 3 times above threshold with M4 reflectivity of 100%. By observation, particularly of the resolution of transfer, Fig. 6.8(c) taken at 2.5 times above threshold shows an idler spectral intensity profile similar to Fig. 6.6(a)-(b). However, Fig. 6.7(b) shows that the expected spectral transfer Z_S for operation at 2.5 times above threshold is higher than $Z_S = 0.014$ calculated from Fig. 6.8(c). This discrepancy is due to the one of the centre peaks of the pump spectrum being higher in Fig. 6.6 than in

Fig. 6.8 where the former case would require a higher resolution of transfer for a lower value of Z_S. This therefore highlights the earlier comment about the use of Z_S as a relative value only within data sets.

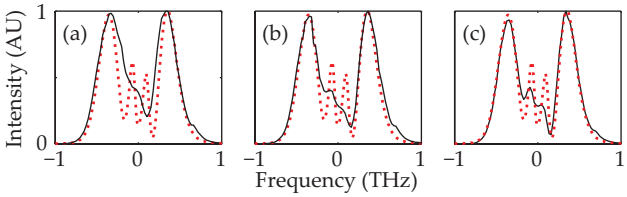

FIGURE 6.8: Measured idler spectra (solid) and input pump spectrum (dashed) for M4 reflectivites of (a) 65%, (b) 85% and (c) 100%.

6.3.2 Chromatic Dispersion

Having investigated the effects of the resonator parameters, the effects of the PPLN chromatic dispersion on the parametric transfer will now be shown. More specifically, the effect of the temporal walk-off between the interacting pulses will be investigated, since the effect of the GDD is negligible for our experimental configuration.

We start by investigating the effect of the pump-signal temporal walk-off. For the combination of wavelengths used here, the signal group velocity is greater than the pump group velocity, causing the signal to walk through the pump in the PPLN and thus distorting the parametric transfer. In the earlier numerical investigation, it was established that this effect can be compensated for by adjusting the cavity length in such a way that the signal arrives at the crystal after the pump pulse. Note that, in this chapter, zero round-trip mismatch, τ'_{ps} is defined to correspond to the resonator length at which minimum threshold is achieved. This is different from the definition of τ_{ps} in Chapter 5 that corresponds to the length for which the pump and signal pulse peaks enter the crystal at the same time. Hence, the two definitions are related by some temporal offset which has not been experimentally determined.

For this investigation, the standard SPOPO configuration was used, where the pump-idler temporal walk-off was ∼48 fs, and consequently the pump-signal temporal walk-off was ∼1 ps. An etalon was used to restrict the signal bandwidth to ∼100 GHz at a centre wavelength of 1505 nm. Figure 6.9 shows the measured idler spectra for cavity length

detunings of $\pm 80\,\mu$m, $\pm 40\,\mu$m and $0\,\mu$m, corresponding to round-trip mismatches, τ'_{ps} of ∓ 267 fs, ∓ 133 fs and 0 fs, respectively. Note that a negative round-trip mismatch corresponds to the signal arriving at the crystal at a later time than the pump. This is the same sign convention as in Chapter 5. An increase in cavity length detuning causes

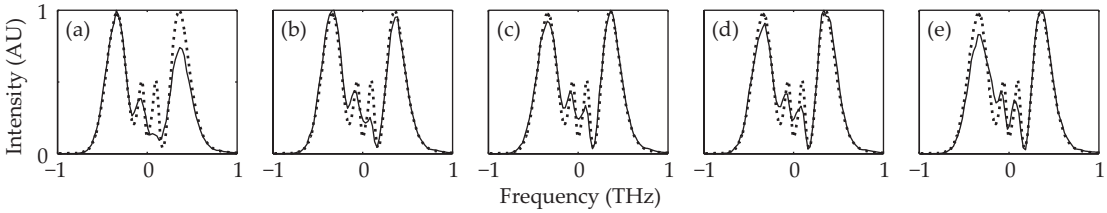

FIGURE 6.9: Measured idler spectra (solid) and input pump spectrum (dashed) for increasing cavity length corresponding to round-trip mismatches of (a) +267fs, (b) +133fs, (c) 0fs, (d) -133fs and (e) -267fs in an arrangement where the pump-idler temporal walk-off is 48fs.

a delay in the signal pulse arrival at the PPLN entrance, causing the higher frequency spectral peak of the pump pulse, that corresponds to the trailing edge, to be transferred more efficiently. Note that at zero round-trip mismatch, the heights of the two larger spectral peaks are not quite equal as they are in the pump. Symmetric transfer to the idler occurs between a round-trip mismatch of zero and +133 fs, although this seems to be coupled with a slight degradation in fidelity of the centre peaks of the spectrum. Conversely, decreasing the cavity length seems to improve the resolution of the central peaks but compromises the symmetry of the spectral transfer. Fig. 6.13(b) shows the relative trend of spectral transfer fidelity Z_S calculated from the data in Fig. 6.9 and will be discussed in more detail later.

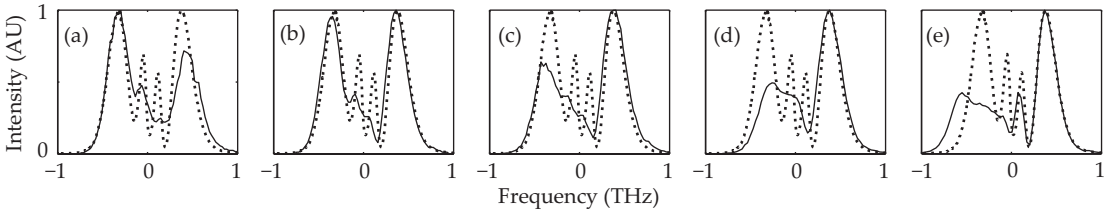

FIGURE 6.10: Measured idler spectra (solid) and input pump spectrum (dashed) for poling periods (a) 29.2μm, (b) 29.5μm, (c) 29.8μm, (d) 30.0μm and (e) 30.2μm showing variation of spectral fidelity as pump-idler temporal walk-off varies.

Having investigated the pump-signal temporal walk-off, we now investigate the effect of the pump-idler temporal walk-off. In this investigation, the pump-idler temporal walk-off was changed by varying the idler wavelength, which was achieved by using

different QPM grating periods in our PPLN crystal. As in previous investigations, the SPOPO was operated at three times above threshold and an etalon was used to narrow the signal spectral FWHM to ∼100 GHz. Figure 6.10 shows the idler spectra for five different PPLN poling periods, whose transfer fidelity Z_S is plotted in Fig. 6.11. It can be easily seen that the best fidelity is achieved at minimum pump-idler temporal walk-off where the working idler wavelength is 3440 nm. As the pump-idler temporal walk-off becomes more positive, as shown in Fig. 6.10(c)-(e), the transfer fidelity of the lower frequency peak worsens. Similarly, as the pump-idler temporal walk-off becomes more negative, the transfer of the higher frequency peak is degraded, as shown Fig. 6.10(a).

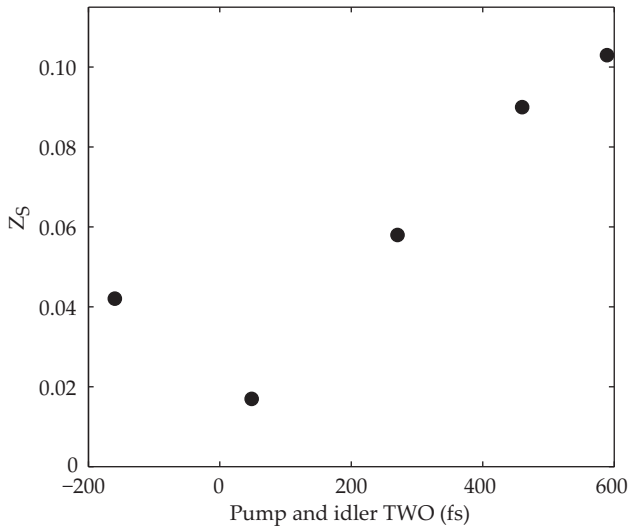

FIGURE 6.11: Spectral fidelity z as a function of pump-idler temporal walk-off.

It is important to mention that the degradation of the transfer fidelity indicated by the difference in the height of the two main spectral peaks cannot always be rectified by tuning the cavity length. When the SPOPO had a signal central wavelength of 1600 nm, the cavity length was varied by as much as ±120 μm, corresponding to a total round-trip mismatch of ∓400 fs, and obtained various idler spectra as shown in Fig. 6.12. It can be seen from this that, in contrast to Fig. 6.9, as the cavity length is increased, the lower frequency peak becomes higher than the higher frequency peak. This is due to the higher frequency peak decreasing in energy rather than an increase in the lower frequency peak since the signal pulse is delayed to the extent that the interaction with the pump is reduced. As a result of the large pump-idler temporal walk-off and non-uniform pump depletion, the lower frequency leading peak is generally not transferred well.

The spectral fidelity Z_S for our SPOPO working at two different wavelengths at various cavity length offsets is compared in Fig. 6.13. For both cases, it can be observed that minimum Z_S coincides with near maximum pump depletion. For $\lambda_s = 1600\,\text{nm}$, the maximum achievable pump depletion is lower than for $\lambda_s = 1505\,\text{nm}$ and the rate of change of depletion with cavity length detuning is faster. However, despite the relatively small change in the pump depletion behaviour, the spectral transfer fidelity is significantly worsened by the increase in pump-idler temporal walk-off. If we compare the results of Fig. 6.13(b) with Fig. 5.17(b), one can see that in the numerical results, a reduction of the idler wavelength from $\delta\nu_{pi} = 0$ results in the optimum fidelity occurring at more positive τ'_{ps} than at $\delta\nu_{pi} = 0$. In contrast, Fig. 6.13(b) shows the minimum occurring at more negative round-trip mismatch. However, note that the round-trip mismatch τ'_{ps} (or cavity length detuning) for the $\lambda_s = 1505\,\text{nm}$ and $\lambda_s = 1600\,\text{nm}$ data sets cannot be directly compared as the zero round-trip mismatch conditions do not necessarily correspond to the same cavity length as would be the case in the numerical results. Instead, it is more valuable to examine the rate of change of Z_S with τ'_{ps}. In the $\lambda_s = 1600\,\text{nm}$ data for Fig. 6.13(b), the rate of change of Z_S with τ'_{ps} is faster for $\tau'_{ps} > \tau'_m$ than $\tau'_{ps} < \tau'_m$, where τ'_m is the round-trip mismatch corresponding to minimum Z_S. Also, inspection of the same data set but for pump depletion in Fig. 6.13(a), shows that that the rate of change of pump depletion with τ'_{ps} is slower for $\tau'_{ps} > \tau'_m$ than $\tau'_{ps} < \tau'_m$. Comparison of these trends with the equivalent numerical results in Fig. 5.17 show that the experimental results are in good agreement.

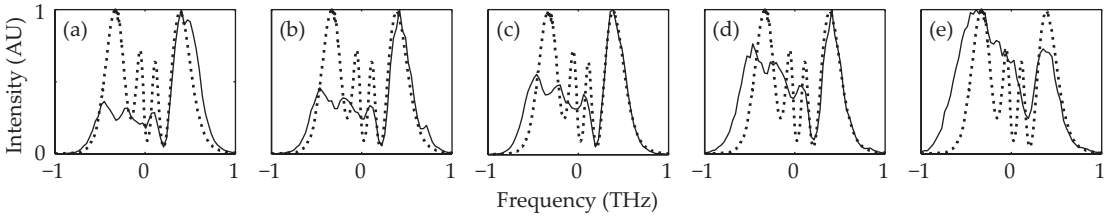

FIGURE 6.12: Measured idler spectra (solid) and input pump spectrum (dashed) for increasing cavity length corresponding to round-trip mismatches of (a) +400fs, (b) +133fs, (c) 0um, (d) -266fs and (e) -400fs in an arrangement where the pump-idler temporal walk-off is 589fs.

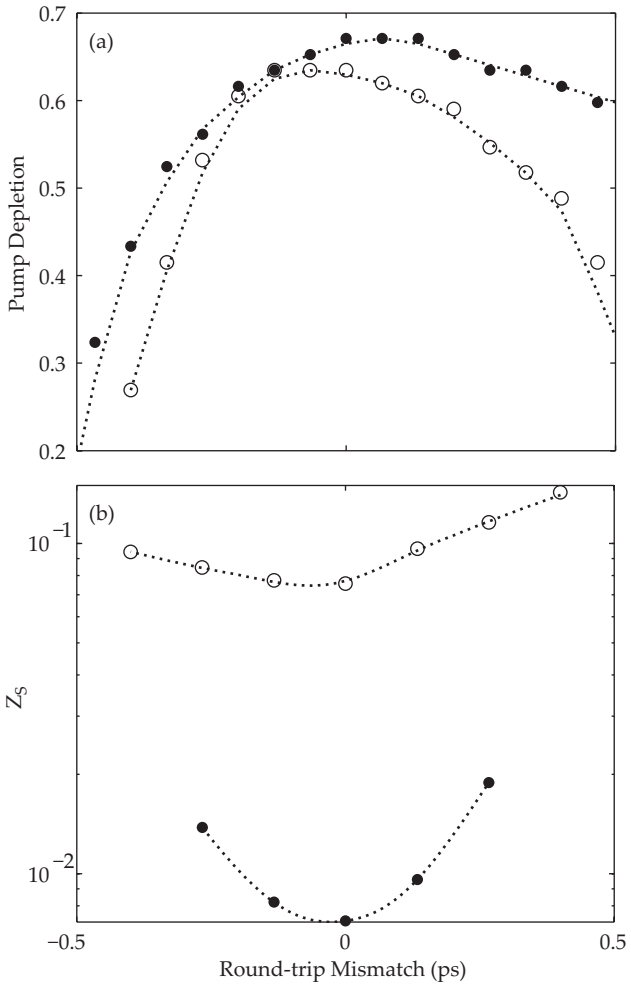

FIGURE 6.13: (a) Pump depletion and (b) fidelity as functions of cavity length for SPOPO arrangements where λ_s=1505 nm (solid circles) and λ_s=1600 nm (open circles). The points represent data and the lines are a guide for the eye.

6.3.3 High fidelity transfer

Finally, based on the results of the investigation thus far, the SPOPO was operated for high fidelity transfer by placing an etalon in the cavity to reduce the signal spectral FWHM to ∼80 GHz, choosing a PPLN grating with minimal pump-idler temporal walk-off working at $\lambda_i = 3440$ nm, compensating the pump-signal temporal walk-off by tuning the cavity length, using a low loss resonator and operating at four times above threshold to achieve a significant pump depletion. Figure 6.14(b) shows the retrieved idler sonogram trace obtained under these conditions looking almost identical to the retrieved pump sonogram trace in Fig. 6.14(a). Closer inspection of the pulses can be seen in Fig. 6.14(d) where comparison of the pump and idler spectra and phase show that they are in good agreement except for a small discrepancy in the middle peaks.

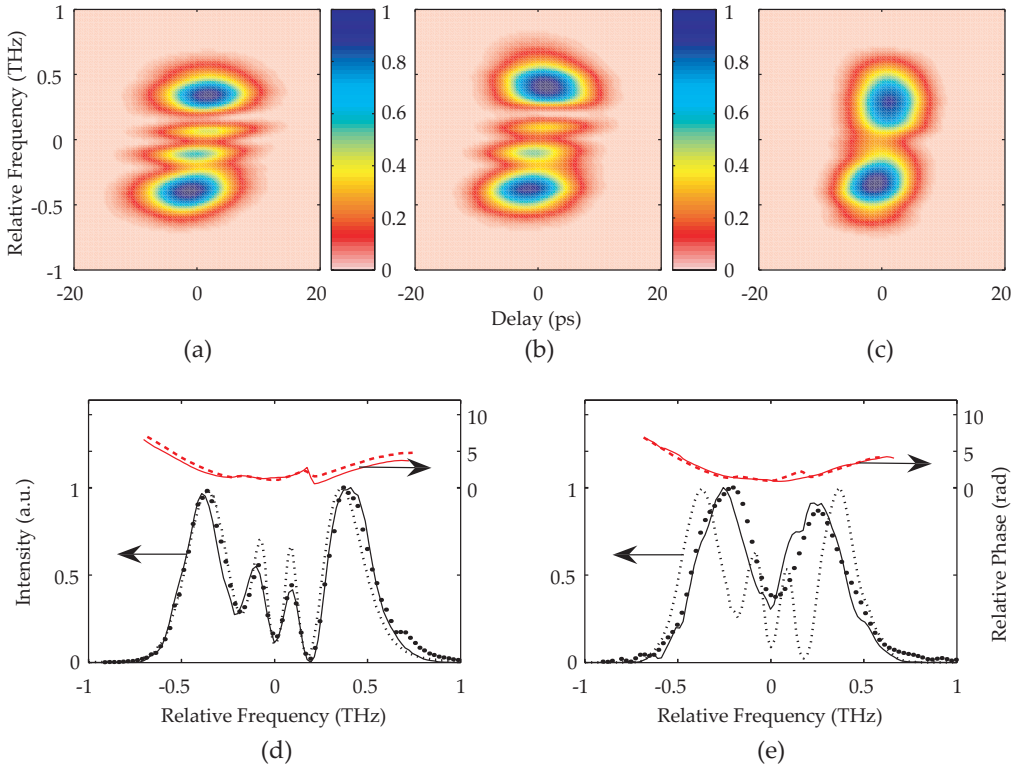

FIGURE 6.14: Demonstration of high fidelity parametric transfer. (a) Retrieved pump sonogram, (b) retrieved idler sonogram for actively preserving parametric transfer and (c) retrieved idler sonogram with no attempts to preserve transfer. (d) and (e) show the retrieved pump spectrum and phase (dashed curve) compared with the measured idler spectrum (circles) and retrieved idler spectrum and phase (solid) for the SPOPO arrangements maintaining and not maintaining high fidelity transfer.

Inspection of the spectral transfer shows the resolution of the central peaks of the idler spectrum to be much better than any of the previous results where only individual parameters were considered. Moreover, comparison to Fig. 6.14(c) and (e) where there is no signal bandwidth narrowing or cavity length tuning emphasizes the importance of implementing the measures that have been identified for enhancing fidelity. Such implementation, in this case, has resulted in an order of magnitude improvement of spectral transfer from $Z_S = 0.15$ to 0.015.

6.4 Conclusions

The factors affecting parametric transfer from the pump to the idler in a SPOPO have been experimentally investigated. The results presented here are in good agreement

with the numerical predictions in Chapter 5. It has been shown that signal bandwidth narrowing significantly improves the transfer and is easily achieved with an etalon in the SPOPO cavity. A low loss resonator achieved by the use of highly reflecting mirrors is required as this minimises the signal gain and helps to maintain a narrow signal bandwidth. In addition to this, operation should be near maximum pump depletion, corresponding to around four times above oscillation threshold, and below the level at which back-conversion begins to distort the transfer.

Although the optimum threshold position is already very close to optimum fidelity, cavity length tuning can somewhat improve the fidelity by compensating for pump-signal temporal walk-off. Temporal walk-off between the pump and idler causes significant degradation of transfer fidelity such that good fidelity can only be achieved within a small tolerance of the zero walk-off condition for this SPOPO arrangement, severely restricting the tunability. However, a larger wavelength range could easily be accessed with shorter crystal lengths or with a tunable pump source to minimise pump-idler temporal walk-off.

For the SPOPO arrangement described in this work, high fidelity transfer was achieved by implementing the measures identified for fidelity enhancement. The quality of transfer was evident in the comparison of the pump and idler sonogram traces and the retrieved spectral phase and amplitude of the pulses. In quantifying the fidelity, an order of magnitude improvement in spectral transfer fidelity was calculated. This demonstration of high fidelity transfer in a SPOPO from the NIR to the MIR realises the concept of high resolution MIR pulse shaping, via an optical parametric oscillator device. Without active preservation of the pulse shape, the work presented in this chapter has shown that the resolution of the required MIR pulse is severely hindered, thereby compromising the degree of precision that is essential for applications such as coherent control of molecules.

References

[1] H. S. S. Hung, J. Prawiharjo, N. K. Daga, D. C. Hanna, and D. P. Shepherd, "Experimental investigation of parametric transfer in synchronously pumped optical parametric oscillators," *J. Opt. Soc. Am. B* **24**(12), pp. 2998–3006, 2007.

[2] D. H. Jundt, "Temperature-dependent sellmeier equation for the index of refraction, n_e, in congruent lithium niobate," *Opt. Lett.* **22**(20), pp. 1553–1555, 1997.

[3] I. G. Cormack, W. Sibbett, and D. T. Reid, "Rapid measurement of ultrashort-pulse amplitude and phase from a two-photon absorption sonogram trace," *J. Opt. Soc. Am. B* **18**(9), pp. 1377–1382, 2001.

[4] J. Prawiharjo, H. S. S. Hung, D. C. Hanna, and D. P. Shepherd, "Numerical investigations of parametric transfer in synchronously pumped optical parametric oscillators for indirect mid-infrared pulse shaping," *J. Opt. Soc. Am. B* **24**(9), pp. 2484–2493, 2007.

Chapter 7

Adaptive Pulse Shaping in High Power Fibre-based Chirped Pulse Amplification Systems

7.1 Introduction

In the previous chapters, adaptive shaping of MIR pulses and high fidelity parametric transfer in a SPOPO have been demonstrated, concluding that the development of MIR pulse diagnostics, adaptive optimisation algorithms, pulse shaping techniques and parametric transfer components of this adaptive tunable MIR source should indeed lead to promising applications in chemistry. However, since most coherent control experiments occur within a femtosecond timescale, a new laser system would be required to replace the Nd:YLF picosecond laser/amplifier system used in the experiments thus far.

Moving into the femtosecond regime, however, is not a trivial task since, at these pulse durations higher order nonlinear effects become more significant. This is particularly true for fibre based systems, where the optical confinement lowers the threshold for nonlinear processes. The development of a high power fibre-based CPA system incorporating an adaptive pulse shaper is therefore interesting, not only for coherent control

applications, but also as a general means of improving the performance of these systems for many other applications.

The experimental work in this chapter was carried out in collaboration with Fei He who ran the fibre-based CPA system whilst I operated the pulse shaper and adaptive optimisation algorithm, which was written by Naveed Naz. The basis of the pulse propagation model was written by Jerry Prawiharjo, whilst I wrote the code describing the CPA system, and performed and analysed the numerical results.

7.2 Background

The generation of high-peak-power femtosecond pulses is often accomplished through CPA, where nonlinear effects are kept to a minimum by temporally stretching the pulse before amplification and then recompressing afterwards [1]. This technique has been used with great success with parametric [2], Ti:sapphire [3], and other bulk solid-state amplifier systems [4]. Fibre-based CPA, while not yet reaching such high pulse energies at such short pulse durations, can offer significant advantages for high-average-power systems with excellent beam quality [5]. However, imperfect correction of spectral phase distortions caused by high-order dispersion and residual nonlinear effects in the stretcher and amplifier can lead to non-transform-limited pulses at the output of the compressor. One method of attempting to overcome such limitations is to include a programmable pulse shaper [6] within the amplifier system to control the spectral phase and/or amplitude of the pulses. Such a shaper can be used before or after the amplifier but power handling considerations and the overall efficiency of the system often dictate that it be used in a pre-compensation role [7]. Adaptive pulse-shaping, using an optimization algorithm based on an experimental feedback parameter, has also been successfully employed [8] increasing the flexibility of the system to work at varying power levels. As dispersion, nonlinearity, and gain narrowing all need to be taken into account in a CPA, an adaptive system also greatly reduces the necessary computation for designing a compensation element.

The use of phase modulators to correct for SPM-induced phase distortions of up to 2π has been demonstrated in fibre CPA systems [9] and adaptive pulse shaping has been used to control the propagation of ultrashort pulses in optical fibres [10]. It is only recently however, that an experiment combining adaptive amplitude-only pulse shaping with fibre-based CPAs was demonstrated [11], even though nonlinear pulse distortions are very challenging in such systems due to the presence of high intensities over long lengths of fibre. In this report, Schimpf et al. [11], describe shaping the spectral amplitude of the pulse before it enters the amplifier and show high quality pre-compensation of pulses at B-integrals as high as 16. The selected parameter for the computer-controlled feedback loop was a target spectral shape and it was shown that imposing a parabolic shape was superior to a Gaussian shape for pulse energies up to 20 nJ and pulse durations of 300 fs at average powers of 1.5 W.

In this chapter, the use of phase-only shaping in a fibre CPA system is demonstrated comparing the use of a grating stretcher or fibre stretcher arrangement [12]. The shaper is placed before the grating/fibre stretcher and used in a pre-compensation setup through which the peak of the autocorrelation trace of the final compressed pulse is used as the feedback parameter in the adaptive control loop. The adaptive process was controlled by a simulated annealing algorithm and was used to optimise the coefficients of a Taylor expansion of the spectral phase profile. Three times improvement in the autocorrelation peak intensity was demonstrated for the grating stretcher arrangement, with close to transform-limited pulse durations of 800 fs at pulse energies of 65 μJ and a corresponding B-integral of ~ 8. Implementation of the shaper in the CPA fibre stretcher arrangement also yielded significant improvement in pulse quality for the same pulse energy, although the overall pulse quality was poorer than for the grating stretcher arrangement.

In Section 7.5 the experimental results of phase-only shaping are presented, giving details of the results obtained as the pulse energy is increased and of the performance of the adaptive control. Numerical modelling of the fibre stretcher system is also provided to gain a better understanding of the results obtained and discuss the limitations imposed by the pulse shaper on the fibre CPA system.

7.3 Phase-Only Pre-Compensation of Self-Phase Modulation

It is desirable to use pulse shaping at an early stage in a fibre CPA system since it avoids any damage issues which may arise due to high pulse energy or high average power. Moreover, the losses associated with the pulse shaper need not seriously affect the overall efficiency of the system if the final amplification stage is saturated. Typically, nonlinear distortion that affects fibre CPAs is SPM and so the question arises as to whether it is possible to pre-compensate for SPM by spectral phase shaping.

It has been argued [13] that in the situation where the pulse propagates for a long distance through a dispersive stretcher, such that the temporal intensity profile becomes proportional to the spectral intensity, $I(t) \sim I(\omega)$, then SPM in the amplifier section merely introduces a frequency dependent phase with negligible effect on the spectral bandwidth of the pulse, [14]. Such a frequency-dependent phase could indeed be readily pre-compensated by a phase-only pulse shaper. However, it should also be noted that SPM by itself only causes changes to the spectrum and does not change the temporal intensity of the pulse. Thus a chirped pulse produced by SPM-induced spectral broadening of a bandwidth-limited pulse cannot be pre-compensated by a spectral phase shaper to give a bandwidth-limited pulse (which would be shorter than the original bandwidth-limited pulse), as the shaper would have to produce a shorter than bandwidth-limited pulse prior to the SPM. Going beyond these simple arguments requires numerical modelling, especially if one wishes to look at the effects of noise on the system or indeed to include other effects such as gain narrowing of the spectrum in the amplifier chain.

Sato et al. [15] reported numerical modelling of adaptive shaping for femtosecond pulse propagation in a fibre, showing that phase-only shaping can pre-compensate for GDD and SPM. However, they also report that this pre-compensation is only successful up to certain powers (100kW for a 0.114m length of single-mode fibre). Similarly, Braun et al. [13], reported numerical modelling of phase-only pre-compensation in a fibre CPA system showing good behaviour for nonlinear phase of up to 3 rad. Numerical modelling of spectral amplitude pre-compensation in a fibre CPA system with large

amounts of SPM was reported by Schreiber et al. [16], confirming the experimental results described in [11]. However, they also point out that small noise levels and gain shaping can seriously affect the final recompression.

A numerical model is presented in Section 7.5.3, after the experimental results are presented, and aims to bring out general features of phase-only pulse shaping in CPA systems in the presence of SPM broadening and dispersion.

7.4 Experimental Arrangement

7.4.1 The Chirped Pulse Amplifier

A schematic of the CPA system is shown in Fig. 7.1. The pump source is a mode-locked 1.053 μm Nd:glass laser that delivers ~500 fs pulses at a repetition rate of 80 MHz. These pulses are shaped with a phase-only pulse shaper before being stretched to ~1ns with either a grating stretcher or a fibre stretcher. An electro-optic modulator then reduces the repetition rate to 100 kHz before amplification to 0.1 W using the core-pumped Yb-fibre pre-amplifiers. High pulse energies were achieved with two cladding-pumped amplifiers, each of which used a 2 m length of double-clad Yb-doped photonic crystal fibre (PCF) from Crystal Fibre (core diameter 40 μm, NA 0.03; inner cladding diameter 170 μm, NA 0.6) and fiberised 975 nm pump laser diodes (diode powers were 6 W and 20 W respectively). Acousto-optic modulators prevented ASE build-up, and reduced the final repetition rate to 16.67 kHz. A dielectric grating compressor, with 65% overall transmission efficiency, recompressed the pulses. The maximum amplitude of the autocorrelation trace minus the minimum within the measuring window (30 ps) was used as the feedback parameter for the adaptive loop, which modified the phase profile applied at the shaper. The quality of the pulses without adaptive shaping is shown in Fig. 7.2. Compensation of the SPM effects using the final grating compressor, to match the second and third order dispersion of the grating stretcher, yields high quality pulses at low energy for the bulk stretcher setup. At high pulse energies of 65 μJ, the autocorrelation trace has a large pedestal that cannot be removed with tuning of the compressor. The fibre stretcher arrangement, yields pulses with substantially larger

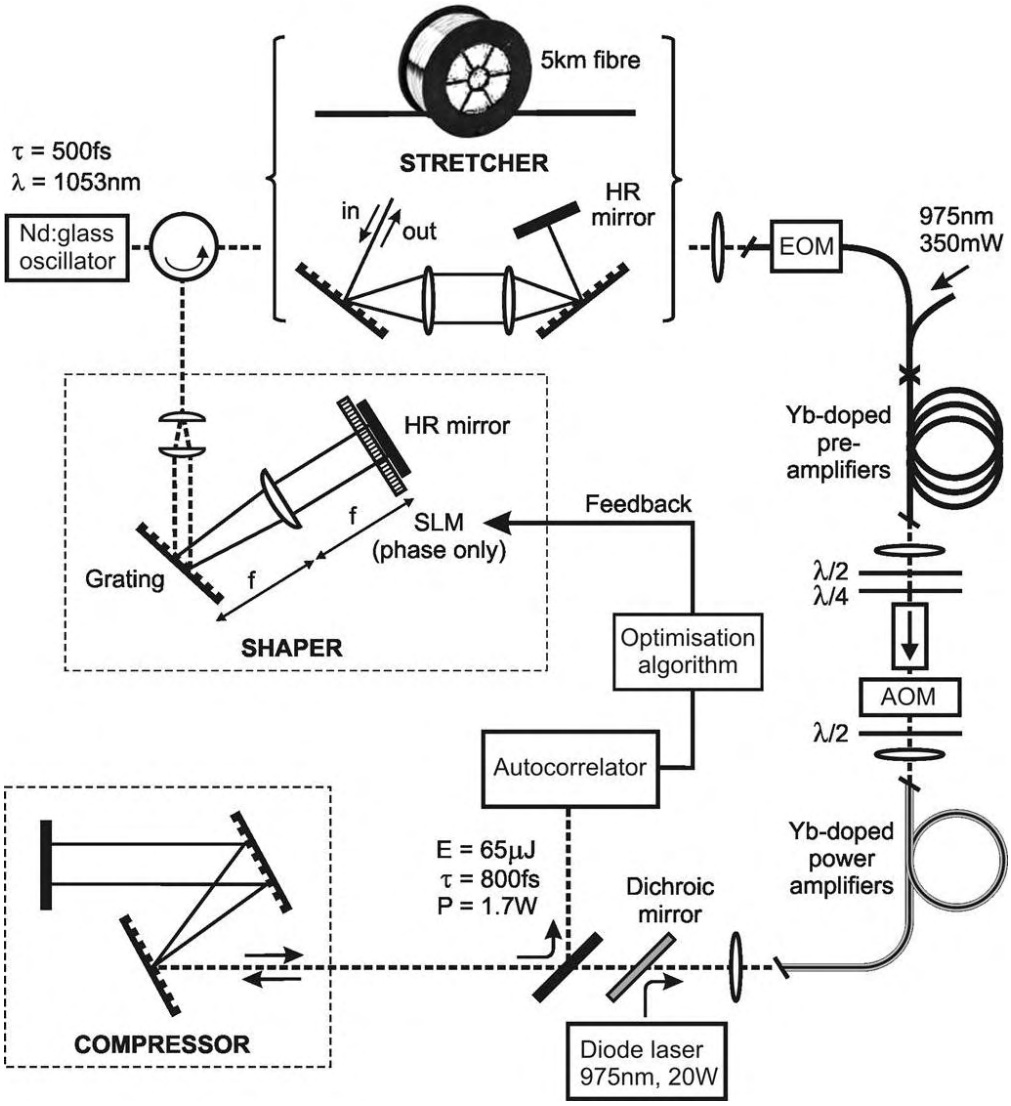

FIGURE 7.1: Shematic of the CPA system.

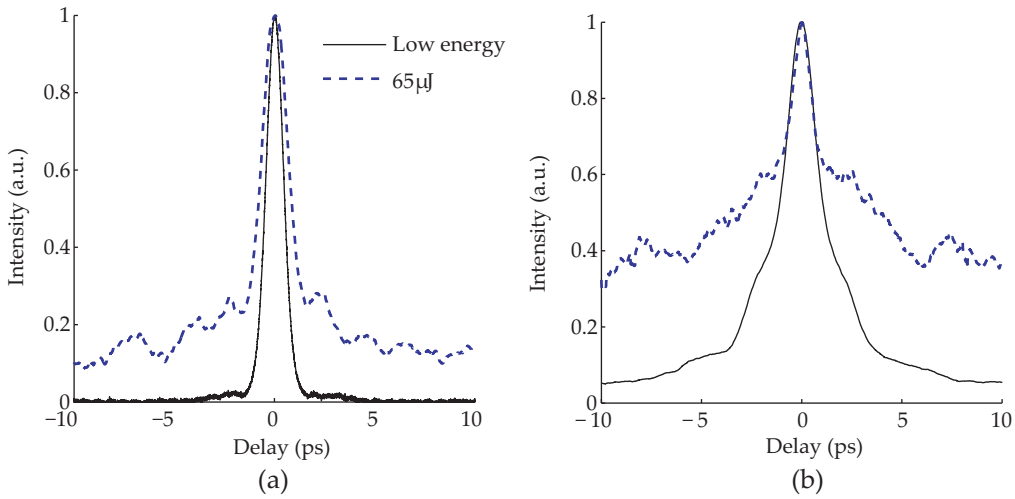

FIGURE 7.2: Autocorrelations for the unshaped pulses of the (a) bulk stretcher and (b) fibre stretcher systems for high and low energy pulses.

pedestals, even at low energy, due to large amounts of residual third order dispersion since the fibre stretcher and grating compressor can be matched for second but not third order dispersion. It is therefore evident that manipulation of the pulse shape in the CPA system is required to achieve higher quality pulses, particularly at high energies.

7.4.2 Adaptive Pulse Shaping

7.4.2.1 The Shaper

The pulse shaper is arranged in a folded 4-f configuration [6]. It consists of a diffraction grating with a groove density of 1100 lines/mm, cylindrical lens (f = 200 mm), SLM and a flat mirror to retroreflect the input beam. The SLM is a phase-only liquid crystal array of 128 pixels covering a distance of 12.8 mm (CRI SLM-128-MIR). The 10 nm bandwidth input beam was expanded to a collimated beam radius of 6 mm and was incident upon the diffraction grating at an angle of 10 degrees, with a corresponding diffracted angle of 80 degrees. From these parameters and using the equations presented in Ref. [6] the calculated beam shaper characteristics are given in Table 7.1.

Characteristic at the Mask	**Value**
Spatial dispersion α	7.5×10^{-16} m/(rad/s) or 0.78 nm/mm
Radius of a single frequency component, w_0	64 μm
Spectral resolution, δf or $\delta\lambda$	7.2x10^{10} Hz or 0.04 nm
Complexity, η	250
Temporal resolution,δt	160 fs
Time window, T	40 ps

TABLE 7.1: Pulse shaping parameters.

The characteristics shown in Table 7.1 are for the shaper without considering the pixellation of the mask. However, ultimately, the maximum complexity, η, is limited by the number of pixels to 128 and thus the finest achievable spectral feature, $\delta\lambda$, is 0.078 nm and the time window, T, is 20 ps. As discussed in Chapter 2, it should be noted that while the time window is the period over which the output pulse is affected by the mask, it does not mean that it is incompatible with the use of pulses stretched to durations much longer than T, as is the case here.

The absolute phase that can be applied by the SLM at 1053 nm varies between 1 and 11 radians. The computer control therefore enforces phase wrapping between these limits if higher magnitude phase profiles are required. We observed experimentally that spectral amplitude distortions appeared where these phase wrappings occur due to localised parts of the beam being diffracted out as a result of the phase discontinuity. This had little effect on the adaptive outcome for profiles that were wrapped near the wings of the pulse.

Another consequence of the shaper pixellation is to limit the complexity of the phase profile. As described earlier in Section 2.2.1, this means that the maximum magnitude of the phase profile is limited by the Nyquist sampling theorem to π per pixel [17]. Recall from Eqn. 2.26 that, for a phase that consists only of nth order phase, the nth order dispersion limit $\beta_{n_{max}}$ is described by,

$$\beta_{n_{max}} = \pm \frac{(n-1)!}{2} \frac{\lambda_0^{2n}}{(N_{pix}\pi)^{n-1}(c\Delta\lambda)^n} \,. \tag{7.1}$$

For the shaper described here, the maximum $\beta_{2_{max}}$ is 2.80 $\mathrm{ps}^2/\mathrm{rad}$, $\beta_{3_{max}}$ is limited to 0.66 $\mathrm{ps}^3/\mathrm{rad}^2$, and the fourth order dispersion parameter is limited to 0.233$\mathrm{ps}^4/\mathrm{rad}^3$.

7.4.2.2 Adaptive Control

In this work, an optimisation algorithm known as the generalised simulated annealing (GSA) algorithm [18] was used, which was introduced earlier in Section 2.4. It combines the classical simulated annealing technique [19] with the later developed fast simulated annealing method [20], providing a significantly faster convergence. The main parameters that affect the convergence are the initial acceptance temperature, T_a, the acceptance parameter, q_a, the initial visiting temperature, T_v, and the visiting parameter, q_v. The acceptance parameter defines the probability of accepting an outcome and the visiting parameter determines the rate of convergence. Typically, the algorithm ran for 150 iterations with $\mathrm{T}_a = \mathrm{T}_v$ set to be twice the expected value of the optimised feedback parameter (i.e. twice the maximum minus the minimum voltage of the autocorrelation). As the optimised feedback parameter value was not known in advance of

the experiment a few trial runs were carried out first to estimate a reasonable value of T_0. The acceptance and visiting parameters were initially set to similar values used in reference [18] and following several trial runs, the parameters $q_a = 1$ and $q_v = 2.5$ were chosen to be the most effective.

The phase was described by a Taylor series expansion as was done previously in Chapter 4, so that the 128 pixels could all be addressed with only a few optimisation parameters and thus achieve faster convergence. The phase applied, $\phi_{SLM}(\Omega)$, was described by,

$$\phi_{SLM}(\Omega) = \beta_0 + \beta_1\Omega + \beta_2\frac{\Omega^2}{2!} + \beta_3\frac{\Omega^3}{3!} + \beta_4\frac{\Omega^4}{4!} + \dots , \tag{7.2}$$

Where Ω is the frequency detuning and β_n, is the nth order dispersion. Results for the bulk stretcher system modified the 2nd to 6th order dispersion of the above expansion. However, for the fibre stretcher system, it was found that optimisation from the linear to the 4th order dispersion was sufficient.

Figure 7.3 shows a set of typical convergence data for the feedback parameter and the optimisation parameters. It can be seen from this data that the algorithm converges quickly, typically within the first 100 iterations, which took ∼2 minutes.

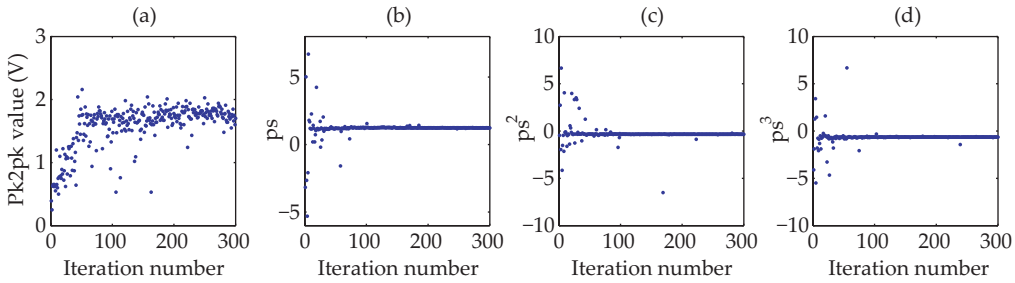

FIGURE 7.3: Convergence data for (a) the feedback parameter and the (b) linear, (c) second, and (d) third order dispersion parameters of the GSA algorithm.

7.5 Results

7.5.1 Grating Stretcher

In the grating stretcher setup, the second and third order dispersion from the stretcher is well matched to the compressor. Figure 7.4(a) shows high quality pulses with no shaping at pulse energies of 13 μJ after the compressor, which was tuned to optimise the pulse compression. Adaptive pulse shaping improved the autocorrelation peak height by just 20%. With the compressor fixed at the optimum position for 13 μJ, the CPA

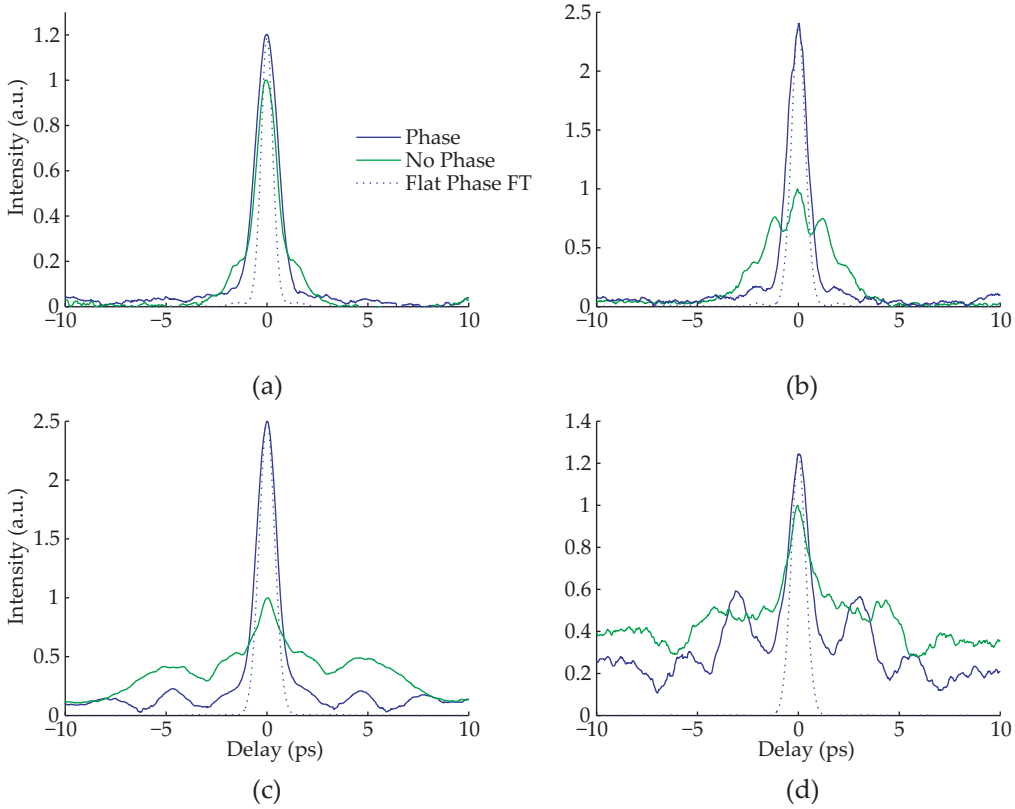

FIGURE 7.4: Autocorrelation traces measured with (blue) and without (green) shaping at output pulse energies of (a) 13 μJ, (b) 26μ J, (c) 65 μJ, and (d) 104 μJ. Calculated autocorrelations of the flat phase FT of the measured spectra are also shown (blue dashed). The compressor grating separation is optimised at low energies.

output energy was increased to test the energy limitations of the adaptive CPA system. These autocorrelations are shown in Fig. 7.4 (b) to (d). As the pulse energy after the compressor increased to 104 μJ, the adaptive shaper struggled to suppress the increasing wings of the pulse. Inspection of the values of the second order phase imposed by the shaper showed that it increased with the pulse energy, gradually exceeding the Nyquist

limit as well as having increased phase wrapping. To reduce the required phase imparted by the shaper and hence place less strain on the shaper limits, the compressor was tuned to minimise the pulse duration before applying the adaptively optimised phase for 65 and 104 μJ pulse energies. The results in Fig. 7.5 (a) and (b) show improvement to the pulse quality due to additional compensation from the compressor, particularly for pulse energies of 65 μJ where the wing structure is significantly reduced and the autocorrelation peak intensity is improved by a factor of three.

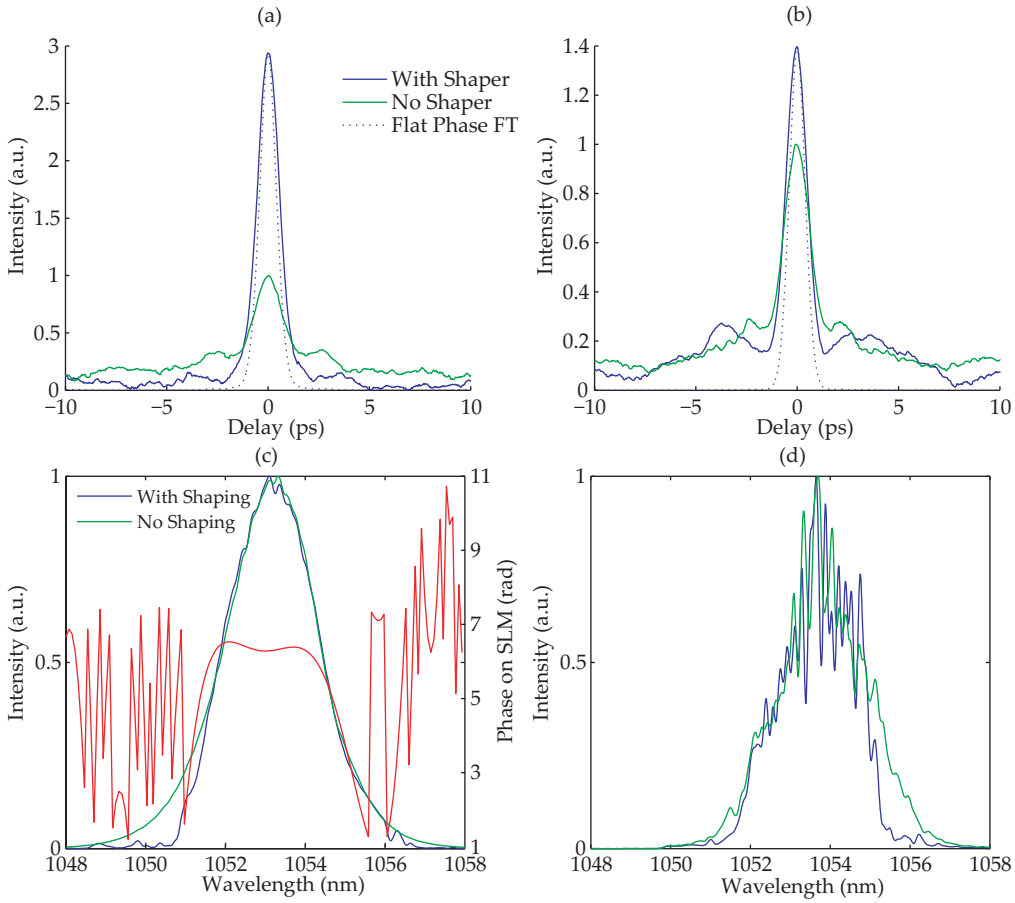

FIGURE 7.5: Autocorrelation traces measured with (blue) and without (green) shaping at pulse energies of (a) 65 μJ, and (b) 104 μJ. Calculated autocorrelations of the flat phase FFT of the measured spectra are also shown (blue dashed). The compressor grating separation is optimised in each case. The spectra at (c) the shaper and (d) the 65 μJ output of the adaptive CPA system are also shown.

The spectral evolution of the pulse shape in the CPA system, after the shaper and at the system output, for 65 μJ pulse energy is shown in Fig. 7.5 (c) and (d). The spectral amplitude is mostly unchanged by the pulse shaper except for a small amount of distortion at the edges of the spectrum due to phase wrapping. The oscillatory feature

that appears on the spectra was experimentally observed to increase with pulse energy, and as such, is believed to be due to SPM effects occurring in the amplifier stages. Inspection of the optimum phase shaping parameters found that the shaper limits were exceeded at 65 μJ but the distortions occurred at the edge of the pulse. It is thought that, as a result of the increasing SPM with pulse energy, the shaper limits are further exceeded beyond 65 μJ, so that for higher energies sub-optimal solutions, like the one in Fig. 7.5(b) for 104 μJ, are found. Further discussion on the limitations imposed by the shaper will be presented, following numerical modelling of the system, in Section 7.5.3.

7.5.2 Fibre Stretcher

A 5km length of Corning fibre (SMF28e) was then used as a fibre stretcher in place of the bulk grating stretcher. This resulted in a large residual third order dispersion as the stretcher added to the third order contribution from the compressor. Figure 7.6(a) shows an autocorrelation trace of the pulse without shaping (green) showing features that are typical of a pulse with third order dispersion. The data depicted in Fig. 7.6 (a) and (b) were taken at low energy (1nJ). With no SPM in the system, the phase shaping leads to pulses that are much improved in quality but with a small pedestal. Moreover, the shaped pulse is not fully compressed. The flat phase limit calculated from the FT of the measured spectral data is approximately half the width of the shaped pulse. Since, at these low energies, the pulse shaper is required to compensate only for the stretcher/compressor mismatch without SPM, the result that full compression could not be achieved was unexpected. For a bandwidth limited pulse propagating in the stretcher, the TOD induced is negligible. Therefore the TOD from the compressor dominates and at low power and with no SPM in the stretcher, the shaper should be able to compensate for this. Based on the free-space grating separation, the TOD contribution from the compressor is calculated to be 0.92 $\mathrm{ps}^3/\mathrm{rad}^2$. Since the shaper is in a folded configuration, the SLM is doubled-passed and we expect the shaper TOD to be $\sim$0.46 $\mathrm{ps}^3/\mathrm{rad}^2$. This is close to but within the TOD limit of 0.66 $\mathrm{ps}^3/\mathrm{rad}^2$ expressed in Eqn. 7.1 for a purely TOD phase. However, for the results presented in Fig. 7.6, inspection of the phase profile found by the optimisation routine finds that whilst the

optimised third order coefficient was well within the Nyquist limit, the π per pixel limit is exceeded at the edges of the spectrum due to the combined contributions from all the dispersion terms in unison. It is therefore concluded that the magnitude of the dispersion mismatch was beyond the limits of the pulse shaper. Further discussion of the limitations are discussed in section 7.5.3.

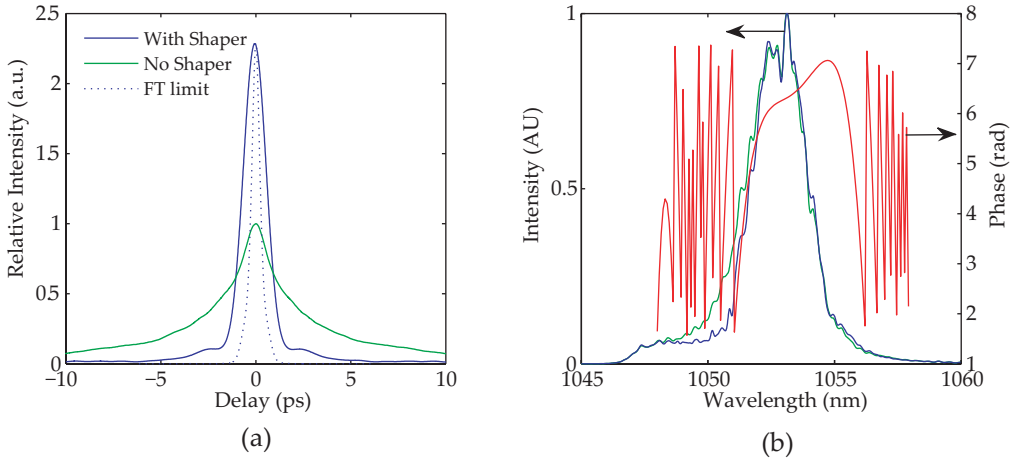

FIGURE 7.6: Low energy, no SPM in the system. (a) Autocorrelations of the unshaped (dashed blue), shaped (red) and compressed pulse limit (dashed green) and (b) corresponding spectra.

For high energy pulses, the power launched into the stretcher had to be increased to minimise amplifier noise, resulting in SPM effects in both the fibre stretcher and the amplifier stages. The pulse shaper would thus have to pre-compensate these effects as well as the stretcher/compressor mismatch. With significant SPM in the stretcher but with the CPA output pulse still at low energy, adaptive compression of the pulse resulted in the autocorrelation shown in Fig. 7.7(a), showing a large pedestal. Here the compressor was adjusted to compensate for the GDD induced by the stretcher. Subsequent results in Fig. 7.7 were then taken with the compressor gradually detuned from the minimum GDD point. The roof mirror of the compressor arrangement was moved by - 10mm and -15mm. Results show that as the compressor is moved, the autocorrelation quality improves and the peak height is improved by almost 5 times for a movement of 15mm. With the detuned compressor, the pulse after the shaper is forced into being stretched, therefore lowering the peak power and SPM induced in the fibre stretcher. However, the phase profile applied by the shaper was found to exceed the Nyquist limit as well as having significant amounts of phase-wrapping, resulting in

phase to amplitude distortions of the spectrum. The output spectrum after shaping is thus significantly narrower than without shaping such that the flat phase limit of the pulse is now artificially broadened to be a closer match to the shaped AC.

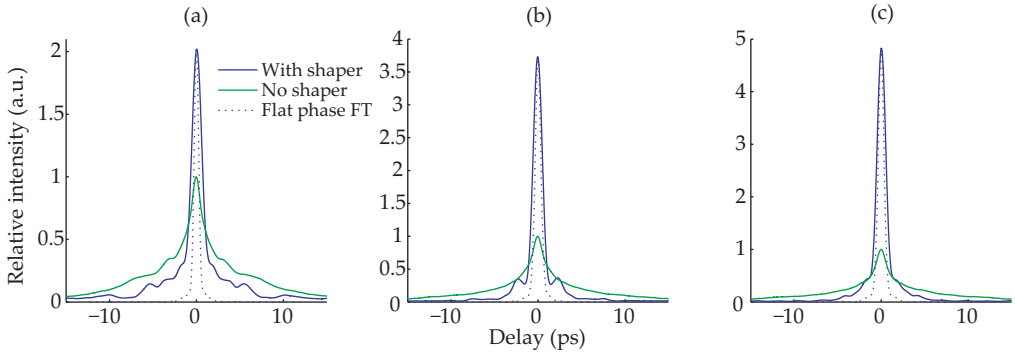

FIGURE 7.7: Autocorrelations at low energy but with significant SPM in the stretcher at different roof mirror offsets of the compressor of (a) 0 mm, (b) -10 mm, and (c) -15 mm.

At high energies the adaptive CPA system was able to achieve significant improvement in pulse quality, even at 104 μJ. However, the pulses still had a large pedestal and were not compressed near the theoretical limit. Figure 7.8 shows the autocorrelations at pulse energies ranging from 13 μJ to 104 μJ at a compressor offset of -10 mm from the minimum GDD point of the 13 μJ setup.

The spectral evolution for a 65 μJ pulse in the system is shown in Fig. 7.9. With no shaping, the spectral FWHM after the stretcher is broadened from ~2.5 nm to ~6.5 nm. In the amplifiers, the pulse experiences gain narrowing to a FWHM of ~4 nm with a shift in the peak wavelength by ~2 nm and the spectrum acquires oscillatory features due to SPM. The spectra of the shaped pulses are somewhat changed compared to the unshaped spectra with reduction of the spectral amplitude at the edge of the spectrum due to phase wrapping. The changes in main part of the spectrum are due to the change in peak power, pulse duration and spectral phase imparted by the pulse shaper leading to significant moderation of the effect of the SPM in the fibre stretcher.

From the results presented here, it has been shown that although significant improvement in pulse quality can be achieved through pulse shaping, the presence of the large pedestal at high power and inability to compress close to the flat phase limit, even at low power, hinders the performance of a CPA system with a fibre stretcher and phase

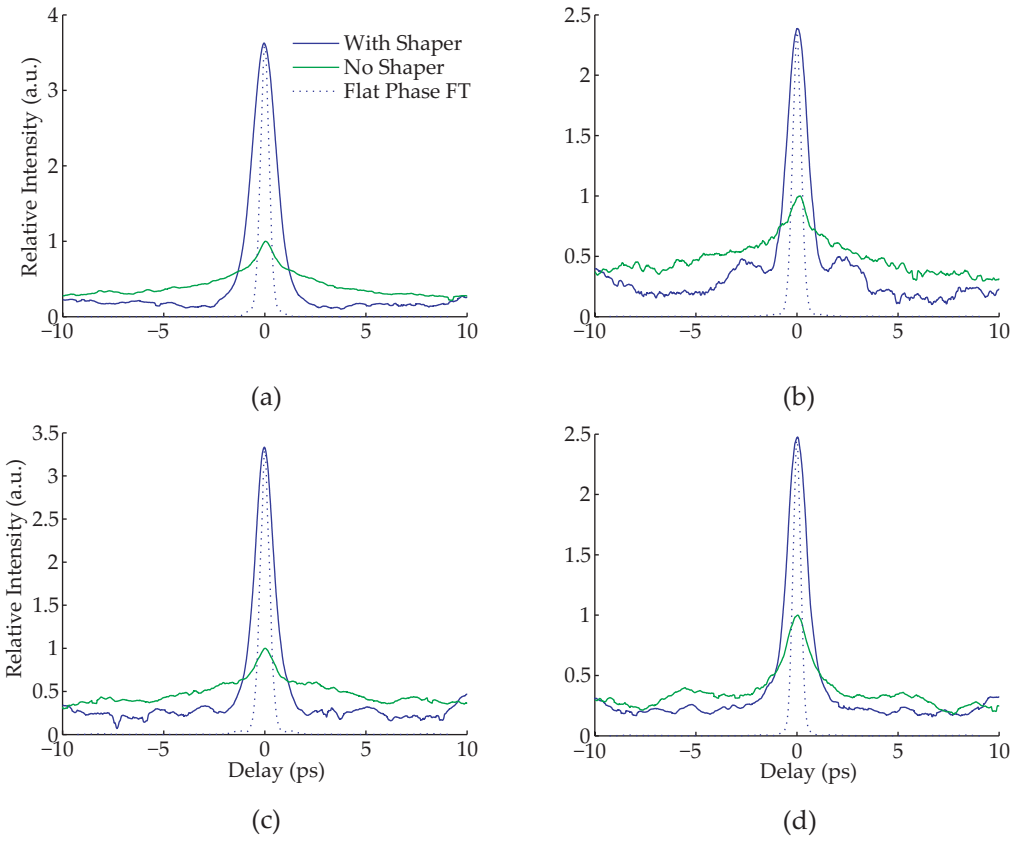

FIGURE 7.8: Autocorrelations of output pulses with and without pulse shaping for pulse energies of (a) 13 μJ, (b) 33 μJ, (c) 65 μJ, and (d) 104 μJ.

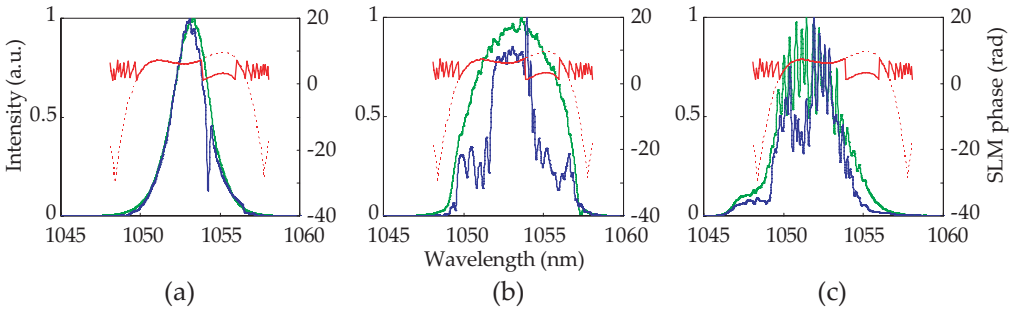

FIGURE 7.9: Spectral evolution of the pulse in the CPA system with (blue) and without (green) shaping, (a) before the stretcher, (b) after the stretcher, and (c) after the compressor. The wrapped (red) and unwrapped (red dashed) phase profiles are also shown. The turning points in the unwrapped profile are a residual effect from the Nyquist limit as the number of sampling points (i.e. pixels) is not enough for the phase to be unwrapped correctly.

pre-compensation. Further understanding of the limitations of this system is required and is therefore investigated in the next section.

7.5.3 Numerical Modelling of the fibre stretcher CPA system

A pulse propagation method is used to simulate a simplified model of a fibre stretcher CPA system to investigate the limitations of the pulse shaping component. In particular, the two cases of pre-compensation and post-compensation of the phase before or after the fibre stretcher, are compared. The initial pulse is described as a Gaussian bandwidth-limited pulse and the phase in the system is modelled in the spectral domain as described by Eqn. 7.2. The phase accumulated in the fibre stretcher, the shaper, and the compressor is also considered in the model.

The effect of gain and gain narrowing in the amplifiers was also considered but it was found that, for the situation modelled here, there was no mentionable additional effect to the limits imposed by the shaper on the system output. The amplifier stages have therefore been neglected in this numerical discussion.

Propagation of the pulse in the fibre stretcher is modelled using the split-step Fourier method with the Runge-Kutta integrator to solve the nonlinear Schroedinger equation along a 2 km length with a dispersion parameter, b_F, of 20 $\mathrm{ps^2 km^{-1}}$ and a nonlinear coefficient, α_F, of 3 $\mathrm{radW^{-1}km^{-1}}$. The nonlinear Schroedinger equation of a pulse propagating in the fibre, described by the slowly varying electric field, A_F, is given by [21],

$$\frac{\partial A_F}{\partial z} + \frac{i b_F}{2}\frac{\partial^2 A_F}{\partial t^2} - i\alpha_F \left|A_F\right|^2 A_F = 0\,. \tag{7.3}$$

The initial input pulse is described by the following relation,

$$A_F(0,t) = \sqrt{P_{pk}} \exp\left[-2\ln 2\left(\frac{t}{\delta t_F}\right)^2\right]\,, \tag{7.4}$$

where P_{pk} is the peak power which was chosen to be 50W and δf_F is the initial pulse at 600 fs. The pulse is stretched from 600 fs to $\sim$300 ps and recompressed using a grating compressor to compensate for the GDD. Dispersion coefficients (second, third and fourth

order dispersion of a Taylor series expansion) for the grating compressor were calculated from standard equations [22] for a grating pair compressor. The shaper was implemented either before or after the stretcher. The peak of the pulse intensity was used as a feedback loop for the GSA to optimise the shaper phase which could compensate from second to sixth order dispersion of the Taylor series expansion. The phase was a smooth, continuous profile that extended over the entire frequency range of the numerical model. The first 200 iterations of the algorithm optimised the first 3 parameters and the last two were included in the final 800 iterations.

Comparison of the pre- and post-compensation schemes is shown in Fig. 7.10 for an input peak power of 50 W resulting in spectral broadening of the pulse due to SPM in the fibre stretcher from 0.7 THz to 1.4 THz. Post-compensation of this accumulated phase results in a bandwidth limited pulse, whereas shoulders are observed in the autocorrelation of the pre-compensated pulse. This shows that in the arrangement with the shaper before the stretcher, the shaper is unable to fully pre-compensate for the SPM phase. Moreover the chirped pulse induces complex structure to the SPM induced spectrum compared with the smooth Gaussian shape of the spectrum from the post-compensation scheme.

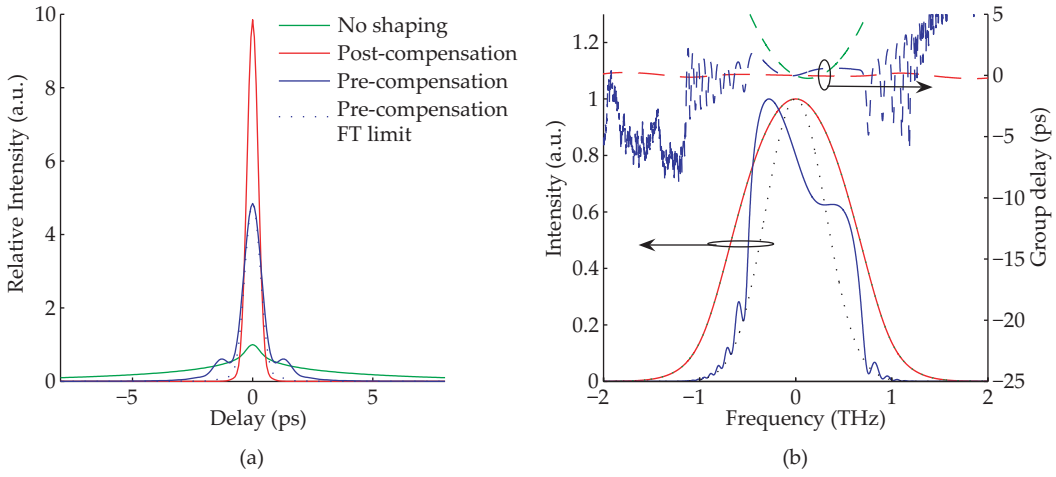

FIGURE 7.10: Autocorrelations (a) and spectral phase and amplitude (b) of the CPA output with no shaping (green), post-compensation (red) and pre-compensation (blue). The black dotted line in (b) indicates the input spectrum.

By reducing the input peak power to 1 W one can eliminate the SPM broadening. Results from Fig. 7.11(a) show that for a pre-compensating scheme, a bandwidth limited pulse can be achieved showing that the results presented in Fig. 7.6 should, in theory, have

been able to be fully compressed. It was believed that the inability to achieve this was due to the optimum phase being outside the limits of the pulse shaper. A similar Nyquist limit was therefore implemented on the numerical model to verify this. The phase profile was "pixellated" by sampling the phase profile over 32 points across 10 nm with the phase wrapped between ∼1-11 radians. Beyond the 10 nm range, the phase was set to zero. Figure 7.11(b) shows that reducing the sampling results in a system that cannot reach the bandwidth limit as the Nyquist limit is exceeded. Moreover, in practice, if there are many phase jumps due to phase wrapping, the amplitude of the pulse will be slightly diminished. This could result in the theoretical infinite resolution mask solution for an optimally compressed pulse to no longer be the global optimum.

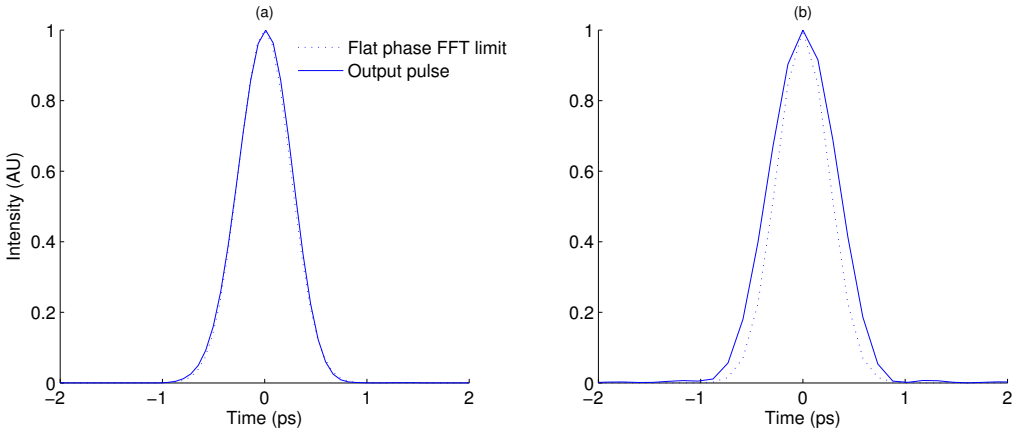

FIGURE 7.11: Intensity of the CPA output with (a) a high resolution shaper (b) a low resolution shaper of 32 pixels.

The results presented in this numerical work show that SPM broadening in the fibre stretcher and the pixellation of the shaper limit the fibre stretcher CPA system. Pre-compensation of SPM effects is only possible for low SPM before the onset of spectral broadening, after which the fundamental bandwidth limit cannot allow the output pulse to be fully compressed. The SPM can also result in oscillatory structure of the spectrum requiring a high resolution pulse shaper to avoid the Nyquist limit. In the experimental system, SPM in the amplifier stages could also further limit the pulse quality by introducing more nonlinear effects and spectral broadening if insufficient stretching had occurred that would therefore be difficult to pre-compensate with the shaper. Due to the practical damage limitations of pulse shapers, the shaping must always occur before the

amplification stage thereby placing a limit on the output pulse energy for high quality pulses.

7.6 Discussion and Conclusions

The results presented in this chapter show that, of the two experimentally investigated adaptive fibre CPA systems, the bulk stretcher setup resulted in higher quality shaped pulses at 65 μJ pulse energies. This is largely due to the dispersion mismatch between the fibre stretcher and compressor requiring a shaper phase profile that exceeds the physical limits of our shaper setup. The consequence of the pixellation and phase wrapping boundaries of the shaper are such that the phase that should produce the optimum pulse shape is no longer the global minimum and thus a new sub- optimal solution, one that is the optimum within the constrained parameter space, is found. This resulted in an inability to fully compress pulses from the fibre stretcher setup, even at low energies and negligible SPM broadening. Experiments at low energy for the bulk stretcher setup succeeded in producing pulse widths close to the flat phase limit and required only very small phase parameters, well within the Nyquist limit. At higher energies, the bulk stretcher started to exceed the shaper limits, but with the help of the compressor to compensate for the SPM induced GDD, the performance of the system was improved. Reducing the GDD component of the shaper had the effect of lowering the rate of change of phase near the centre of the spectrum and hence pushing the phase to amplitude distortions to the edges of the spectrum.

Results from the numerical work found that as well as the limitations of the shaper, significant SPM spectral broadening in the fibre stretcher could also limit the fibre CPA. This applies to the bulk stretcher as well as the fibre stretcher setup due to the nonlinear phase in the amplifier stages, but because of gain narrowing, the spectral broadening is restricted and its impact on performance is not as immediate as the shaper limitations which are believed to be brought on by the oscillatory spectral structure due to high SPM.

For the fibre stretcher setup, it appears that the shaper limits were reached at low energies such that full compression could not be achieved even with no SPM. At higher energies, the pulse shaper was able to improve the pulse quality of the fibre stretcher setup but significant pedestal structure still remained. It is believed that full compression could not be achieved due to fundamental limits on pre-compensation of SPM effects as well as the pulse shaper limits.

From the numerical results of the fibre stretcher setup, it is shown that improvements can be made by placing the pulse shaper after the fibre stretcher. The Nyquist limit can be improved by having more pixels, thus increasing the potential complexity of the phase. In addition, phase wrapping should ideally be avoided due to diffraction effects. Other SLM techniques such as optically addressed liquid crystal modulators or MEMS micromirror arrays could potentially provide smoother phase profiles.

Further work into both phase and amplitude shaping in an adaptive fibre CPA system with a fibre stretcher in a post-compensation arrangement, is anticipated following investigations into other optimisation methods and feedback parameters.

References

[1] D. Strickland and G. Mourou, "Compression of amplified chirped optical pulses," *Opt. Commun.* **55**(6), pp. 447–449, 1985.

[2] A. Dubietis, R. Butkus, and A. P. Piskarskas, "Trends in chirped pulse optical parametric amplification," *Selected Topics in Quantum Electronics, IEEE Journal of* **12**(2), pp. 163–172, 2006.

[3] H. Takada and K. Torizuka, "Design and construction of a TW-class 12-fs Ti:Sapphire chirped-pulse amplification system," *Selected Topics in Quantum Electronics, IEEE Journal of* **12**(2), pp. 201–212, 2006.

[4] K. Ogawa, Y. Akahane, M. Aoyama, K. Tsuji, S. Tokita, J. Kawanaka, H. Nishioka, and K. Yamakawa, "Multi-millijoule, diode-pumped, cryogenically-cooled Yb:KY(WO4)^2 chirped-pulse regenerative amplifier," *Opt. Express* **15**(14), pp. 8598–8602, 2007.

[5] F. Röser, D. Schimpf, O. Schmidt, B. Ortaç, K. Rademaker, J. Limpert, and A. Tünnermann, "90 W average power 100μJ energy femtosecond fiber chirped-pulse amplification system," *Opt. Lett.* **32**(15), pp. 2230–2232, 2007.

[6] A. M. Weiner, "Femtosecond pulse shaping using spatial light modulators," *Rev. Sci. Instrum.* **71**(5), pp. 1929–1960, 2000.

[7] M. A. Dugan, J. X. Tull, and W. S. Warren, "High-resolution acousto-optic shaping of unamplified and amplified femtosecond laser pulses," *J. Opt. Soc. Am. B* **14**(9), pp. 2348–2358, 1997.

[8] A. Efimov, M. D. Moores, N. M. Beach, J. L. Krause, and D. H. Reitze, "Adaptive control of pulse phase in a chirped-pulse amplifier," *Opt. Lett.* **23**(24), pp. 1915–1917, 1998.

[9] F. G. Omenetto, D. H. Reitze, B. P. Luce, M. D. Moores, and A. J. Taylor, "Adaptive control methods for ultrafast pulse propagation in optical fibers," *Selected Topics in Quantum Electronics, IEEE Journal of* **8**(3), pp. 690–698, 2002.

[10] G. Zhu, J. Edinberg, and C. Xu, "Nonlinear distortion free fiber-based chirped pulse amplification with self-phase modulation up to 2π," *Opt. Express* **15**(5), pp. 2530–2534, 2007.

[11] D. N. Schimpf, J. Limpert, and A. Tünnermann, "Controlling the influence of SPM in fiber-based chirped-pulse amplification systems by using an actively shaped parabolic spectrum," *Opt. Express* **15**(25), pp. 16945–16953, 2007.

[12] F. He, H. S. S. Hung, J. H. V. Price, N. K. Daga, N. Naz, J. Prawiharjo, D. C. Hanna, D. P. Shepherd, D. J. Richardson, J. W. Dawson, C. W. Siders, and C. P. Barty, "High energy femtosecond fiber chirped pulse amplification system with adaptive phase control," *Opt. Express* **16**(8), pp. 5813–5821, 2008.

[13] A. Braun, S. Kane, and T. Norris, "Compensation of self-phase modulation in chirped-pulse amplification laser systems," *Opt. Lett.* **22**(9), pp. 615–617, 1997.

[14] M. D. Perry, T. Ditmire, and B. C. Stuart, "Self-phase modulation in chirped-pulse amplification," *Opt. Lett.* **19**(24), p. 2149, 1994.

[15] M. Sato, M. Suzuki, M. Shiozawa, T. Tanabe, K. Ohno, and F. Kannari, "Adaptive pulse shaping of femtosecond laser pulses in amplitude and phase through a single-mode fiber by referring to frequency-resolved optical gating patterns," *Japan. J. App. Phys* **41**(6A), pp. 3704–3709, 2002.

[16] T. Schreiber, D. Schimpf, D. Muller, F. Roser, J. Limpert, and A. Tunnermann, "Influence of pulse shape in self-phase-modulation-limited chirped pulse fiber amplifier systems," *J. Opt. Soc. Am. B* **24**(8), pp. 1809–1814, 2007.

[17] G. Stobrawa, M. Hacker, T. Feurer, D. Zeidler, M. Motzkus, and F. Reichel, "A new high-resolution femtosecond pulse shaper," *Appl. Phys. B* **72**(5), pp. 627–630, 2001.

[18] C. Tsallis and D. A. Stariolo, "Generalized simulated annealing," *Physica A* **233**(1-2), pp. 395–406, 1996.

[19] S. Kirkpatrick, C. D. Gelatt, and M. P. Vecchi, "Optimization by simulated annealing," *Science* **220**(4598), pp. 671–680, 1983.

[20] H. Szu and R. Hartley, "Fast simulated annealing," *Physics Letters A* **122**(3-4), pp. 157–162, 1987.

[21] G. P. Agrawal, *Nonlinear Fiber Optics*, Academic Press, 3rd ed., 2001.

[22] E. Treacy, "Optical pulse compression with diffraction gratings," *IEEE J. Quantum Electron.* **5**(9), pp. 454–458, 1969.

Chapter 8

Conclusions

8.1 Summary

The work in this thesis has followed the build and development of an adaptive pulse shaping system for the MIR wavelength regime. The final experiment presented was on an adaptive fibre CPA system since this will become important in future work where a new femtosecond MIR source will be used for coherent control experiments.

The motivation of such coherent control experiments and the background leading up to adaptive optimal coherent control was given in Chapter 1. The theory of pulse shaping, SPOPOs and optimisation algorithms was reviewed in Chapter 2 before a discussion of pulse characterisation techniques in Chapter 3. The theory of time-frequency domain techniques such as the FROG and sonogram were presented after an initial review of the autocorrelator. In particular, experimental results for MIR pulse characterisation using the FRAC, CCS and XFROG were shown and a comparison of the latter two techniques was carried out. The results of the comparison showed that the XFROG technique is more sensitive and therefore the preferred choice of MIR pulse characterisation for spectral phase and amplitude retrieval. However, note that the experimental results of parametric transfer in Chapter 6 use the CCS for characterisation as the experimental comparison of these two pulse characterisation methods was carried out at a later time.

In Chapter 4, adaptive MIR pulse shaping experiments demonstrated that MIR pulses could be indirectly shaped via an SPOPO. A simulated annealing algorithm was used to optimise the TPA of the MIR idler pulse resulting in pulse compression and double-pulse generation. Having demonstrated control over the temporal shape of the pulse, inspection of the spectral shape of the idler showed serious degradation in comparison to the input pump pulse. In order to achieve maximum control over the idler pulse shape, one would ideally require that the pump pulse shape is transferred faithfully to the idler. This process, termed parametric transfer, was the subject of numerical investigation in Chapter 5. Starting from a simple DFG process and then extending the analysis to SPOPOs, the factors affecting parametric transfer were identified. It was found that in a SPOPO high fidelity parametric transfer can be achieved by narrowing the signal bandwidth using a spectral filter, such as an etalon, inside the cavity. The temporal walk-off between the pump and idler can cause significant degradation and can be minimised by careful choice of wavelength or using a short crystal length. On the other hand, the temporal walk-off between the pump and signal can be compensated for by cavity length tuning to adjust the timing of the pump-signal walk-through inside the crystal. Effects due to higher order dispersion such as GVD should be minimised, again, using a short crystal length. Pre-compensation of GVD with the pulse shaper should also be possible to allow a certain target pulse to be generated. Finally, good fidelity also generally coincided with high pump depletion and low signal amplification. These factors are readily obtained in an efficient system by operating 3-4 times above threshold and having HR resonator mirrors for the signal, while the idler is extracted. This numerical study was verified experimentally in Chapter 6. The pump and idler pulses were characterised using the CCS technique to assess the quality of transfer.

Having demonstrated adaptive shaping of MIR pulses and that high fidelity transfer can be achieved in an SPOPO, for the application of high resolution MIR pulse shaping, the techniques developed in this picosecond system can be transferred to a femtosecond fibre CPA system for progress towards coherent control experiments. Results of an initial experiment with such a CPA system were presented in Chapter 7. Two different CPA systems were investigated where one had a grating stretcher and the other had a fibre stretcher. The output pulse for the grating stretcher setup was found to be significantly

better quality since the pulse shaper had to compensate for fewer nonlinear effects. In the fibre stretcher system, the shaper was placed before the stretcher in a pre-compensation arrangement. However, it was found both experimentally and numerically, that full pre-compensation of large SPM broadening could be not be achieved and therefore resulted in poorer pulse quality. The results also highlighted the limitations of the pulse shaper, particularly at high pulse energies. It was found that, at these energies, oscillatory structure on the pulse spectrum increased as a result of SPM, challenging the resolution limits of the shaper. Despite these limitations, high quality pulses up to 65 μJ were obtained and it was demonstrated that adaptive pulse shaping improved the pulse quality in all situations.

The shaped output pulses of the high power fibre CPA system could certainly be used to pump a PPLN SPOPO for shaped MIR femtosecond pulse generation as a source for coherent control experiments. This will be the aim of future experiments, as discussed in the next section.

8.2 Outlook

In parallel to the work presented in this thesis, a fibre CPA system similar to the one used in Chapter 7 was built. However, thus far, the system generates comparatively low energy pulses due to the high repetition rate of 50 MHz. Due to the low pulse energy, the system does not have a stretcher but has a compressor. Recent work in achieving adaptive phase and amplitude shaping has been demonstrated with this system [1]. Optimisation for pulse compression was achieved with the use of a differential evolution algorithm that was described in Section 2.4 and has been shown to provide more reliable convergence in comparison to the previously used SA algorithms. Bandwidth limited pulses of 170 fs were been achieved for pulse energies of 252 nJ with the pulse shaper compensating for residual third order dispersion from the fibre oscillator.

Future work, using these shaped NIR pulses to pump a SPOPO to achieve shaped MIR femtosecond pulses, will be carried out. Since we will be using femtosecond pulses to pump the SPOPO, one would expect significantly higher peak powers leading to higher

order nonlinear effects, such as SPM, to occur within the PPLN crystal. At these pulse lengths, GVD is also more significant and overall the parametric transfer of high fidelity pulses to the MIR idler becomes more of a challenge. A simple way to reduce these unwanted effects is to use shorter crystal lengths and it is expected that 1mm long crystals will be used in future experiments. As the fibre CPA source is power scalable, it should also be possible to increase the spot sizes in the SPOPO such that the intensity is kept at manageable levels

The initial coherent control experiment intended for the adaptive MIR femtosecond pulse shaper is to investigate the molecular orientation of surface water molecules using vibrational sum frequency spectroscopy (VSFS) [2, 3]. The water surface plays a significant part in many biological processes, such as, membrane formation and protein folding, so understanding more about the vapour/water interface is of great interest. In this coherent control experiment, the MIR idler will be resonant with the OH stretching mode at $\sim 3\,\mu$m. Preliminary experiments to adaptively enhance the surface SFG from a thin gold film, will be carried out first.

Experiments with higher energy pulses are also anticipated for which a fibre stretcher will be used. Owing to the results from Chapter 7, the shaper will be placed after the fibre stretcher for post-compensation of SPM broadening.

In the longer term, it is hoped that more novel PPLN crystals, such as MgO-doped PPLN [4, 5] and chirped or aperiodic poling [6], may be used to enhance the tuning range of the adaptive MIR source. Extending these techniques to other nonlinear gain materials, with extended MIR tuning ranges, is also of interest.

References

[1] J. Prawiharjo, N. K. Daga, R. Geng, J. H. V. Price, D. C. Hanna, D. J. Richardson, and D. P. Shepherd, "High fidelity femtosecond pulses from an ultrafast fiber laser system via an adaptive amplitude and phase pre-shaping," *Opt. Express* , 2008.

[2] G. L. Richmond, "Molecular bonding and interactions at aqueous surfaces as probed by vibrational sum frequency spectroscopy," *Chem. Rev.* **102**, pp. 2693–2724, 2002.

[3] X. Zhuang, P. B. Miranda, D. Kim, and Y. R. Shen, "Mapping molecular orientation and conformation at interfaces by surface nonlinear optics," *Phys. Rev. B* **59**, pp. 12632–12640, 1999.

[4] H. Ishizuki, I. Shoji, and T. Taira, "High-energy quasi-phase-matched optical parametric oscillation in a 3-mm-thick periodically poled mgo:linbo3 device," *Opt. Lett.* **29**, pp. 2527–2529, 2004.

[5] M. Nakamura, M. Kotoh, H. Taniguchi, and K. Tadatomo, "Bulk periodically poled MgO-doped $LiNbO_3$ by external electric field application," *Japanese Journal of Applied Physics Part 2-Letters* **38**, pp. L512–L514, 1999.

[6] G. Imeshev, M. A. Arbore, M. M. Fejer, A. Galvanauskas, M. Fermann, and D. Harter, "Ultrashort-pulse second-harmonic generation with longitudinally nonuniform quasi-phase-matching gratings: pulse compression and shaping," *J. Opt. Soc. Am. B* **17**, pp. 304–318, 2000.

Appendix A

List of Publications

A.1 Journal Publications

1. F. He, H. S. S. Hung, J. H. V. Price, N. K. Daga, N. Naz, J. Prawiharjo, D. C. Hanna, D. P. Shepherd, D. J. Richardson, J. W. Dawson, C. W. Siders, and C. P. Barty, "High energy femtosecond fiber chirped pulse amplification system with adaptive phase control," Opt. Express 16, pp. 5813-5821, 2008.

2. H. S. S. Hung, J. Prawiharjo, N. K. Daga, D. C. Hanna, and D. P. Shepherd, "Experimental investigation of parametric transfer in synchronously pumped optical parametric oscillators," J. Opt. Soc. Am. B 24, pp. 2998-3006, 2007.

3. J. Prawiharjo, H. S. S. Hung, D. C. Hanna, and D. P. Shepherd, "Numerical investigations of parametric transfer in synchronously pumped optical parametric oscillators for indirect mid-infrared pulse shaping," J. Opt. Soc. Am. B 24, pp. 2484-2493, 2007.

4. J. Prawiharjo, H. S. S. Hung, D. C. Hanna, and D. P. Shepherd, "Theoretical and numerical investigations of parametric transfer via difference-frequency generation for indirect mid-infrared pulse shaping," J. Opt. Soc. Am. B 24, pp. 895-905, 2007.

5. N. A. Naz, H. S. S. Hung, M. V. O'Connor, D. C. Hanna, and D. P. Shepherd, "Adaptively shaped mid-infrared pulses from a synchronously pumped optical parametric oscillator," Opt. Express 13, pp. 8400-8405, 2005.

A.2 Conference Publications

1. N. K. Daga, F. He, H. S. S. Hung, J. Prawiharjo, D. C. Hanna, D. J. Richardson, and D. P. Shepherd, "Adaptive phase shaping in a fiber chirped pulse amplification system," Ultrafast Phenomena, Stresa, Italy, 2008, paper TUE5l.4.

2. F. He, H. S. S. Hung, N. K. Daga, N. A. Naz, J. Prawiharjo, J. H. V. Price, D. C. Hanna, D. P. Shepherd, D. J. Richardson, J. W. Dawson, C. W. Siders, and C. P. J. Barty, "High energy femtosecond fiber chirped pulse amplification system with adaptive phase control," CLEO, San Jose, 2008, paper CThB5.

3. D. P. Shepherd, N. K. Daga, R. Geng, D. C. Hanna, H. S. S. Hung, and J. Prawiharjo, "Adaptive Pulse Shaping of Ultrafast Mid-IR Optical Parametric Oscillators," (invited) LPHYS'08, Trondheim, Norway 2008.

4. H. S. S. Hung, J. Prawiharjo, N. K. Daga, D. C. Hanna and D. P. Shepherd, "Parametric transfer in a synchronously pumped optical parametric oscillator," LPHYS'07, Leon, Mexico 2007, paper 5.4.4.

5. H. S. S. Hung, J. Prawiharjo, N. K. Daga, D. C. Hanna and D. P. Shepherd, "Spectral phase and amplitude measurements of parametric transfer in a synchronously pumped optical parametric oscillator," CLEO, Baltimore, 2007, paper CTuM4.

6. J. Prawiharjo, H. S. S. Hung, N. K. Daga, A. Williams, D. C. Hanna, and D. P. Shepherd, "Parametric transfer in a synchronously pumped optical parametric oscillator: toward coherent control," (invited) Sixth International Symposium on Modern Optics and its Applications, Bandung, Indonesia, 2007, paper IP-14.

7. H. S. S. Hung, N. A. Naz, J. Prawiharjo, D. C. Hanna, and D. P. Shepherd, "Parametric transfer in a synchronously pumped optical parametric oscillator," LPHYS'06, Lausanne, 2006, paper 5.3.3.

8. H. S. S. Hung, N. A. Naz, J. Prawiharjo, D. C. Hanna, and D. P. Shepherd, "Parametric transfer in a synchronously pumped optical parametric oscillator," CLEO, Long Beach, 2006, paper CtuZ6.

9. N. A. Naz, H. S. S. Hung, M. V. O'Connor, D. P. Shepherd, and D. C. Hanna, "An intelligent, synchronously pumped optical parametric oscillator using adaptive pulse-shaping techniques," CLEO, Baltimore, 2005, paper CThQ6.

A.3 Contributions to Conference Proceedings

1. N. K. Daga, F. He, H. S. S. Hung, N. A. Naz, J. Prawiharjo, D. C. Hanna, D. J. Richardson, and D. P. Shepherd, "Adaptive phase shaping in a fiber chirped pulse amplification system," Ultrafast Phenomena XVI: Proceedings of the 16th International Conference, Stresa, Italy, 2008, to be published.